Proceedings of the 8th Meeting of Japan CF Research Society

Edited by Hiroshi YAMADA

November 29-30, 2007

Doshisha University, Japan

Preface

This is Proceedings of the 8th Meeting of Japan CF Research Society, JCF8, held at Doshisha University, 29-30 November 2007.

Japan CF-Research Society (JCF) was established in March 1999, with scientific presentations and annual general meeting JCF1 at Osaka University on 29-30 March, aiming at promotion of CF researches in Japan and sending the information to the world. The CF researches concern investigation of nuclear reactions that have been newly found and are considered to be taking place in the environment of condensed matter. The main goal is to develop science and technology to extract meaningful energy and extensive application of the CF phenomena. The CF researches are based on a variety of scientific fields and require collaboration efforts from nuclear physics, fusion science, radiation physics, quantum science and technology, accelerator and particle beam science, laser science, molecular dynamics, condensed-matter physics, surface physics, catalysis science, physical chemistry, metallurgy, electrochemistry, hydrogen science, thermodynamics, acoustics, and so on.

Following JCF1, we have successfully organized JCF meetings almost every year; JCF2 (Hokkaido University, 21-22 October 2000), JCF3 (Yokohama National University, 25-26 October 2001), JCF4 (Iwate University, 17-18 October 2002), JCF5 (Kobe University, 15-16 December 2003), JCF6 (Tokyo Institute of Technology, 27-28 April 2005), and JCF7 (Kagoshima University, 27-28 April 2006). For almost all meetings from and after JCF4, we have published electronic versions (via internet) of Proceedings in addition to their printed versions, which are written in English. This is because we strongly intend to be one of the key societies for international cooperation and information exchange.

The scientific area of CF researches in the world is now called Condensed Matter Nuclear Science (CMNS), since establishment of The International Society for Condensed Matter Nuclear Science (ISCMNS; http://www.iscmns.org/) in 2003. Accumulation of research efforts by researchers in the world since 1989 has revealed existence of nuclear reactions in condensed matter that are considered to occur by synergic effects of nuclear and condensed-matter physics under peculiar circumstances in the condensed matter. Concrete results obtained in latest reports are especially noteworthy. Clean deuteron-related fusion with ^{4}He ash and cold transmutation of host metal and/or added nuclei in metal-hydrogen isotope systems are regarded as actual consequences of latest CMNS studies, both in experiments and theories. JCF has been keeping close relation and collaboration with ISCMNS and researchers in the world.

Papers submitted to JCF8 have been peer-reviewed by JCF Editorial Board chaired by Professor Hiroshi Yamada, Iwate University. One or two referees were offered to review each paper submitted, who made extensive reviewing to give constructive comments, questions and recommended corrections, if any. After receiving the revised versions, the papers have been accepted for publication. This book/file, Proceedings of JCF8, does not necessarily contain all contributions presented at the JCF8 meeting. Some authors are permitted, if they whish, to make their contribution as "A note without reviewing" within 2 pages. Program and Abstracts of all the presentations are available on a JCF webpage http://dragon.elc.iwate-u.ac.jp/jcf/JCF8/.

We thank all participants of JCF8.
March 2008,

Akira Kitamura (Prof., Kobe University), Director-in-Chief, JCF
Hiroshi Yamada (Prof., Iwate University), Chairman, JCF Editorial Board

CONTENTS

A New Approach to Observe Optical Phonon in Hydrogen Storage Pd Using Raman Spectroscopy

Ken-ichi TSUCHIYA[a)], Shinnosuke ASANO[a)], Masao OZAKI[b)] and Shigeru SASABE[c)]

a) Tokyo National College of Technology, 1220-2 Kunugida, Hachioji. Tokyo 193-0997
b) Tokyo University of Agriculture, 1-1-1 Sakuragaoka, Setagaya, Tokyo, 156-8502
c) Tokyo Metropolitan University, 1-1 Minami-Ohsawa, Hachioji, Tokyo 192-0397

Abstract: Hydrogen storage Pd has Raman active optical phonons induced by hydrogen-hydrogen interaction. In this study, Raman spectra of PdH_x and PdD_x were measured for some hydrogen storage rates at room temperature. As a result, a broad peak was detected at 56meV for PdH_x and PdD_x. The isotope effect was not observed. These measurements can be done for the samples completely sealed in a glass tube cutting off the external air. If repetitive measurements are done, the change of phonon states in hydrogen storage Pd can be detected along the passage of time. This will lead to the detection of nuclear reaction in Pd as a large change of phonon states.

1 Introduction

When laser light is scattered from lattice vibration, most photons are elastically scattered. It is called Rayleigh scattering. However, a small fraction of scattered wave has different frequency from that of incident wave. In this case, the frequency shift $\Delta\nu$ is called Raman shift, which is created by the interaction between incident laser light and optical phonon. If the frequency of the scattered wave is increased, it is called anti-Stokes scattering. If it is decreased, it is called Stokes scattering. They are schematically sketched in Fig.1.

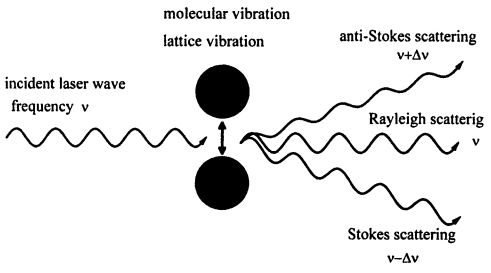

Fig.1 Scattering of laser light by lattice vibration. Stokes and anti-Stokes scatterings are called Raman scattering.

The energy diagram of these scattering is shown in Fig.2. The Stokes and anti-Stokes scattering are called Raman scattering. In Stokes scattering, energy of the incident laser light hν is temporally absorbed by phonon in the ground state and it is exited to a virtual state. Then scattered light with frequency ν-Δν is emitted and the phonon is fallen to the first exited state. The anti-stokes scattering is occurred by the excitation of phonon in the first exited state and scattered light with frequency ν+Δν is emitted. Therefore, the Raman shift Δν includes the information about the optical phonon.

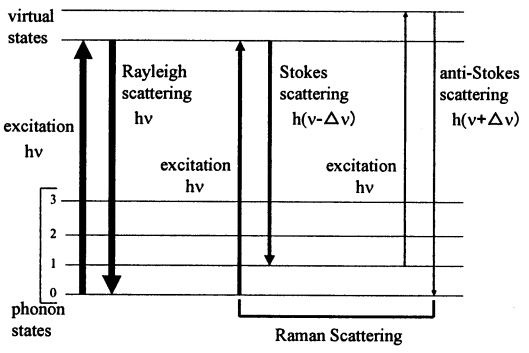

Fig.2 Energy diagram of Raman scattering. The thicknesses of the arrow roughly show the population.

This study shows a method to observe the states of optical phonon in hydrogen storage Pd using Raman spectroscopy. In solid state physics, it is well known that pure Pd lattices only have acoustic mode lattice

vibrations, because it forms perfect fcc structure. However, hydrogen–hydrogen interactions in Pd induce optical mode lattice vibrations [1]. This means that optical phonon in hydrogen storage Pd can be observed by using Raman spectroscopy. In this study, we have tried it for PdH_x and PdD_x.

This method can be applied to the detection of the nuclear reactions in Pd. This is done by the repetitive measurements of the Raman spectra of hydrogen storage Pd. In these measurements, the large changes in Raman spectra may inform us the effects from the condensed states of hydrogen and nuclear reactions in Pd. For example, the estimated result for the repetitive measurements is shown in Fig.3.

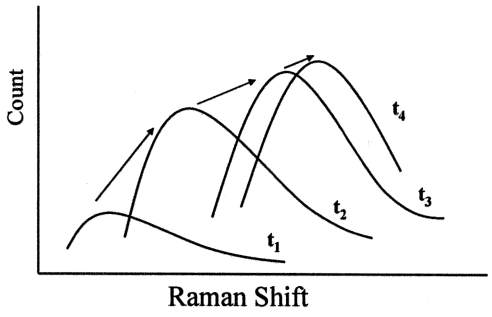

Fig.3 Estimated result for the repetitive measurements.

In Fig.3, the Raman spectra along the passage of time as t_1, t_2, t_3 and t_4 can be seen. These data may contain the information about the events in Pd.

2 Raman spectroscopy

The Raman spectroscopy system we used in this study is shown in Figs. 4 and 5. This measurement can be done for the sample completely sealed in a glass tube cutting off the influence of the external air, because glass materials are Raman inactive. The standard scanning time for this measurement is 15 minute. So we can easily observe the change of phonon states along the passage of time by repetitive measurements.

The wave length of the incident laser light for the excitations of phonons was fixed at 532.25nm. And the measurements were done at room temperature.

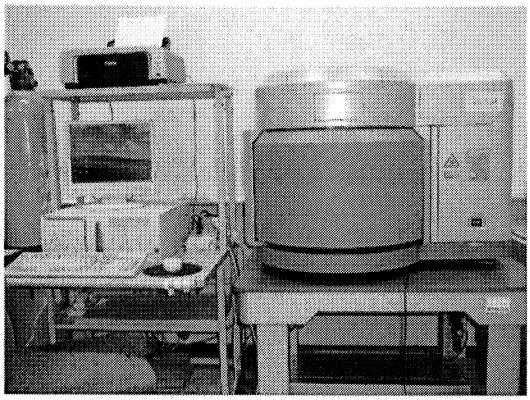

Fig.4 Raman spectroscopy system (NRS-3100 made by JASCO).

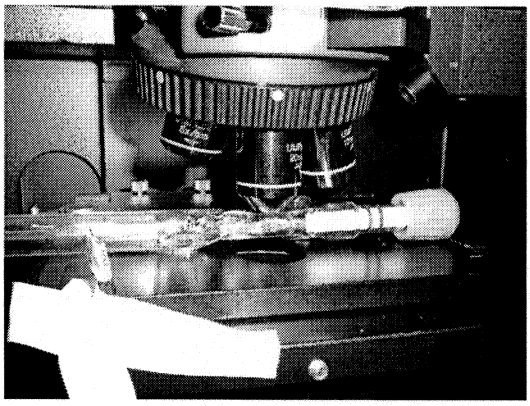

Fig.5 Detection chamber of the system. Hydrogen storage Pd sealed in a grass tube is put on the stage. The conditions for the measurements are following.
Exposure time : 50.00 sec
Integration times : 5 times
Objective lens : UMPLFL 20×
Excitation wavelength : 532.25 nm

3 Hydrogen storage

In this study, the hydrogen storage rate was determined by the constant volume method. The sketch of the storage device composed by grass tube is shown in Fig. 6. This device consists of two parts. One is the space with a constant volume V_0, which is used for the calculation of the storage rate. The other is the hydrogen storage unit. After the storage, the hydrogen storage unit including the Pd sample is taken off and put on the stage in the detection chamber, which is shown in Fig.5.

The gases we used here were 99.9% H_2 and 99.6 % D_2. The Pd was 99.9% purity, and size of 15mm ×5mm×0.1mm.

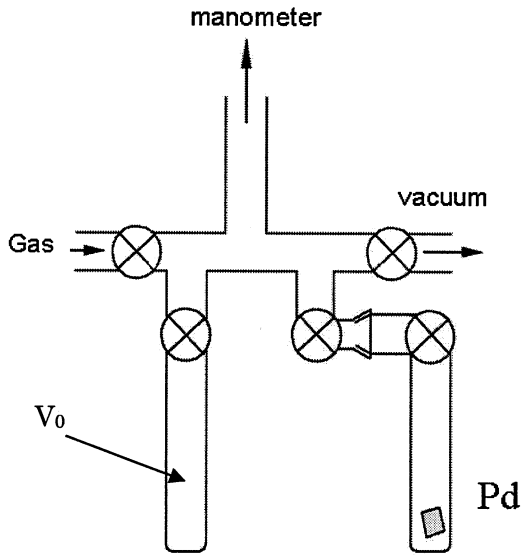

Fig.6 Hydrogen storage device.

4 Results and discussions

The Raman spectra for some storage rates at room temperature are plotted in Figs.7 and 8. In both of them, the data for the pure Pd and the back ground are also plotted for comparison. Seeing the results for PdH_x in Fig.7, broad peaks induced by the interactions between protons in Pd exist at 56 meV for every concentration. They are consistent with the results of Sherman et al. which has a peak at 58.5meV [2]. Sharp peaks at 80meV and 210meV are due to PdO and Ne, respectively. The surfaces of the Pd plates we used were slightly oxidized and PdO peak was detected. Ne peak was detected, because Ne ramp was used for the reference signal. Other sharp peaks are unknown noises. For the case of PdD_x in Fig 8, a broad peak at 56meV due to D-D interactions was detected. This is inconsistent with Sherman's result which has a peak at 39.7meV [2]. PdO and Ne peaks were also detected here.

We consider that the isotope effect at 84K and 18K reported by Sherman et al. [2] has disappeared in our experiments at room temperature. Now, we have no appropriate theoretical explanations for the mechanism of them. However, the condensed states of deuterons in Pd [3] may affect the phonon states and then change Raman spectra. The paper of Kalman [4], which reported that phonon exchange of each branch between quasi-free particles (deuterons) moving in a crystal lattice partly filled with deuterons can lead to an interaction potential that becomes attractive for small distances with increasing deuteron-density fraction, also suggests the possibility of the drastic change of phonon states in PdD_x. Additionally, we consider that the theory for spin-magnetic moment by Sasabe and Tsuchiya [5], which suggests the possibility of the reduction of Coulomb interaction in solid, should help to solve this problem.

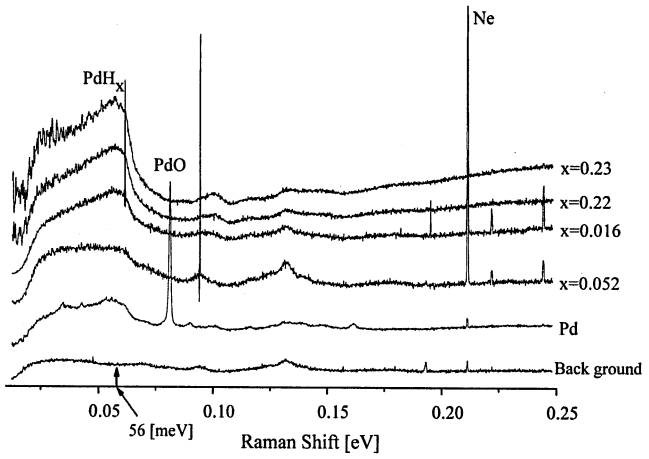

Fig.7 Raman spectra of PdHx.

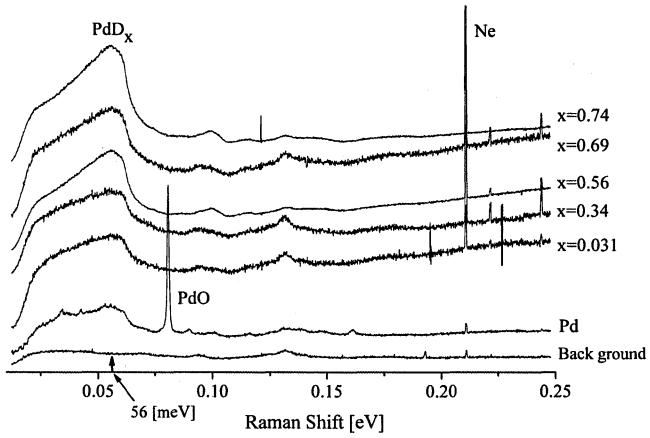

Fig.8 Raman spectra of PdDx.

5 Conclusions

(i) The elementary data for the Raman spectrum of PdH_x and PdD_x for some storage rates at room temperature were obtained. They include the information about the quantum states of protons and deuterons in Pd. As a result, a broad peak was detected at 56meV for PdH_x and PdD_x. The isotope effect reported by Sharman [2] was not observed here.

(ii) In this paper, we have shown the method how to detect the nuclear reactions in Pd by measuring the change of phonon states. In near future, we will try to have repetitive measurements and investigate the change of phonon states along the passage of time. If nuclear reactions are occurred in Pd, the phonon states may change largely. They are able to be detected as the large change of Raman spectrum.

Acknowledgements

The authors wish to thank Professor Akito Takahashi of Osaka University and Professor Hiroshi Yamada of Iwate University for helpful discussions and encouragements. We also wish to thank Professor Noboru Akuzawa of TNCT for the advices on the hydrogen storage techniques.

References

1. J.M.Rowe, J.J.Rush, H.G.Smith, M.Mostoller and H.E.Flotow, "Lattice Dynamics of a Single Crystal of $PdD_{0.63}$", Phys. Rev. Letts., **33**,1297(1974)
2. R.Sherman, H.K.Birnbaum, J.A.Holy and M.V.Klein, "Raman studies of hydrogen vibrational modes in palladium", Phys. Lett., **62A**,353(1977)
3. K.Tsuchiya, "Quantum States of Deuterons in Pd.", International Journal of Hydrogen Energy, **29**,1513 (2004)
4. P.Kalman and T.Keszthelyii, "Attractive d-d interaction via phonon exchange in deuterated Pd", Nuclear Instruments and Methods in Physics Research, **B240**,781(2005)
5. S.Sasabe and K.Tsuchiya, "What is spin-magnetic moment of electron?", Phys. Letts. **A372**, 381(2008)

Investigation of Nuclear Phenomena in Deuterium Diffusion from Pd Heterostructure

S.Narita*, H.Yamada, M.Sakuraba, Y.Fukuda

Department of Electrical and Electronic Engineering, Iwate University

Morioka, Iwate, 020-8551, JAPAN

* narita@iwate-u.ac.jp

ABSTRACT

According to the recent experimental results by several researchers, it has been supposed that the fine-processed sample, such as nano-size Pd or multi-layered Pd complexes is connected closely with the trigger condition for LENR (low energy nuclear reaction in condensed matter). In this study, we investigated the deuterium absorbing and desorbing behavior followed by LENR in heterostructure sample of Pd and different kind of materials. As a result, it was found that the deuterium absorption capability was different in the sample materials. In addition, anomalous heat evolution with explosive gas desorption, which might be concerned with nuclear reaction, was observed in a specified experimental condition.

Keywords: heterostructure, nano-size Pd, deuterium absorption and desorption, CR-39

1. Introduction

It has been known that nano-size Pd cluster is capable of absorbing hydrogen effectively, rather than the bulk Pd [1,2]. Such property of fine Pd cluster is possibly connected with the trigger condition of low energy nuclear reaction (LENR) in condensed matter. For instance, Arata proved helium production in deuterium absorption process to nano-particle Pd [3]. On the other hand, Iwamura has reported that the selective transmutation occurs in permeation of D through thin-layered Pd/CaO complexes [4]. Yamaguchi observed the excess heat and helium production in controlled deuterium diffusion from the heterostructure Au/Pd/MnO sample [5]. Lipson also reported charged particle emissions in deuterium diffusion from Pd/PdO sample [6]. In these experiments, the fine structure of the sample, *i.e.* nano-size Pd or multi-layered Pd complexes, is thought to play an important role for inducing LENR.

Considering these experimental results, we performed the deuterium absorption and desorption experiment using heterostructure samples such as Pd/Au, Pd/CaO and Au/Pd/CaO. In this paper, we report characteristics of the deuterium absorption and diffusion processes followed by nuclear phenomena for each sample type.

2. Experiment

In the present experiments, we tested the following heterostructure samples; Pd/Au, Pd/CaO, Au/Pd/CaO. The Pd foil (4 mm x 25 mm x 0.1 mm in size, 99.95 % in purity) was washed with acetone and aqua regia. Then, Au and/or CaO layers were deposited onto the Pd foil by Ar ion beam sputtering. The thickness of Au and CaO layers were approximately 600-800 nm and 20-40 nm, respectively. After that, the sample was loaded with deuterium under 10 atm pressure for 10 h. The weight of the sample was measured before and after loading and the loading ratio (D/Pd) was obtained from the difference. After loading, the sample was set into the chamber which has a cylindrical shape with volume of 880 cm^3 equipped with a turbo-molecular pump to be evacuated. The pressure in the chamber was measured by an ionization vacuum gauge. A DC power supplier supplied constant current to the sample through chrome steel clips in the chamber. These clips were also utilized for fixing the sample. The sample temperature was measured by a thermocouple with an accuracy of ±1℃. The experimental apparatus is shown in Fig.1.

After evacuating the chamber to a pressure below ~10^{-5} Pa, the temperature and the pressure in the chamber measurements were started. Then, the sample was supplied with an electric current of ~4 A. The experiment continued for about 24 h. The sample was taken out from the chamber after the current was

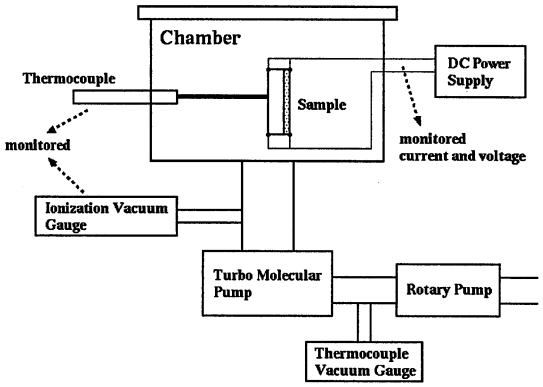

Fig.1. Experimental apparatus.

stopped and weighted to estimate how many D atoms remained in.

The CR-39 track detector (Fukuvi Chemical Industry) was used for charged particle detection as the evidence of nuclear reaction. The detector is made of diethyleneglycol bis allylcarbonate with thickness of 1mm. When a charged track crosses the detector the material was damaged along trajectory. As the velocity of etching in chemical reagent for the damaged zone is larger than other area, the track pit appears after etching. We used optimal etching conditions 5 N NaOH solutions at 70℃ for 7 h. During the experiment, 4 pieces of CR-39 were placed surrounding the sample. Each detector faced front surface, back surface, and two short side edges of the sample, respectively.

In prior to the experiment, the background behavior was examined for the distribution of the number of tracks on the detector (Fig.2). The averaged number of tracks for 44 background runs was 11.1. If there is a large excess in the number of tracks in a foreground run, it can be considered as the emission of charged particles. The diameter distribution for the background tracks is shown in Fig.3. The energy calibration for alpha tracks was also performed using ^{241}Am. The track diameter as a function of the energy of alpha particles is shown in Fig.4. The scattered plots in the energy range 1-3 MeV are our calibration results. The energy was adjusted by changing the distance between the alpha source and the detector. The solid line in Fig.4 was cited from the results obtained by Roussetski et al [7]. Since their etching condition was the same as ours, both data can be connected. For alpha particle with the energy below ~3 MeV, the track diameter does not correspond to the energy clearly, while, the energy can be roughly estimated from the track diameter below 10 μm (energy above ~4 MeV).

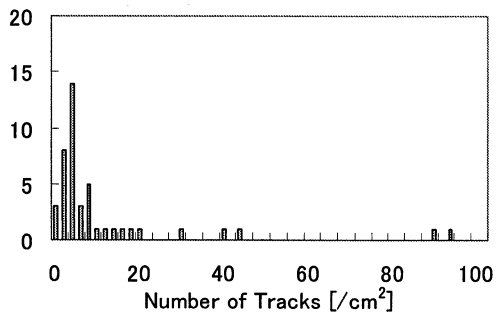

Fig.2. The number of tracks for background runs.

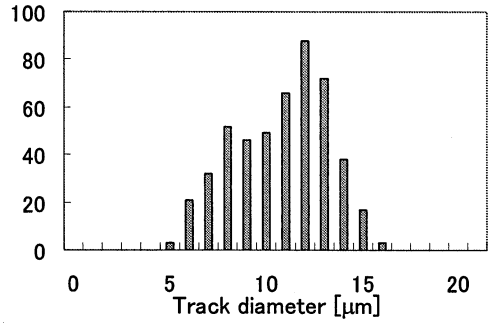

Fig.3. Track diameter for background runs.

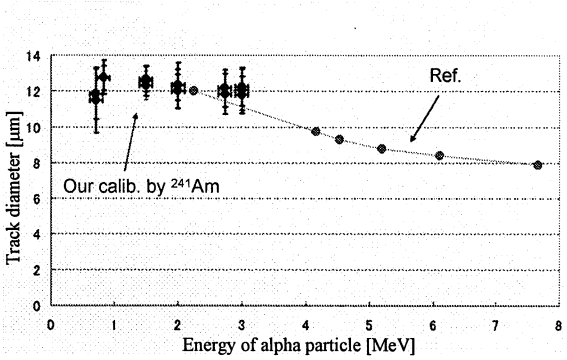

Fig.4. Calibration data between track diameter and the energy of alpha particle.

3. Results and Discussion

The D/Pd for each sample type is shown in Fig.5. Note that the D/Pd shown here is obtained averaged over the sample entirely. The heterostructure seems to help achieve higher D/Pd comparing with plain Pd foil. Especially, the sample coated with both surface, *i.e.* Au/Pd/CaO, shows high D/Pd. We also investigated the D/Pd of the sample Pd(40nm) / CaO(2nm) / Pd(0.1mm), which is similar sample to that used in deuterium permeation experiment by

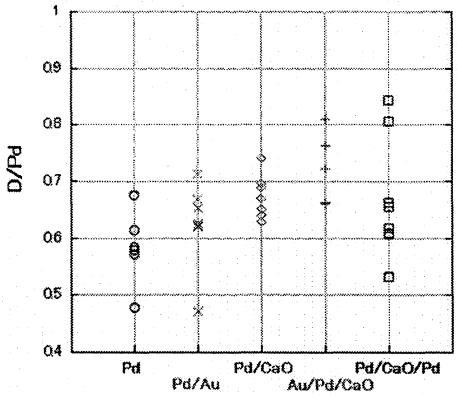

Fig.5. D/Pd for each sample type.

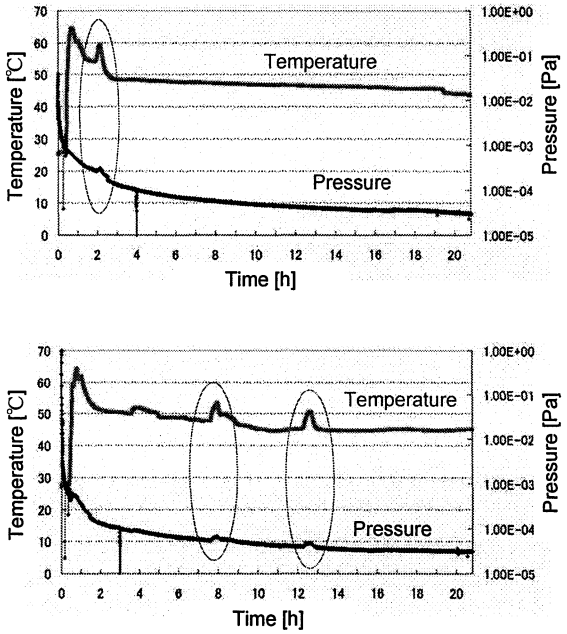

Fig.6. Time dependence of the temperature and the pressure for Au/Pd sample (Top) and Au/Pd/CaO sample (bottom).

some researchers. [4,8,9,10]. The D/Pd for the sample was sometimes quite high, but not always. These results suggest that the D/Pd depends on the sample structure and the materials.

Figure 6 shows the time evolution of sample temperature and the pressure in the chamber for Au/Pd and Au/Pd/CaO samples. The temperature increased just after applying DC current, then, it reached to the thermal equilibrium state balancing exothermic and endothermic process. After a certain

Au/Pd	# of tracks [/cm^2]	Au/Pd/CaO	# of tracks [/cm^2]
Au-side	8	Au-side	5
Pd-side	133	CaO-side	290
Edge-1	113	Edge-1	6
Edge-2	4	Edge-2	2

Table 1. The number of tracks on CR-39 detector for the runs in which anomalous heat evolutions were observed.

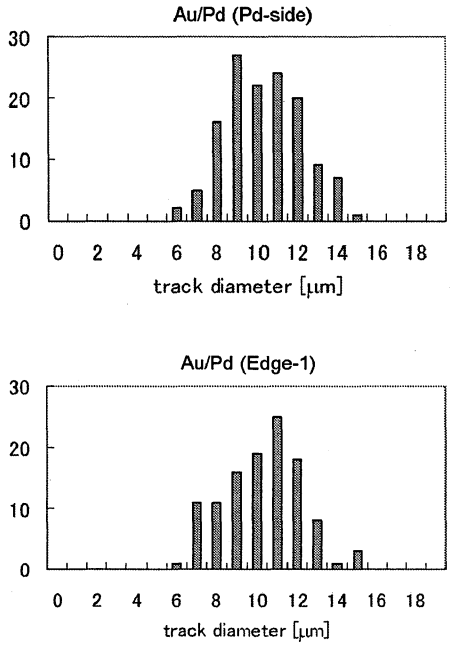

Fig.7(a). Diameter distribution of the tracks on CR-39 for the run with Au/Pd sample. The mean diameters of each distribution were 9.8±1.9 μm (top), 9.8±1.8 μm (bottom), respectively.

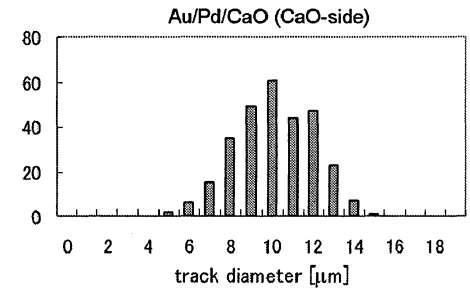

Fig.7(b). Diameter distribution of the tracks on CR-39 for the run with Au/Pd/CaO sample. The mean diameter was 9.6±1.9 μm .

Sample	#	Current supplied [A]	D/Pd		Initial Temperature [℃]	Anomalous T and P increase	Excess in CR-39
			before	after			
Pd/Au	1	4	0.62	0	~65	Yes	Yes
	2		0.62	0	~60	No	No
	3		0.47	0.33	~45	No	No
	4	6	0.62	0	~80	No	No
Pd/CaO	1	4	0.63	0.02	~55	No	No
	2		0.68	0.15	~45	No	No
	3	6	0.65	0.04	~75	No	No
Au/Pd/CaO	1	4	0.66	0	~65	Yes	Yes
	2		0.66	0.12	~50	No	No

Table 2. Summary table of anomalous temperature behavior and excess in the number of tracks on CR-39.

time, the heat evolution simultaneously with explosive deuterium desorption from the samples was sometimes observed. (see elliptical areas marked in Fig.6) The phenomena occurred in 1 out of 4 runs with Au/Pd sample and 1 out of 2 runs with Au/Pd/CaO runs. In principle, the temperature should drop in desorption process because it is endothermic reaction. Also, it was difficult to explain the phenomenon by Joule heat because the voltage and the current monitored did not indicate considerable change before and after the event. This anomalous phenomenon does not seem to be originated by chemical reactions.

We surveyed tracks on CR-39 used in these runs and found significant excess in the number of tracks on the detector for both runs (Table 1). Now it is supposed that the anomalous heat evolution observed is concerned with nuclear reactions. The track diameter distributions for those runs are shown in Fig.7(a) and 7(b). In both cases, the averaged track diameter was about 9.6-9.8 μm. Assuming that these tracks are originated by alpha particles, the energy was estimated to be ~4 MeV from the calibration results.

The dynamics of deuterium in desorption process should depend on various parameters, such as deuterium density in the host metal, sample structure and materials, surface conditions, pressure of environment, temperature, and so on. Among them, we paid attention at initial temperature of the sample just after flowing of the electric current. As described above, the sample was fixed by chrome steel clips through which the electric current supplied. In the current setup, the contact resistance between the end of clip and the sample was different run by run. Therefore, the Joule heat generated there was not always same even with the constant DC current supplied. The temperature varied from 45 to 60℃. In some runs, we tried to increase the current 4 A to 6 A, then the initial temperature was 75-80 ℃. The Temperature behavior and excess in the number of tracks on CR-39 for each runs are summarized in Table 2. For the runs with anomalous heat evolution and tracks, the initial temperature was about 65℃. In other runs which had initial temperature below 60℃ or above 70 ℃, anomalous phenomena, that is, temperature increase with explosive deuterium desorption did not observed clearly. This result makes us expect to existence of optimal temperature for triggering the anomalous phenomena in deuterium desorption and it may be 60-70℃. Now we plan to modify the experimental setup to control the initial temperature.

We tested three types of heterostructure sample in this study. As for the anomalies in heat evolution and the tracks on CR-39, we did not find clear difference in the sample materials and structure, and further numerous trials are still needed. In the past study, we performed similar experiment using plain Pd foil and we did not see anomalous heat evolution simultaneously with gas release at all. So the heterostructure itself is supported to be necessary for the phenomenon to occur.

Besides using heterostructure sample, we just

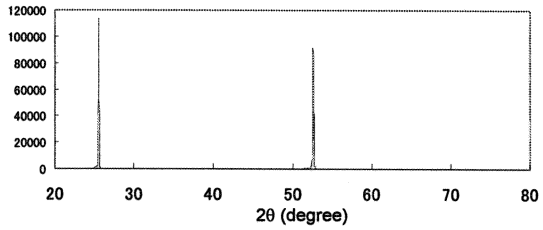

Fig.8. XRD results of the thin Pd layer formed on the sapphire by sputtering.

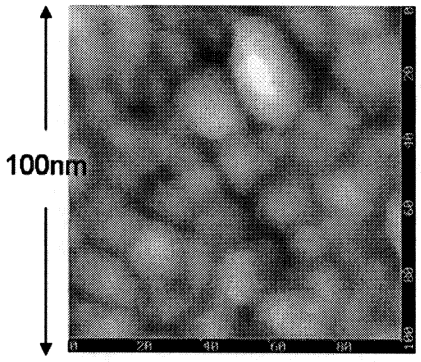

Fig.9. AFM image of thin Pd layer.

considered the characteristics of thin Pd film. As mentioned in introduction, nano-size Pd is another candidate to induce LENR effectively in deuterium absorption and/or desorption. Then, we investigated the structure of thin Pd layer (~20 nm) deposited on sapphire substrate. Figure 8 shows XRD results. Two peaks in the figure correspond to sapphire substrate, and there is no peak corresponding to Pd crystalline. This suggests that the Pd atoms exist with non-crystalline state (just like amorphous). The AFM image for the surface of the thin Pd layer is shown in Fig.9. The grain can be seen in the image. In the sample, Pd atoms do not form a certain arrangement but form a kind of cluster. This arrangement of the Pd may have an advantage for inducing LENR rather than bulk Pd with mono- or poly-crystalline state. For example, higher deuterium density can be realized locally in the sample. We will examine the deuterium dynamics in such sample in the next step. Furthermore, the deuterium dynamics in such Pd state should be investigated by numerical calculation such as first-principle molecular dynamics. It is another topic for the future study.

4. Summary

We performed deuterium absorption and desorption experiment with heterostructure sample, Au/Pd, CaO/Pd, Au/Pd/CaO. The deuterium absorption capability was different in the sample type. We could achieve higher D/Pd ratio with Au/Pd/CaO than the other reports. In desorption process, anomalous heat evolution was observed simultaneously with explosive deuterium out-diffusion for some runs. There was not clear dependence on the sample type but initial temperature of the sample. In such runs, anomalous tracks on CR-39 detector were also observed. These might be the evidence of nuclear reaction. The fine-processed sample surely has advantage to induce the LENR. Further studies will clarify the deuterium dynamics in such sample as well as the process inducing LENR.

References

1. A. Zuttel *et al.*, J. Alloys and Compd. 293-295 (1999) 472.
2. S. Yamaura *et al.*, J. Meter. Res. 17 (2002) 1329.
3. Y. Arata *et al.*, Proc. of ICCF10 (2006) 139.
4. Y. Iwamura *et al.*, Jpn. J. Appl. Phys. 41 (2002) 4642.
5. E. Yamaguchi *et al.*, Jpn. J. Appl. Phys. 29 (1990) L666.
6. A.G. Lipson *et al.*, Proc of ICCF12 (2006) 293.
7. A.Roussetski *et al.*, Proc. of ICCF11 (2006) 274.
8. H. Iwai *et al.*, Proc. of JCF7 (2006) 23.
9. H. Yamada *et al.*, Proc of ICCF12 (2006) 196.
10. S. Narita *et al.*, Proc of JCF7 (2006) 33.

Gas and heat balance during plasma electrolysis

T. Jang, A. Ishihara, S. Mitsushima and K. Ota
Chemical Energy Laboratory, Yokohama National University

Abstract : During water electrolysis in alkaline carbonate solutions, we observed plasma where the voltage-current curve has a critical voltage to start plasma. During the plasma electrolysis, we observed different behaviors compared with the conventional water electrolysis. In this region, the amount of hydrogen and oxygen exceeded theoretical amount which was calculated by the Faraday`s law. However, we could not detect the large excess heat production.

Keyword : water electrolysis; plasma electrolysis; hydrogen generation; excess heat

1. Introduction

Water electrolysis is well known as a process which produces hydrogen and oxygen when potential voltage over then 1.23V at the room temperature. In this process, oxidation and reduction occur at an anode and a cathode, respectively. An excess voltage is charged to proceed this reaction, and the temperature rises. Normally these reaction follows Faraday`s law for the amount of gas production, and the energy balance should follow the energy conservation law.

But in past researches, the amount of the gas generated in the plasma electrolysis exceeded the one expected by Faraday`s law.[1] Moreover, there was a possibility of an excess heat production in the electrolysis.[2]

These results suggest the possibility of developing a new method of hydrogen generation and a new energy resource. However, the reproducibility was not sufficient, and an explanation of the phenomena was required. In this study, we have studied behavior of current by voltage changes at different concentration of electrolyte and measured the accurate excess heat and gas production during the plasma electrolysis.

2. Experimental

Figure 1 is a schematic draw of the electrolytic flow cell. The cell was composed of an acrylic tubing, which had an internal diameter of 2cm, an external diameter of 5cm, and was about 30cm in length. The anode was a 2cm diameter hollow cylindrical platinum which has 99.99% purity 55mesh. The cathode was a 1.5mm diameter tungsten rod which has 99.95% purity. It was placed at the center of the cylindrical anode. The distance between the electrodes was 1cm.

The electrolyte was K_2CO_3 light water solution of 0.2~0.5M.

Figure 2 is a schematic draw of the flow cell system. The electrolyte circulated in this system, passing through a reservoir and
electrolyte flowmeter. The temperature difference between the inlet and outlet of electrolyte was measured with Pt resistance thermometers.

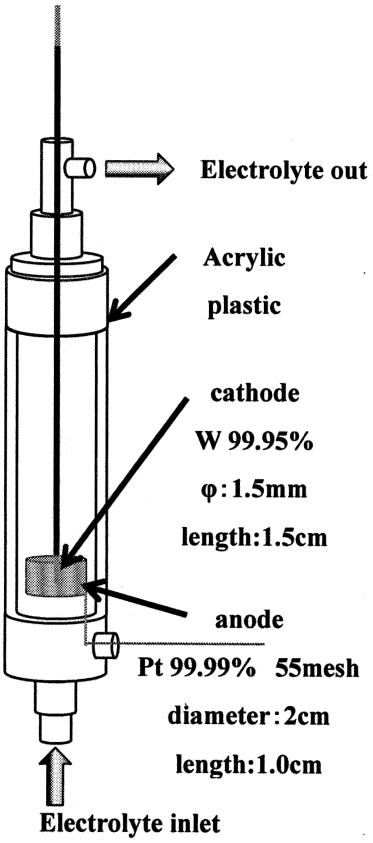

Fig 1. Schematic draw of electrolyte flow cell

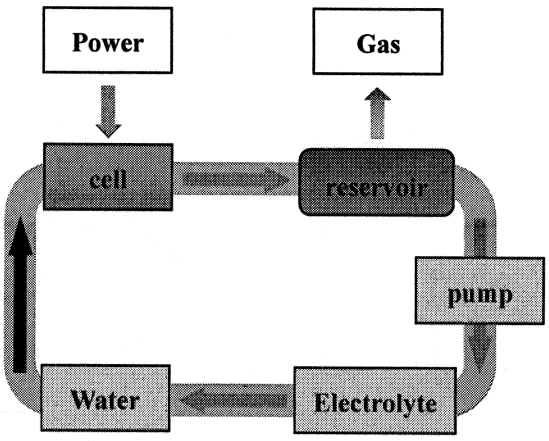

Fig 2. Schematic draw of flow system

Hydrogen and oxygen generated during electrolysis were collected in the reservoir, and the rate of gas generation was measured.

During electrolysis, the cell voltage and the current, the inlet and outlet temperatures of the electrolyte, room temperature, reservoir temperature, and the electrolyte flow rate were measured.

The input energy was calculated by the voltage and the current supplied. The output of energy was the sum of the temperature increase of the electrolyte, and latent energy. The temperature increase of electrolyte was determined by the temperature difference between the output and inlet of the electrolyte at the cell. The latent energy was determined from the flow rate of the gaseous product. The energy balance was calculated by the following equations.

$$E_{in} = U \cdot I \quad (1)$$

$$H_S = f_E \cdot \Delta T \cdot d \cdot Cp \quad (2)$$

$$H_L = f_g \cdot \Delta H \quad (3)$$

$$E_{out} = H_S + H_L \quad (4)$$

$$EB = E_{out} / E_{in} \quad (5)$$

E_{in} is input energy, U is the cell voltage, I is the cell current, H_S is the temperature increase of the electrolyte, f_E is the electrolyte flow rate, ΔT is the increase between the inlet and outlet of the electrolyte temperature, d is the density of the electrolyte, C_P is the heat capacity of the electrolyte, H_L is the latent energy of the H_2 and O_2 evolution, f_g is the generated gas flow rate, ΔH is the enthalpy change of the water electrolysis, E_{out} is the output energy and EB is the energy balance.

Table 1 shows the experimental conditions during electrolysis. In each experiment, inlet temperature of the electrolyte were kept at 26℃,and the flow rate of the electrolyte were fixed at the range of 600～800ml/min.

Table 1. Experimental condition during energy balance measurements

Concentration of solution	Density ($g \cdot cm^{-3}$)	Cp ($J \cdot K^{-1}g^{-1}$)
0.2M	1.02	4.04
0.3M	1.03	3.98
0.4M	1.04	3.92
0.5M	1.06	3.86

The gas balance is calculated as follows;

$$n_{ex} = (P_{air} - P_{vapor}) \cdot v_e / (R \cdot T) \quad (6)$$

$$n_{th} = N_a \times I / F \quad (7)$$

$$\eta = n_{ex} / n_{th} \quad (8)$$

n_{ex} is gas generation per second, P_{air} is atmospheric pressure, P_{vapor} is vapor pressure, v_e is generated gas flow rate, R is gas constant, T is temperature of produced gas during electrolysis, n_{th} is theoretically generated gas flow rate, N_a is gas generation amount per electron, F is Faraday constant, and η is gas balance. Because the theoretical generated gas flow rate was determined from Faraday's law of water electrolysis, the ratio of hydrogen to oxygen was 2:1.

3. Result and discussion

Figure 3 shows the cell voltage and the current as a function of time. The cell voltage was controlled during the electrolysis. In this figure, the current shows various behavior. At the beginning, the current increased with the voltage(I). After that, the current kept constant value(II), and then current decreased with increase of voltage(III). And finally, plasma occurs, and the current became low value(IV). These four regions had certain ranges of voltage, and these values varied with the concentration of electrolyte. Table 2 shows ranges of voltage of each region.

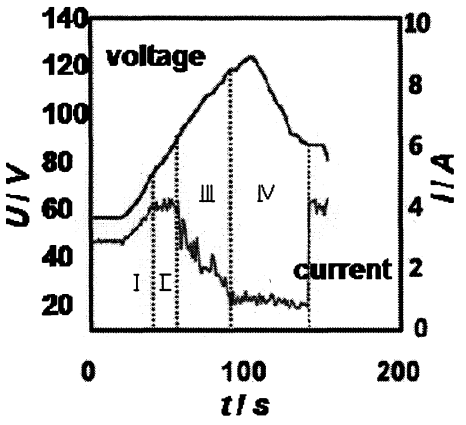

Fig 3. Behavior of current

Table 2. Range of voltage of stage

C of electrolyte	Voltage range			
	Stage I	Stage II	Stage III	Stage IV
0.2 Mol · L^{-1}	～ 72.4V	72.4V ～ 89.6V	89.6V ～ 126.7V	126.7V ～ 84.8V
0.3 Mol · L^{-1}	～ 61.6V	61.6V ～ 77.7V	77.7V ～ 121.8V	121.8V ～ 76.7V
0.4 Mol · L^{-1}	～ 52.9V	52.9V ～ 69.9V	69.9V ～ 114.2V	114.2V ～ 71.1V
0.5 Mol · L^{-1}	～ 44.2V	44.2V ～ 62.0V	62.0V ～ 98.6V	98.6V ～ 68.7V

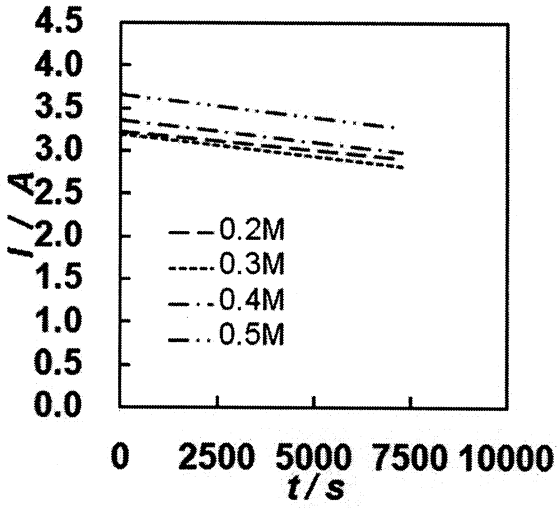

Fig 4. Behavior of current at different concentration of electrolyte

Figure 4 shows the current as a function of time during plasma electrolysis. Every experiment proceeded for 2hours at 90V, after the plasma formed. As a result, the current decreased with the time.

Figure 5 shows the amount of gaseous production as a function of time during plasma electrolysis. It shows gas flow decreased slowly with the time. This result might correspond to the current

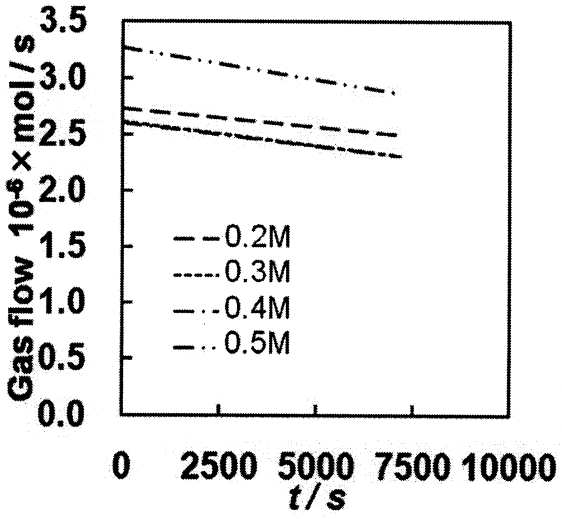

Fig 5. Behavior of gas flow

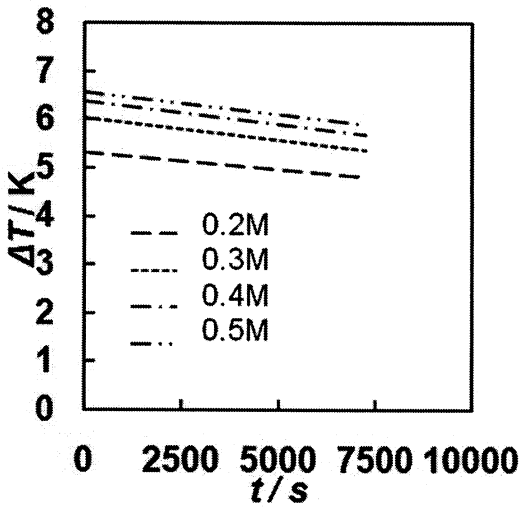

fig 6. Behavior of ΔT

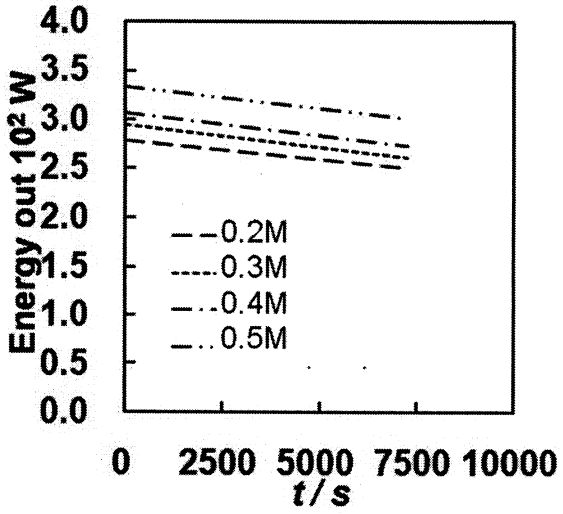

Fig 7. Behavior of energy out

Figure 6 shows the temperature difference between inlet and outlet of the cell.

Figure 7 shows the energy output from the cell during electrolysis. In these figure (Fig5, Fig6, Fig7), every factor decreased with time. These tendencies are mainly caused by the current change.

Figure 8 shows the gas balance during with and without plasma at 90V. In every concentration of electrolyte, more than 100% of gas balance was observed for plasma electrolysis. There was a

clear difference on gas balance between with and without plasma electrolysis, and at least more than 20% gas was produced at plasma electrolysis with respect to the non-plasma electrolysis.

Figure 9 shows energy balance during with and without plasma at 90V. At this figure we detected large energy output for plasma electrolysis. However, the difference is so small that we could not confirm the excess heat.

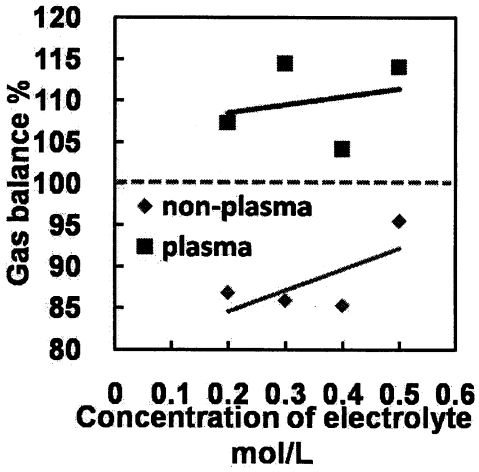

Fig 8. Gas balance during plasma vs. non-plasma electrolysis

4. Conclusions

In light water electrolysis using K_2CO_3, we observed plasma. During the plasma electrolysis, the excess formation of H_2 and O_2 was observed. However, we could not see large excess heat. Further study is necessary to confirm this phenomenon.

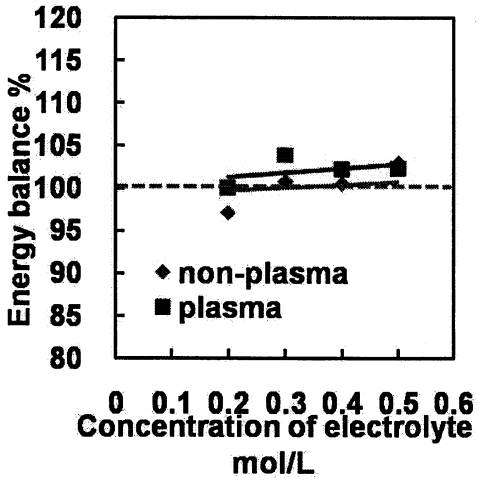

Fig 9. Energy balance during plasma vs. non-plasma electrolysis

References

1. T. Mizuno, T. Ohmori, T. Akimoto, and A. Takahashi,*Jpn. J. Appl. Phys.* 39, 6055(2000)

2. T. Mizuno, T. Akimoto, K. Azumi, and T. Ohmori, *Jpn. J. Appl. Phys.* 44, 396 (2005)

Investigation of Nuclear Transmutation in $(CaO/Sr/Pd)_n/CaO/Sr/Pd$ Samples

T. Yamaguchi*, T. Nohmi, H. Iwai, A. Taniike, Y. Furuyama and A. Kitamura**

(Division of Marine Engineering, Graduate School of Maritime Sciences, Kobe University)

5-1-1 Fukaeminami-machi, Higashinada-ku, Kobe 6580022, Japan

Email address: *076w529w@stu.kobe-u.ac.jp; **kitamura@maritime.kobe-u.ac.jp

N. Yabuuchi and A.Takahashi

(High Scentific Research Laboratory)

2nd Floor, Takano Building, 24-16 Marunouchi, Tsu City, Mie 5140033, Japan

Abstract: We have constructed an experimental system, with which accelerator analyses including PIXE, ERDA, NRA and RBS can be made *in situ* and simultaneously with deuterium gas permeation through the samples at elevated temperature, and performed experiments using multilayered $(CaO/Sr/Pd)_n/CaO/Sr/Pd$ samples. Although consistent changes have been observed in some runs, they are within the range of experimental error. It is necessary to increase the permeation D flux as well as the areal densities of D and the transmutation nuclei in the sample for further study.

Keywords: Nuclear transmutation, $(CaO/Sr/Pd)_n/CaO/Sr/Pd$ samples, D permeation, PIXE, NRA, ERDA

1. Introduction

It has been claimed that forced permeation of deuterium (D) through X-deposited (Pd/CaO)/Pd samples induced nuclear transmutation from the element X to Y, where (X, Y) being (^{133}Cs, ^{141}Pr), (^{88}Sr, ^{96}Mo), (^{138}Ba, ^{150}Sm) and (^{137}Ba, ^{149}Sm) **[1]**. To confirm the nuclear transmutation and to elucidate the mechanism, we have constructed an experimental system, with which accelerator analyses including PIXE, ERDA, NRA and RBS can be made *in situ* and simultaneously with gas permeation through the samples, with a sample temperature control system added in the present study.

The structure of our Pd multilayer film sample is different from those used in ref. 1. The basic structure of the samples is $(CaO/Sr/Pd)_n/CaO/Sr/Pd$ with an exception of Run 4 with no CaO layer, where $n = 9$ or 0. In the samples used in ref. 1, the nuclei to be transmuted are located on the sample surface, and exposed to D_2 atmosphere. In the present work, however, they are embedded in the sample between the CaO layer and the Pd layer/bulk, and exposed to D permeating through the sample. The feature of the sample is then expressed as $vacuum/(CaO/Sr/Pd)_n/CaO/Sr/Pd/D_2$.

2. Experimental apparatus and procedure.

A schematic of experimental setup is shown in Fig.1. The film was mounted on a vacuum flange with O-ring seal and the rear surface was exposed to D_2 gas typically for 7 - 48 days. The sample area effective for D permeation is 3.7 cm^2. The D_2 gas pressure is

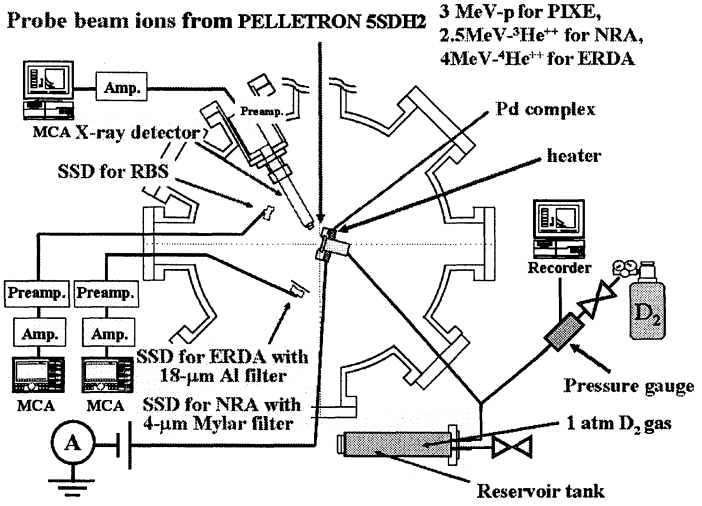

Fig.1. A schematic of experimental setup.

maintained at 0.04 - 0.1 MPa by occasionally replenishing the reservoir. The D flow rate through the complex sample was 0.01 – 0.15 sccm, which was calculated from the pressure change. We performed *in situ* analyses for characterization of the sample before, during and after D permeation; 3-MeV proton PIXE for elemental analysis, 2.5-MeV ^{3}He NRA or 4-MeV ^{4}He ERDA for D distribution analysis. The ^{4}He ERDA method has a spatial resolution of 80 - 100 nm. For monitoring the incident particle fluence RBS was applied simultaneously.

We will explain the experimental results regardless of the order in which they were made. We start with Run 6, 7 and 8 using CaO/Sr/Pd (n = 0) samples to replicate Run 1 described in ref. **2**. The samples were prepared as follows. At first the Pd bulk with a thickness of 0.1 mm was annealed for 3 hours at 570 K after 100 second immersion in aqua regia/D_2O. And Sr atoms were deposited on one side of the Pd bulk surface using electrochemical deposition method, by carefully placing the Pd bulk on the surface of the 10-mM $Sr(NO_3)_2/H_2O$ solution. Finally, a CaO layer with a thickness of 8 nm was deposited on the Sr/Pd samples. Each sample for Run 6, Run 7 and Run 8 has different areal density of Sr. And we kept the sample temperature at 70 °C during D permeation in Run 7 and Run 8. The rear surface of the Pd samples was exposed to D_2 gas at a pressure of 0.1 MPa typically for 49 days in Run 6, for the 26 days in Run 7 and for 20 days in Run 8.

In order to increase the number of nuclei to be transmuted, multilayered Pd samples were prepared for Run 4 and Run 5: The Pd bulk was annealed for 10 hours at 1170 K after 100 seconds immersion in aqua regia/H_2O. Sr atoms were then deposited on one side of the Pd bulk surface using electrochemical deposition method.

Next, for the sample of Run 4, a Pd layer with a thickness of 54 nm was deposited on the Sr/Pd surface by RF sputtering. We repeated the process of Sr deposition followed by Pd sputtering nine times to make a $(Sr/Pd)_9Sr/Pd$ sample. The sample of Run 5, $(CaO/Sr/Pd)_9/CaO/Sr/Pd$, was prepared by means of sputtering deposition of CaO and Pd layers with a thickness of 2 nm and 18 nm, respectively, in addition to electrochemical deposition of Sr on the Pd bulk.

Table1. Temporal variation of the areal densities of detected element during the permeation process in the R6 - 8.

6th	0.42 sccm			7th	0.06 sccm			8th	0.08 sccm		
Vacuum/CaO/Sr/Pd/D_2				Vacuum/CaO/Sr/Pd/D_2				Vacuum/CaO/Sr/Pd/D_2			
Time [h]	D fluence [10^{21} cm^{-2}]	Areal density [10^{15} cm^{-2}]		Time [h]	D fluence [10^{21} cm^{-2}]	Areal density [10^{15} cm^{-2}]		Time [h]	D fluence [10^{21} cm^{-2}]	Areal density [10^{15} cm^{-2}]	
		Sr	Mo			Sr	Mo			Sr	Mo
0	0	2.6 ± 0.2	5.0 ± 0.7	0	0	21.2 ± 0.3	1.3 ± 0.6	0	0	4.6 ± 0.2	1.2 ± 0.6
46	8.2	2.9 ± 0.7	3.4 ± 2.0	10	0.3	19.5 ± 0.3	1.9 ± 0.6	399	13.8	3.5 ± 0.2	1.0 ± 0.6
121	21.7	2.4 ± 0.2	3.5 ± 0.7	45	1.2	22.7 ± 0.3	0.8 ± 0.6	474	16.3	3.8 ± 0.2	1.0 ± 0.6
194	34.8	2.9 ± 0.2	2.3 ± 0.7	96	2.6	22.9 ± 0.3	1.2 ± 0.6				
1138	205	3.0 ± 0.2	2.8 ± 0.6	182	4.9	17.0 ± 0.3	0.3 ± 0.6				
1170	211	2.6 ± 0.2	4.7 ± 0.7	448	12.2	16.8 ± 0.4	1.2 ± 0.7				
				614	16.4	15.3 ± 0.3	1.1 ± 0.6				

3. Results and discussion

First, an example of the PIXE spectra is shown in Fig.2, and the results of the PIXE analysis in Run 6 through 8 are shown in Table 1, where the areal densities of Sr and Mo as measured with PIXE as a function of time or the permeating D fluence are listed. In every run we can hardly notice any element having the atomic number between 38 (Mo) and 46 (Pd). Moreover, we can hardly see any consistent change in the areal densities of Sr and Mo.

As a general tendency, the areal densities of Sr and Mo decrease with the permeating D fluence. A possible reason for the decrease might be sputtering by 3-MeV protons used as the probe beam for PIXE analysis. However, a simulation using a program ACAT have shown that contribution of sputtering to the decrease is 2 orders of magnitude smaller than the decrease observed or estimated as a tendency.

The typical examples of ERDA spectra obtained at 103 hours and 1120 hours after initiation of D permeation in Run 6 are shown in Fig.3(a). We notice an energy shift of the spectra, which is probably caused by sample deformation resulting in change (of about 3 degree, in the present case) in the recoil angle. We also notice small humps at the recoil particle energy of 1.3 MeV, below which recoil hydrogens (H) are detected. We assume here that the humps are caused by H atoms adsorbed on the surface, and extract the H component leaving a smoothly varying D spectrum.

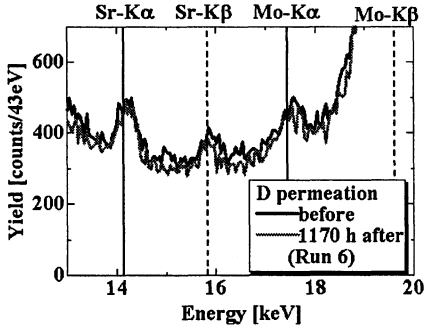

Fig.2. examples of the PIXE spectra

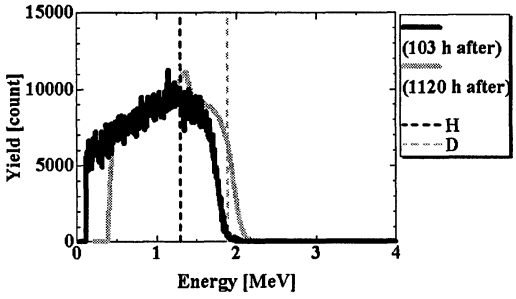

Fig.3(a). Typical examples of ERDA spectra.

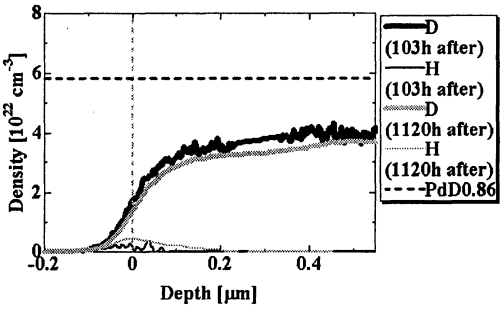

Fig.3(b). Depth profiles of the D and H densities.

The depth profiles of the D and H densities deduced from them are shown in Fig.3(b). The D density at 103 s of 3.8×10^{22} cm^{-3} averaged over the surface region up to the depth of 0.5 μm corresponds to the mean composition of $PdD_{0.56}$, and that at 1120 h of 3.4×10^{22} cm^{-3} corresponds to $PdD_{0.5}$. On the surface H concentration amounts 5 – 10 % of the total hydrogen isotope density, which is probably due to ion-beam-induced hydrocarbon deposition from gas phase contaminants. Since the distribution FWHM is almost the same as the spatial resolution of 100 nm, the H atoms are expected to be localized in the uppermost layer with little mixing with bulk D atoms.

These values mean that the D density is somewhat smaller then the saturation value, and suggest that what limits the D flow in the sample is not only recombination at the vacuum surface, but also by Pd bulk diffusion. The reason of insufficient blocking of the D flow by the CaO layer is unknown at present.

Both qualitatively and quantitatively similar result is obtained in Run 7, which gives the averaged composition of $PdD_{0.4}$ with very little surface contamination by H. In Run 8, however, we have rather large amount of contaminant H atoms, which is shown in Fig.4. We can hardly expect the CaO/Sr/Pd interface not affected by the existence of the H/D mixed layer extending deep into the sample. We don't have reasonable explanation of this exclusively large amount of H contaminants.

We could ascribe the apparently negative result of Run 6 through 8 to a probabilistic nature of the transmutation phenomenon. Iwamura *et al.* have found that the transmutation proceeds locally and inhomogeneously on the surface, and the number of points where it occurs increase with time randomly **[3]**. In this sense, XPS having a wide probe beam with a diameter of several mm is advantageous over PIXE with a beam diameter of 0.5 mm. Namely, it might be merely due to a premature permeation of D or insufficient number of nuclei to be transmuted.

Next, we discuss the results of Run 4 and 5 using multilayered samples prepared for the purpose of increasing the number of the atoms to be transmuted. Results of the PIXE analysis in the Run 4 and 5 are shown in Table 2.

In Run 4, an increase (4.6×10^{14} cm^{-2}) in the Mo areal density to compensate the decrease (5.7×10^{14} cm^{-2}) in the Sr areal density was observed until after 120 hours permeation. After leaving the system in the D flow for 12.7 days, however, both areal densities have recovered the initial values before permeation. The most optimistic explanation of this phenomenon might be sample deformation caused by D absorption and resultant change of analyzing spot on the sample. The above change is, however, within the range of experimental error.

Table2. Temporal variation of the areal densities of detected element during the permeation process in the R4 and 5.

4th		0.14 sccm		5th		0.10 sccm	
Vacuum/(Sr/Pd)$_9$/Sr/Pd/D$_2$				Vacuum/(CaO/Sr/Pd)$_9$/CaO/Sr/Pd/D$_2$			
Time [h]	D fluence [10^{21} cm^{-2}]	Areal density [10^{15} cm^{-2}]		Time [h]	D fluence [10^{21} cm^{-2}]	Areal density [10^{15} cm^{-2}]	
		Sr	Mo			Sr	Mo
0	0	3.7 ± 0.8	2.4 ± 0.6	0	0	30 ± 0.3	2.9 ± 0.07
42	4.2	3.3 ± 0.7	2.6 ± 0.6	50	3	28 ± 0.3	2.7 ± 0.07
100	8.3	3.2 ± 0.7	3.0 ± 0.7	80	3.8	27 ± 0.3	2.4 ± 0.07
145	11.7	3.1 ± 0.7	2.9 ± 0.7	115	5.3	24 ± 0.3	2.4 ± 0.07
422	33.3	3.7 ± 0.8	2.0 ± 0.5	145	7.2	24 ± 0.3	2.6 ± 0.07
				280	13.0	29 ± 0.3	2.3 ± 0.07

In this run the D distribution analysis was performed exceptionally using NRA, which has poorer resolution of about 150 nm. As shown in Fig.5, the measured D density of 5.9×10^{21} cm^{-3} averaged over the surface region up to the depth of 0.4 μm corresponds to the rather low concentration of $PdD_{0.09}$ at 60 h.

In Run 5, monotonic decrease in the areal densities of both Sr and Mo was observed. The D depth profiles at about 60 h and 115 h after initiation of D permeation are shown in Fig.6. The averaged composition of $PdD_{0.33\text{-}0.39}$ is deduced for these cases. The apparently negative results in Run 4 and 5 are then ascribed to the low D density in the sample or to the low permeation flux of D.

4. Summary

We have constructed an experimental system, with which accelerator analyses including PIXE, ERDA, NRA and RBS can be made *in situ* and simultaneously with gas permeation through the samples. We have then tried to replicate Run 1, in which nuclear transformation of Sr to Mo was suggested by XPS analysis. Up to the present, however, we have not yet confirmed occurrence of the transmutation in the present experimental system.

We have also tried to increase the number of transmutation nuclei by making the multilayered sample of $(CaO/Sr/Pd)_n/CaO/Sr/Pd$. An increase (4.6×10^{14} cm^{-2}) in the Mo areal density compensating a decrease (5.7×10^{14} cm^{-2}) in the Sr areal density was observed until after 120-hour permeation. After leaving the system in the D flow for 12.7 days, however, both areal densities have recovered the initial values before permeation. Although these changes are consistent and the reverse change could be reasonably explained by sample deformation, they are within the range of experimental error. Taking account of the experimental results that transmutation takes place locally and inhomogeneously, it is necessary to increase the permeation D flux as well as the areal densities of D and the transmutation nuclei in the sample.

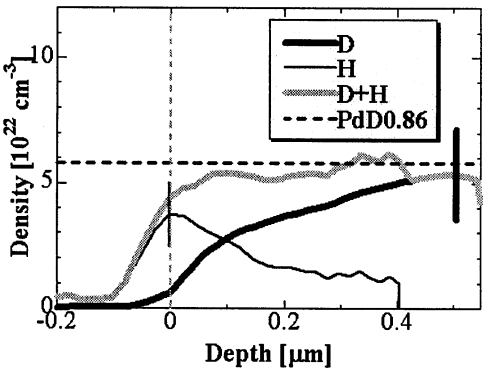

Fig.4. Depth profile of the D density in Run 8.

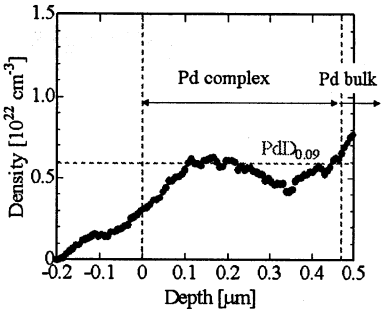

Fig.5. Depth profile of the D density in Run 4.

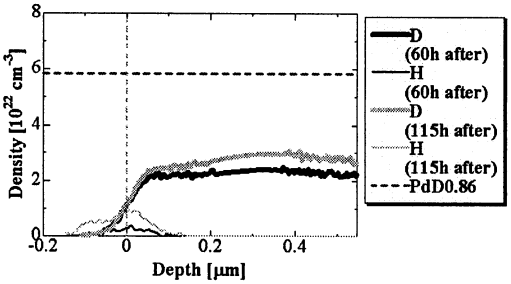

Fig.6. Depth profile of the D density in Run 5.

References

1. Y. Iwamura, M. Sakano and T. Itoh; Jpn. J. Appl. Phys. 41 (2002) 4642-4650.
2. A. Kitamura, R. Nishio, H. Iwai, R. Satoh, A. Taniike and Y. Furuyama; Proc. ICCF12, 2005, Yokohama, Japan, (World Scientific Publishing Co. Pte. Ltd, 2006) 272-277.
3. Y. Iwamura *et al.*; Proc. ICCF12, 2005, Yokohama, Japan, (World Scientific Publishing Co. Pte. Ltd, 2006) 178-187.

Radiation Measurement during Gas Permeation Experiment

Yu TORIYABE and Jirohta KASAGI

Laboratory of Nuclear Science, Tohoku University
Mikamine 1, Taihaku-ku, Sendai 982-0826, Japan
E-mail: toriyabe@lns.tohoku.ac.jp

A detector system was developed in order to measure high energy α particles in gas permeation experiments. A YAP(Ce) scintillator with a photomultiplier tube was employed as the detector and a pulse shape discrimination (PSD) technique was developed to identify species of radiations. All output pulses from the photomultiplier tube were recorded by a digital storage oscilloscope. In the off-line analyses, the pulses can be categorized. Most of the pulses are normal scintillations originated mainly from charged particles and show a rise time of about 5 ns and a decay time of about 30 ns. In a long period of the gas permeation, however, anomalous pulses were observed in every run. Although some of them can be rejected as originated from electrical noise, pulses having a huge amplitude and a short decay time may be a candidate of direct light emission from the sample foil. We discuss on a small peak observed at low energy region, which indicates the possibility of light emission or 3-MeV proton emission associated with the D+D reaction.

1. Introduction

Anomalous nuclear reactions have been reported in a gas loading system such as electrical discharge, gas permeation, gas desorption and so on[1]. Since these experiments are carried out at low pressures or in a vacuum chamber, charged particles from nuclear reactions can be measured, while one cannot detect them except neutrons in an electrolysis system.

In this study, we carried out charged particle measurement in a D_2/H_2 gas permeation system which is fully based on experiments conducted at Mitsubishi Heavy Industries, Ltd (MHI)[2-5]. If the same condition as MHI were achieved, high energy α particles (~23.8MeV) could be measured in this system.

Here, radiation during CMNS experiments is so weak that we have to reduce background counting to a level as low as possible and improve reliability of particle and energy identification. In this view point, we introduced pulse shape discrimination (PSD) technique to analyze very rare events. We recorded all electrical signals from detector systems by a digital storage oscilloscope. After experiments, we checked all signals carefully and identified differences between background and foreground.

2. Experiment

2.1. Detector system

Although it is widely recognized that Si semiconductor detector is the best for charged particle detection, it is passivated in H_2/D_2 gas environment and energy resolution becomes worse. In the case of MHI-type experiments, charged particle emissions are expected to occur not at vacuum side but at gas side. Therefore we selected a scintillation detector.

Typical inorganic scitillators such as NaI(Tl) and CsI(Tl) have hygroscopicity and dependence of light yield on temperature as liquid organic scintillators for high energy neutron energy spectroscopy such as NE213 do[6-8]. Hence we selected a Cerium doped Yttrium Aluminium Perovskite ($YAlO_3$) scintillator (YAP(Ce)), which shows good chemical stability and little temperature dependence[9,10]. This scintillator is connected to a quartz light guide and a photomultiplier tube under a shading condition.

Plastic scintillators placed below the chamber served as veto counters to reject cosmic-ray events. All of these detectors are connected to not only NIM and CAMAC modules but also digital oscilloscope to record all pulses with record length of 500 ns per 1250 channels. A schematic view of the experimental setup is shown in Fig. 1

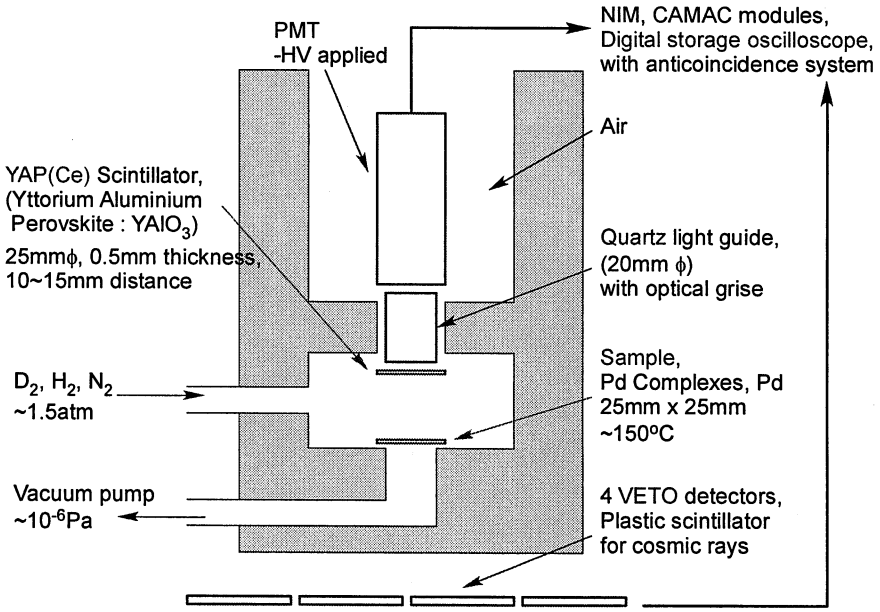

Figure 1. Experimental setup.

2.2. Procedure

Pd samples were provided from MHI and Toyota Central R&D Labs., Inc. (TCL). The composition is just same as theirs without Cs deposition.

D_2/H_2 gas pressure was kept at about 1.5 atm (1.6 atm at maximum). The opposite side is evacuated below 10^{-5} Pa. Temperature of the sample can be controlled by a heater. During permeation we measured the temperature at outside of the chamber near the sample, where temperature is lower than that of the sample. We elevated the temperature to 140 °C at maximum and ignored light yield change of YAP(Ce).

In this series, permeation rate is much lower than 1ccm. Thus we could not replicate the MHI condition.

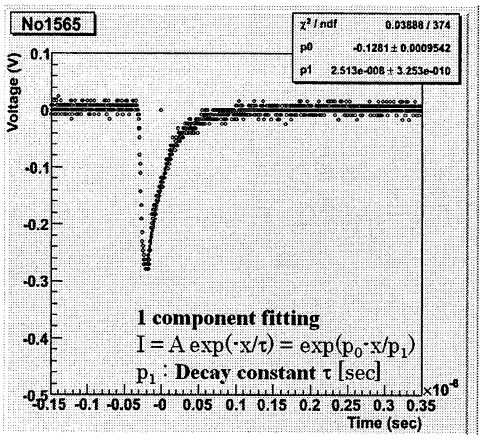

Figure 2. Pulse shapes of 5.5MeV α particles from an ^{241}Am checking source.

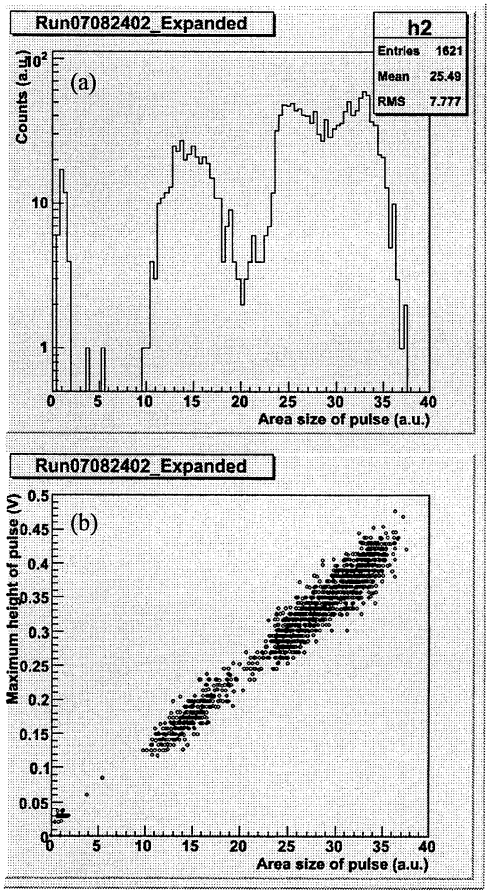

Figure 3. (a)Charge integrated energy spectrum of 5.5MeV α particles from an ^{241}Am checking source. (b)Relation between the energy and pulse height.

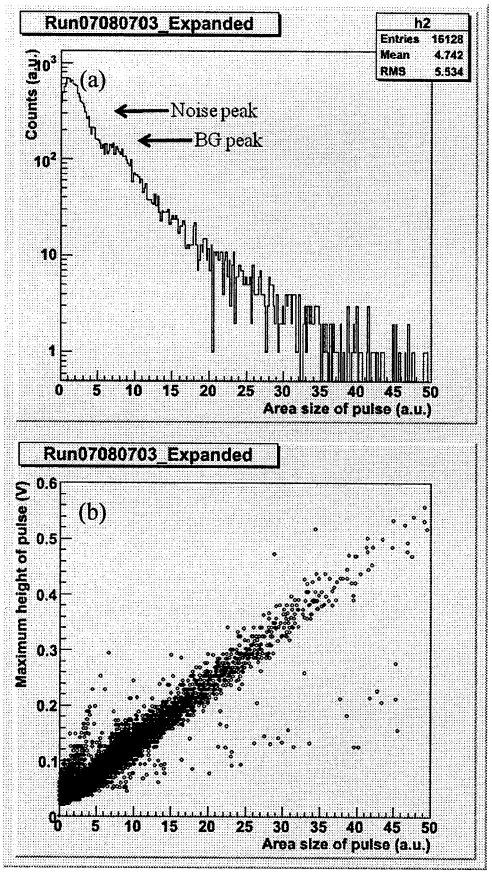

Figure 4. (a) Energy spectrum recorded during the first 17 hours of D_2 gas permeation through the Pd complexes supplied by MHI Lab. (b) Plot of the pulse height vs. energy. High energy tail and anomalous plots separated from normal linear relation appeared.

3. Results

3.1. Calibration

First, we measured α particles from ^{241}Am checking source. Figure 2 shows recorded pulses of 5.5MeV α particles. Decay constant was evaluated by 1 component fitting as 25 nsec which agrees with that found in some references[9,10].

From these pulses, we obtained a charge integrated energy spectrum shown in Fig. 3. Obviously, there are 3 peaks. At present we cannot identify the cause of the phenomenon but conjecture that reflection of scintillation light would have led to 3 peaks.

3.2. Gas permeation

Figure 4 shows an energy spectrum during D_2 gas permeation through Pd complexes from MHI. A high energy tail is observed during permeation. These counts are not normal shape pulses because relation between charge integrated energy and the maximum height of that pulse is different from the normal linear relation. This means that these are anomalous shape pulses.

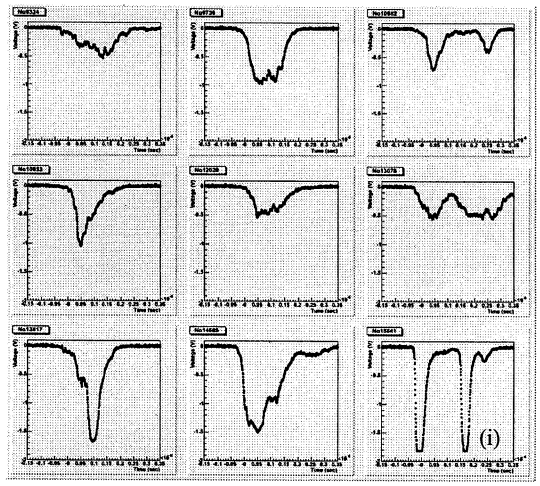

Figure 5. Anomalous pulses observed during the first 17 hours of D_2 gas permeation through the Pd complex supplied by MHI lab. Two kinds of pulses were detected. The first one has complicated shape, while the second has a very small rise time and a very small decay time as shown in (i).

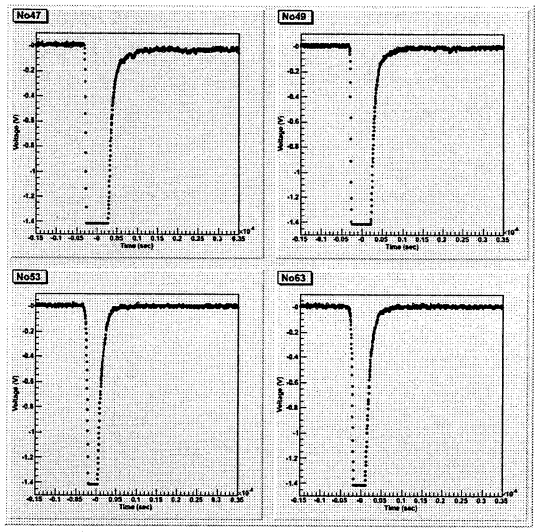

Figure 6. Anomalous pulses observed during D_2 gas desorption from Pd complex supplied by MHI lab, after D_2 gas permeation. Large and sharp pulses were only observed in the first few minutes.

Figure 5 shows examples of these anomalous pulses during D_2 gas permeation which are clearly different from charged particle signals as shown in Fig. 2. There are 2 kinds of pulses. First one is a complex pulse. The second has very large pulse

height and small decay time. These pulses were observed throughout the period of permeation, in both cases of D_2 and H_2 gas, from both samples provided by MHI and TCL labs.

3.3. *Pumping*

After gas permeation, we pumped out D_2/H_2 gas. Then anomaly appeared again as shown in Fig. 6. The large and sharp pulses were observed only in the first few minutes of pumping. These pulses are not originated from scintillation because decay constant is too small. At present we ascribe them to burst emission of light. If the sample emits not charged particles but light, photons pass through the scintillator without interaction and reach the photomultiplier. Then the photon bursts are amplified electronically without the scintillation process which causes large pulse height and small decay constant.

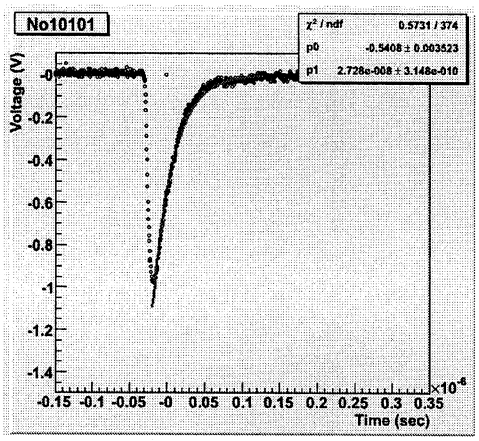

Figure 7. Pulse shape of high energy event after discrimination process. Shapes are normal and the decay constant agrees with that of ^{241}Am pulses.

3.4. *Discriminaion*

We discriminated anomalous pulses from normal pulses to search charged particle emissions. In this process normal pulses are defined as the events after following discrimination processes,

i) rejecting the cosmic rays,

ii) rejecting the low energy events by sufficiently high threshold level,

iii) rejecting pulses with anomalous decay constant,

iv) rejecting multi-pulse events within the record length.

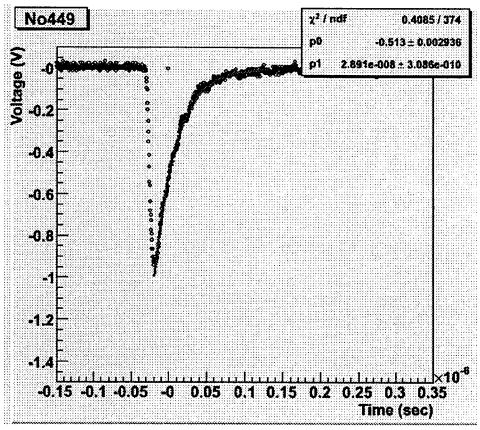

Figure 8. Pulse shapes of high energy cosmic rays. Shapes are almost same as anti-coincidence events shown in Fig. 7

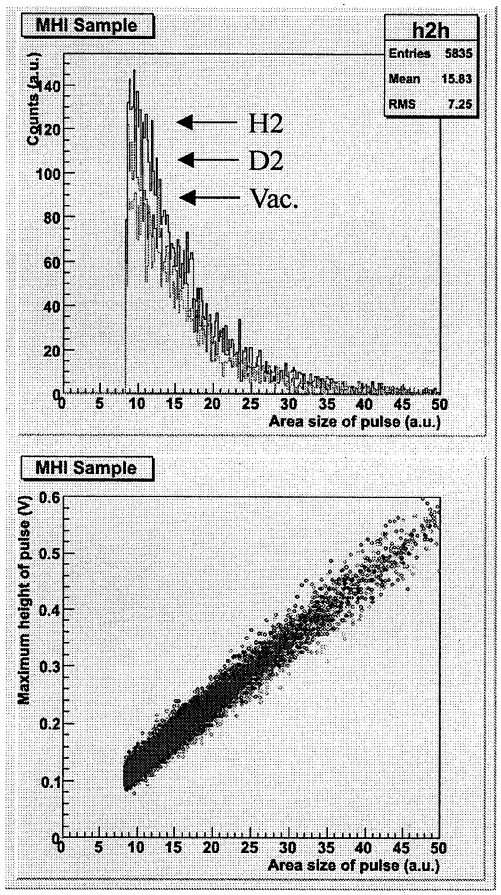

Figure 9. Energy spectrum of normal pulses during D_2/H_2/Vac. permeation through Pd complex supplied by MHI lab.

There still exists large pulses whose shapes are normal. Examples of these pulses are shown in Fig. 7 and cosmic rays are shown in Fig. 8. Cosmic rays, mainly muons, do not deposit meaningful amount of energy in such a thin

scintillator. However, the large pulses were coincident with those detected by veto detectors

This would mean that pulses with such large amplitude are produced as a result of interaction between cosmic rays and stainless steel chamber.

Figure 9 shows an energy spectrum for normal pulses measured under D_2/H_2/Vacuum permeation conditions. A spectrum for anomalous pulses is shown in Fig. 10.

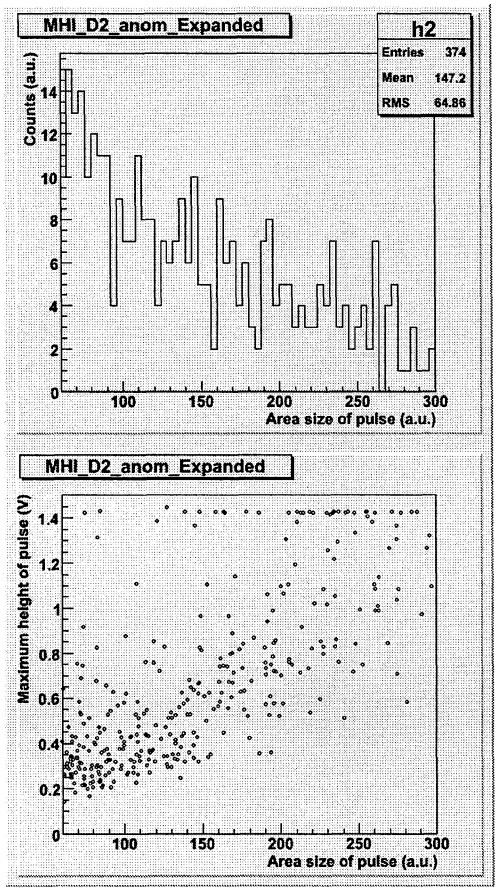

Figure 10. Energy spectrum of anomalous pulses during D_2 gas permeation through Pd complex supplied by MHI lab.

3.5. *Improvement*

There still exists a possibility that the pulses with anomalous shape are electrical noise. We carefully checked sources of noise, and improved the detector system. First, we changed the photomultiplier tube for new one. Next, we fixed quartz light guide tightly to prevent moving with changing pressure. After these improvements, we set a new Pd complex sample with Cs deposition provided by MHI lab. Then anomalous pulses disappeared except rarely detected pulses with a rate of under 0.05 cph. At present we cannot identify which is the reason of disappearance, the sample or the electrical noise. However, we now infer that complex pulses might be noise, while we still cannot reject the possibility of burst light emission in the case of large and sharp pulse.

Figure 11 shows energy spectra in the new experimental setup. Here gain was decreased so that 5.5MeV α particles from the ^{241}Am checking source are found at 13.5 a.u. Foreground spectrum is almost same as background. There is a little difference at a region of 15-20 a.u., though it is still within statistical error.

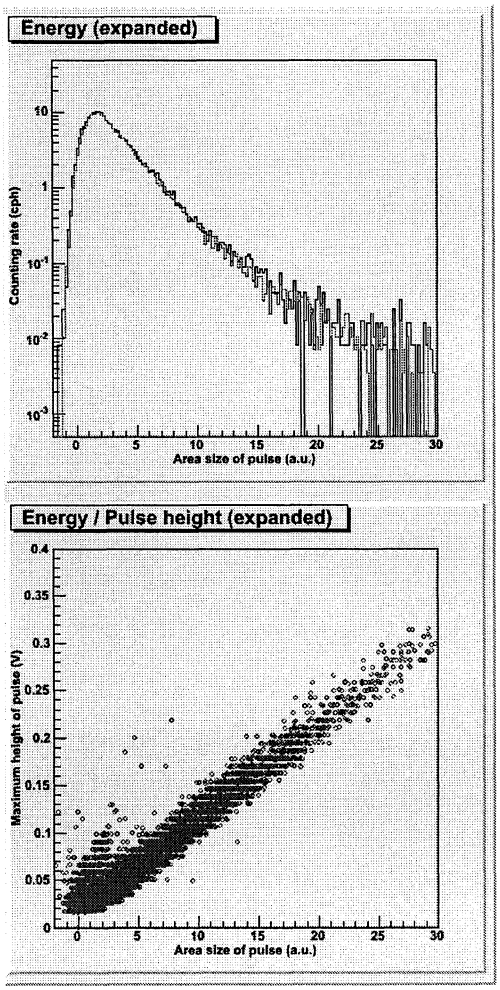

Figure 11. Energy spectra during D_2/Vac. gas permeation through Pd complex with Cs deposition supplied from MHI lab, in the improved system. The counting rate of both conditions are almost same.

On the other hand, we confirmed a little peak which has 3σ difference from background, at low energy region shown in Fig. 12. This could be

caused by light emission or 3 MeV proton from normal D+D reaction. Since we have not measured a light yield curve for YAP:Ce, we cannot identify the energy of this peak. In general, the light yield at lower energy does not have linear relation with the energy deposited. Furthermore, we need to change the region of interest to the lower energy for precise measurement of this small peak.

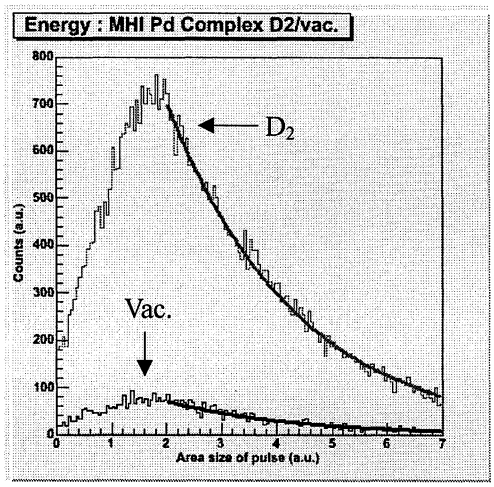

Figure 12. Small peak at low energy region during D_2 gas permeation through Pd complex with Cs deposition supplied by MHI lab, in the improved system.

Except this small peak, the foreground is almost same as the background as shown in Fig. 11. It is difficult to discuss the anomaly anymore in the present detector system. The other technique to decrease background to quite low level is strongly required.

4. Conclusion

We have conducted radiation measurement during gas permeation experiment with the YAP(Ce) scintillator, which shows good chemical stability and little temperature dependence, and the technique of pulse shape discrimination using digital storage oscilloscope. As a result, two kinds of anomalous pulses were detected during permeation and pumping. This anomaly was observed in both cases of D_2 and H_2 run, using Pd complexes without Cs deposition provided from MHI and TCL labs. However, these pulses disappeared after improvement of experimental setup.

Although the first type of anomalous pulse, namely the complex pulse, would be noise, we cannot abandon the possibility of burst light emission for the second type pulse. Furthermore, the small peak at low energy might be caused by small light emission or 3 MeV proton from normal D+D reaction. To identify this signal precisely the region of interest should be shifted to the lower range.

The background counting rate is so high that a clear evidence of LENR has not been obtained at present. Another technique to reduce background counts is necessary to forward the next step.

Furthermore basic data, namely dependences of light yield on the temperature and energy, and decay constant for each charged particle and so on, are required for precise measurement.

We now plan to measure the temperature dependence of YAP(Ce) for α particles and develop a new detector system for precise measurement.

Acknowledgement

Pd complexes samples were provided from Mitsubishi Heavy Industries, Ltd and Toyota Central R&D Labs., Inc. Authors would like to thank CMNS researchers at those laboratories.

This study is partially supported by JSPS grant.

References

1. A. Takahashi, *Proc. ICCF12*, 1, 2006.
2. Y. Iwamura *et al.*, *Jpn. J. Appl. Phys.*, **41**, 4642, 2002.
3. Y. Iwamura *et al.*, *Proc. ICCF10*, 24, 2003.
4. Y. Iwamura *et al.*, *Proc. ICCF11*, 339, 2004.
5. Y. Iwamura *et al.*, *Proc. ICCF12*, 178, 2005.
6. G. F. Knoll, *Radiation detection & measurement: 2nd ed.*
7. W. R. Leo, *Techniques for nuclear & particle physics experiments.*
8. T. Akimoto *et al.*, *Proc. ICCF6*, 295, 1996.
9. S. Baccaro *et al.*, *Nucl. Instr. & Meth. A*, **361**, 209, 1995.
10. M. Moszynski *et al.*, *Nucl. Instr. & Meth. A*, **404**, 157, 1998.

PRODUCING ELEMENTS OF MASS NUMBER 137 AND 141 BY DEUTERIUM PERMEATION ON MULTI-LAYERED Pd SAMPLES WITH Cs DEPOSITION

H. YAMADA, S. NARITA, D. SATO, T. USHIROZAWA, S. KURIHARA, M. HIGASHIZAWA, K. IIDA, H. OHATA and H. NANAO*

Department of Electrical and Electronic Engineering, Iwate University, Ueda 4-3-5, Morioka, 020-8551 Japan *yamadahi@iwate-u.ac.jp*

* Department of Chemical Engineering, Iwate University, Ueda 4-3-5, Morioka, 020-8551 Japan

Abstract: An elemental analysis of Pd samples after deuterium permeation experiment was performed using TOF-SIMS. The TOF-SIMS has provided the marked count peaks at mass numbers 135 and 137 in spectra after deuterium permeation at 70℃, only when the multilayered Pd sample with a small amount of Cs was used. The substance with mass number 137 could be ^{137}La, ^{137}Ba or ^{137}Cs. They were produced during deuterium permeation by some nuclear transmutation occurring on/in the uppermost of multi-layered Pd sample. The single and five couples of Pd/CaO thin films on Pd foil might contribute to induce production of an element with mass number 137. This would imply a transmutation of 4 mass number increasing before ^{141}Pr production.

Keywords: Pd-deuteride, Deuterium permeation, Transmutation, TOF-SIMS, Surface analysis

1. Introduction

Nuclear transmutation from a selected element into another one at near room temperature is of interest to give important information for constructing a standard model of low energy nuclear reaction. Among several experimental methods for the transmutation, the gas permeation method is one of the promising methods. Applying this method to Pd film complexes, Iwamura et al. reported a low energy nuclear transmutation from Cs into Pr and from Sr into Mo [1]. They used five couples of Pd/CaO thin films on a basal bulk Pd foil in their experiment. Kitamura et al. have investigated the transmutation from Sr into Mo using another permeation method and have revealed that the transmutation takes place between the thin film and the base Pd foils.[2]

We have taken advantage of these gas permeation method to perform the transmutation from Cs into Pr using single couple of Pd/CaO thin films instead of the five couples. We have not observed marked amount of Pr but detected a small amount of substance with mass 137 using TOF-SIMS [3, 4]. Next, we have performed several reference experiments to search for the formation of the substance of mass number 137. The substance with mass 137 has not observed for these reference experiments; the series of test gave a strong suggestion that the substance of mass 137 formed during the D_2 gas permeation through the multi-layered Pd sample was a newly produced element ^{137}La, ^{137}Ba or ^{137}Cs.

It might be possible that the result in almost no production of Pr in our experiment was due to the low number of the couple of Pd/CaO thin films. Thus, in this present investigation, we have compared the result for samples with single couple with that for five couples of Pd/CaO films after the deuterium permeation experiment.

2. Experimental

The experimental method and setup to investigate the transmutation of Cs into other elements of larger mass number are basically the same as before.[3, 4] The multi-layered sample consisted of single or five couples of CaO and Pd thin films on the basal Pd foil of 0.1×12.5×12.5mm in size. The CaO and Pd thin films were formed in this order on the Pd foil by Ar ion beam sputtering. After forming the thin films, small amount of Cs was deposited on the multi-layered Pd sample by an electrochemical method. Each thickness of

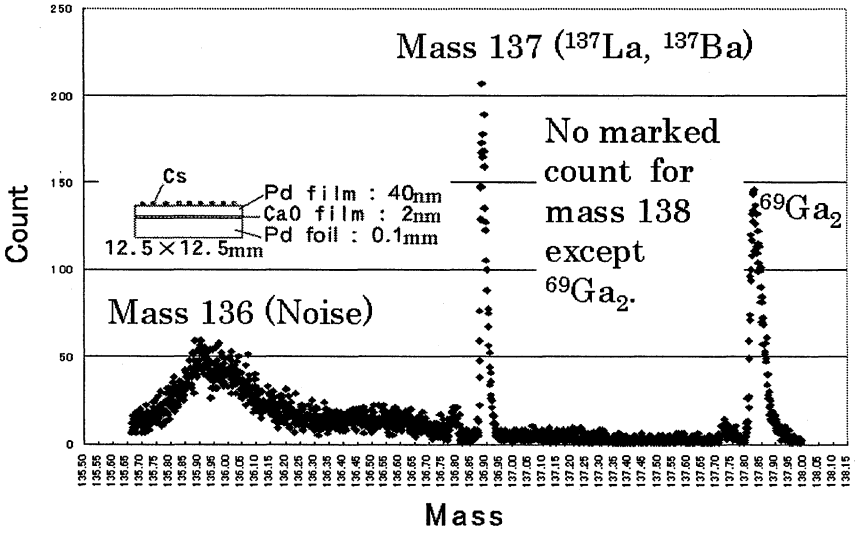

Fig. 1 TOF-SIMS spectrum around mass number 137 for a multi-layered Pd sample with single couple of Pd/CaO thin films after deuterium permeation.

CaO and Pd films formed were 2 and 18 nm, respectively. Only the thickness of uppermost Pd film was 40-50 nm. No deuterium gas was loaded to the samples before deuterium permeation experiment.

The chamber was usually filled with N_2 gas under non-experiment condition.

Just before the permeation experiment, the Pd samples were set into the sample holder in an air environment and it was placed at the vacuum chamber.

Then, the chamber was filled with deuterium gas at a pressure 0.1 or 0.2 MPa; the thin Pd film side of multi-layered Pd sample with small amount of Cs was exposed to D_2 gas. The other side of sample was evacuated by a turbo molecular pump. The deuterium permeated from the chamber through the Pd sample to the evacuated side by the pressure gradient for about 2-4 weeks. A heater was employed to keep the temperature of the chamber at 70℃ during the experiment.

After the permeation experiment, the heater is turned off and the chamber was filled with N_2 gas, then the sample ("Permeation sample") was taken out from the holder. The sample surface of gas-filled side was analyzed by Time-of-flight secondary ion mass spectroscopy (TOF-SIMS) (ULVAC-PHI: TFS-2100).

The primary ion in TOF-SIMS was Ga^+ and we measured at least three randomly selected areas of 40×40 micron square. The spectra were obtained before and after a sputter cleaning of the uppermost surfaces of samples by the Ga^+ for 5-10 sec. In order to take into account the contamination from the environment, we prepared the control sample ("Control sample") without flowing the deuterium gas, which was prepared by the same procedure for the permeation samples.

3. Result and Discussion

TOF-SIMS spectrum of mass number range 136-138 after sputter cleaning for a sample with single couple of Pd/CaO thin films is presented in Fig. 1. The schematic view of cross-section of sample is shown in this figure. An anomalous peak is seen at mass number 137. Another anomalous peak was also observed at mass number 135 for the same measured area, even though the count intensity was lower than that of the mass 137. These peaks were not observed for control samples. Considering the difference between the measured mass of substance with mass 135 and that of ^{135}Ba, the substance seems to be molecule CsD. The peak observed at mass 136 could be due to

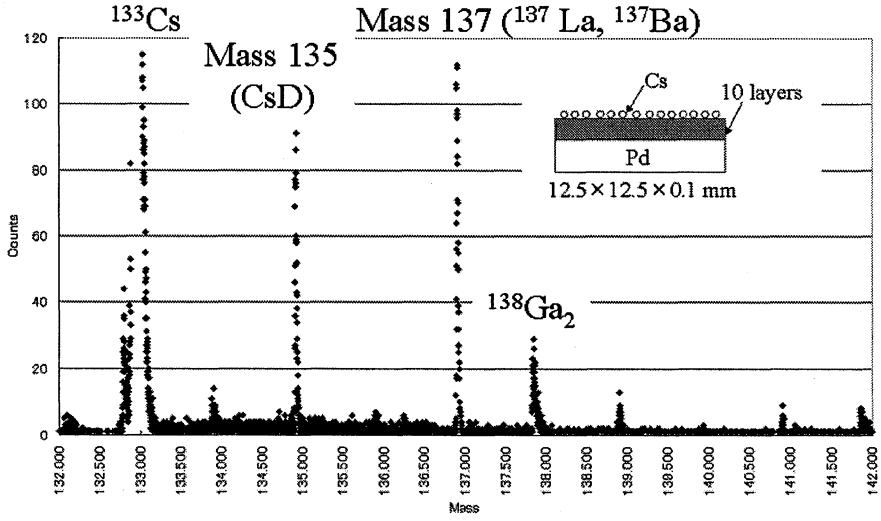

Fig. 2 TOF-SIMS spectrum of mass number range 132-142 for a multi-layered Pd sample with five couples of Pd/CaO thin films after deuterium permeation.

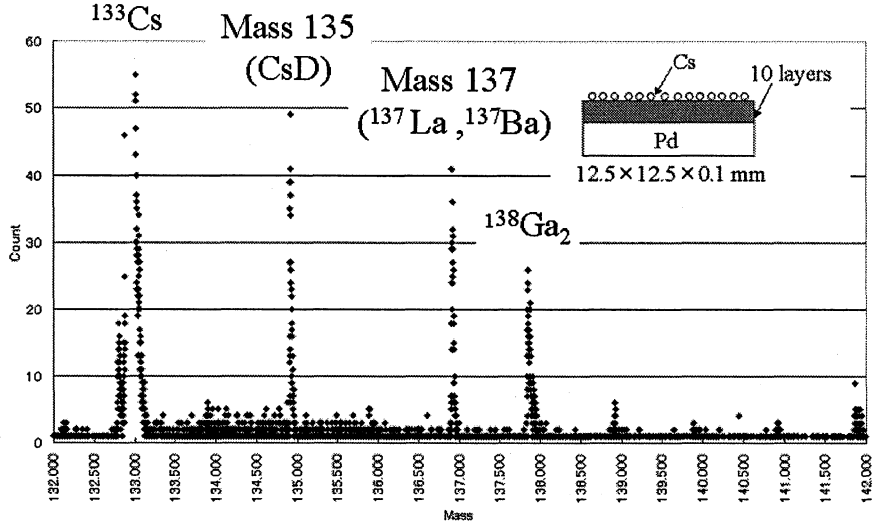

Fig. 3 TOF-SIMS spectrum of mass number range 132-142 for a multi-layered Pd sample with five couples of Pd/CaO thin films after deuterium permeation.

nose signal relating to the TOF-SIMS characteristics.

Similar spectrum for a multi-layered Pd-base sample with five couples of Pd/CaO thin films is shown in Fig. 2 and 3. Similar peaks as that for single couple of Pd/CaO thin films are seen at mass 137 in these figures. The peak intensity at mass 137 is higher than that at mass 135 in Fig. 2. However, the peak intensity at mass 137 in Fig. 3 is slightly lower than that of mass 135; such lower peak at mass 137 was sometimes observed. This indicates that the formation process for the substances of mass 135 is independent of that of mass 137.

Table 1 gives the candidates of the substances of mass 137. The peak position of Cs on TOF-SIMS spectrum was the standard against which we have measured the peak position of substance of mass number 137.

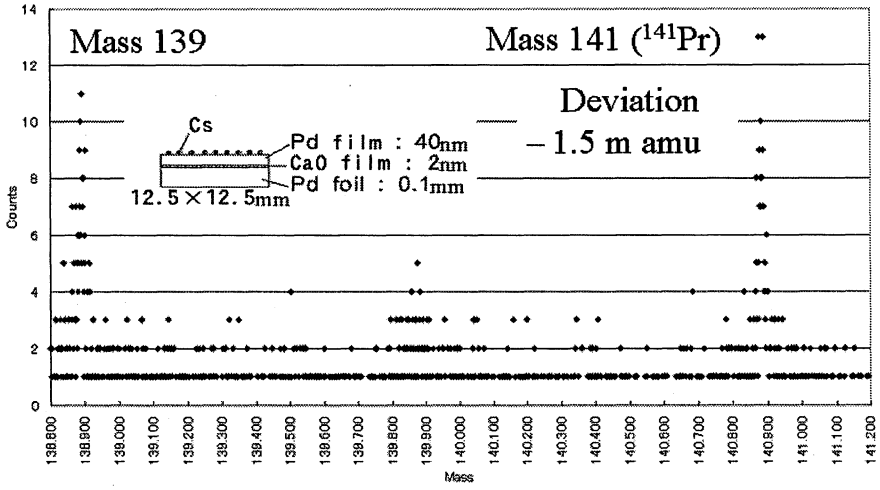

Fig. 4 TOF-SIMS spectrum of mass number range 139-141 for a multi-layered Pd sample with five couples of Pd/CaO thin films after deuterium permeation.

The peak deviation in the Table 1 is defined as the difference between the measured mass number and each real mass number of substance, that is, 136.9065-(each real mass number).

Table 1. Candidates of the substances with mass 137

	Mass (amu)	Peak deviation (m amu)
CsD_2	136.9336	-27.1
$^{106}PdOCH_3$	136.9219	-15.4
^{137}Ba contaminant		
^{137}La	136.9065	0.0
^{137}Ba	136.9058	0.7
^{137}Cs	136.9071	- 0.6

As mentioned above, the count intensity observed at mass 137 was usually higher than that observed at mass 135. This is the characteristics commonly observed in almost all the samples and almost all the measured areas. In general, amount of CsD formed by chemical process during the deuterium permeation experiment is thought to be much more than that of CsD_2. Accordingly, the substance corresponding to mass 137 cannot be CsD_2. Furthermore, the absolute value of peak deviation -27.1 m amu for CsD_2 in the Table 1 is enough lager than that of ±3 m amu, which is the rough value of the error range. This also ascribes that the substance of mass 137 must not be CsD_2.

We have reported that a Pd compound of $PdOCH_3$ could be formed at the uppermost surface of multi-layered Pd sample after the D_2 Permeation [4]. This means that small amount of $PdOCH_3$ would be exist on the surface of the sample even after the sputter cleaning. On the basis of Pd natural isotopic abundance, the amount of Pd isotopic compounds formed should be proportional to the abundance values. The natural isotopic abundance of ^{105}Pd, ^{106}Pd and ^{108}Pd are 22, 27 and 26%, respectively. It should have been expected that count intensity at mass 139 by $^{108}PdOCH_3$ was as large as that at mass 137 when the substance of mass 137 was $^{106}PdOCH_3$. In other wards, a marked count due to $^{108}PdOCH_3$ should have been seen at mass 139 in Fig. 2 and 3. However, there existed a peak of extremely low count intensity at mass 139. Consequently, the contribution of $^{106}PdOCH_3$ to form the peak at mass number 137 is thought to be negligible. The absolute value of peak deviation -15.4 for $^{106}PdOCH_3$ in Table 1 is enough larger than that of the rough value of the error range. Furthermore, no marked peak appeared at

mass number 136, which corresponds to the mass number of $^{105}PdCOH_3$. Considering the fact that Pd has large natural isotopic abundance in mass number 105, 106 and 108, the compounds of ^{106}Pd cannot account for the marked count at mass 137 in Fig 1, 2 and 3. Therefore, molecule $^{106}PdOCH_3$ is out of the candidate substance.

Similarly, on the basis of Ba natural isotopic abundance, the amount of Ba isotopic compounds formed should be proportional to the abundance values. The natural isotopic abundance of ^{137}Ba and ^{138}Ba are 11 and 72%, respectively. Thus, the element of ^{137}Ba contaminant can be possible candidate only when remarkably large count intensity was observed at mass 138. To the contrary, we have not recognized such large peak at mass 138 as seen in Fig. 1, 2 and 3, where only a peak corresponding to Ga_2 is seen. This implies that the substance of mass 137 must not be ^{137}Ba contaminant.

Thus, the substance of mass number 137 observed only after deuterium permeation and only with Cs deposition is unlikely to be contaminants but would be an elements ^{137}La, ^{137}Ba, or ^{137}Cs. Among these three possible candidates, ^{137}La might be the most likely candidate, because only the transmutation from ^{133}Cs into ^{137}La takes place via an alpha particle formation. There are other unstable ten candidate elements with mass 137, including such as ^{137}Xe. However, these elements have relatively short half life of time range s-h. Thus, we have excluded these ten elements from the possible candidates.

A TOF-SIMS spectrum of mass number range 139-141 after sputter cleaning for the multi-layered Pd sample with single couple of Pd/CaO thin films is shown in Fig. 4. It is interesting to note that the count intensity at mass 141 is often slightly higher than that at mass 139 as seen in Fig. 4, even though both intensities are relatively low. The absolute value of peak deviation -1.5 of the substance with mass 141 is within the that of the rough error range ± 3 m amu. This provides a possibility that the detected substance of mass 141 might be ^{141}Pr. Considering the results of experiment by Iwamura et al. [1], all the results obtained in this study suggest an important role of alpha cluster in the transmutation process of 4, 8 and 12 mass number increasing.

4. Conclusion

TOF-SIMS was employed for elemental analysis of surface of multi-layered Pd-base samples with single and five couples of Pd/CaO thin films. The TOF-SIMS has provided the marked count peaks at mass 137 in spectra after deuterium permeation at 70℃, only when a small amount of Cs was deposited on the uppermost surface of sample. The result suggests production of an element with mass 137 which would be produced from ^{133}Cs. The substance with the mass 137 could be ^{137}La, ^{137}Ba or ^{137}Cs. They were produced during deuterium permeation by some nuclear transmutation occurring on/in the uppermost of multi-layered Pd sample. The single and five couples of Pd/CaO thin films on Pd foil might contribute to induce production of an element with mass number 137. This would imply a transmutation of 4 mass number increasing before ^{141}Pr production.

Acknowledgment

The authors acknowledge for the support of TEET (The Thermal and Electric Energy Technology Foundation).

References

1) Y. Iwamura, T. Itoh and, M. Sakano, Jpn. J. Appl. Phys., 41, 4642 (2002).
2) A. Kitamura, R. Nishio, H. Iwai, R. Sato, A. Tanike and Y. Furuyama, Proc. 12th International Conference on Cold Fusion, p. 272 (2006).
3) H. Yamada, S. Narita, S. Taniguchi, T. Ushirozawa, S. Kurihara, M. Higashizawa, H. Sawada and M. Itagaki, Proc. 12th International Conference on Cold Fusion, p. 196 (2006).
4) H. Yamada, S. Narita, S. Taniguchi, T. Ushirozawa, S. Kurihara, M. Higashizawa and M. Itagaki, Proc. 7th Meeting of Japan CF Research Society, p. 28 (2006).

Proceedings of JCF8, November 29-30, 2007, Doshisha University, Kyoto, Japan

Change of Coulomb Potential of Electron due to Band Structure in Semiconductor

Shigeru Sasabe*) (Tokyo Metropolitan University)

Ken-ichi Tsuchiya**) (Tokyo National College of Technology)

Kyo-ta Watanabe (Tokyo Metropolitan University)

E-mail: *) s-sasabe@tmu.ac.jp **) tsuchiya@tokyo-ct.ac.jp

Abstract

The quantization of Lorent-Dirac equation leads to a weakened Coulomb barrier for the charged particle. This weakened Coulomb potential depends on some critical length Rc. Unfortunately, Rc is two small to achieve some effect in vacuum. However, it is expected that Rc becomes large in material and overcomes the Coulomb barrier to facilitate the nuclear reaction. Our expectation is examined by the use of band electron in semiconductor. We find positive results.

Keywords: Cold fusion, Coulomb potential, Band structure, Spin-magnetic moment, Zitterbewegung

1. INTRODUCTION

By quantizing Lorentz-Dirac equation, we obtain weakened Coulomb potential [1][2]

$$U(r)=\frac{e^2}{r}\left[1-\exp\left(\frac{-r}{2R_c}\right)\cos\left(\frac{r}{2R_c}\right)\right], \quad (1)$$

which is composed of the original coulomb potential with a damping factor. Here, r is the distance between two charged particles, and $2R_c$ is called 'critical length' in the sense that the damping factor decreases rapidly when r becomes smaller than $2R_c$.

We can make the same potential as Eq.(1) in the context of classical theory when two charged particles, whose effective size of charge distribution is about R_c, are at distance r (Fig.1). Usually, the transmission probability of a incident particle through the Coulomb barrier of nuclear is extremely small. Since the damping factor in the weakened Coulomb potential Eq.(1) begins to work when r is close to $2R_c$, it is expected that the potential barrier and the transmission probability changes drastically, depending on the value of R_c.

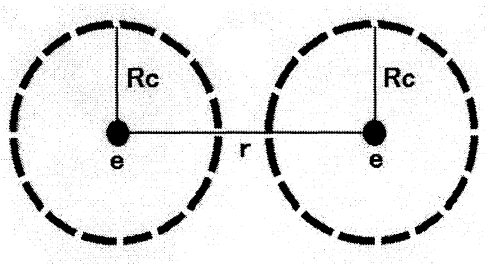

Fig.1. Classical analogy of the weakened potential U: Extended charges with effective radius R_c.

In the next section, thus we discuss the

effect of the critical length $2R_c$ on the Coulomb potential in anticipation of reduction in Coulomb barrier for low energy nuclear dynamics.

2. COMPARISON BETWEEN THE WEAKENED COULOMB POTENTIAL AND ORIGINAL POTENTIAL

The comparison of the weakened Coulomb potential U and the original Coulomb potential V_0 is shown in Fig.2 and Fig.3. As seen in Figure 2, in the region where r is large, two particles are far away each other, U and V_0 are almost equal. As particles are close, the difference between U and V_0 appears. When r is at $2R_c$, the value of U decrease 20% less than that of V_0.

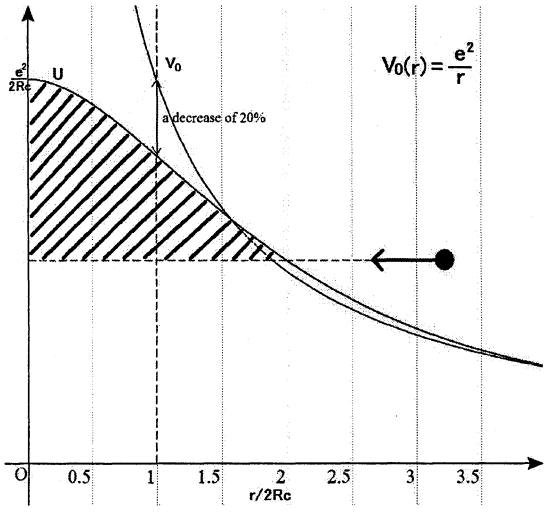

Fig.2. The comparison of the weakened Coulomb potential U and the original Coulomb potential V_0

We consider here the transmission probability of electron through the weakened coulomb potential. According to the WKB method[3], the transmission probability T is given as

$$T \approx \exp\left(-\frac{2}{\hbar}\int\sqrt{2m(U-E)}dx\right), \quad (2)$$

where m is the mass of the charged particle, and E the energy.

Thus, the transmission probability of interest can be estimated as the slashed area in Fig.2. This area in U is much smaller than that for the ordinary original potential V_0. In other word, the probability becomes much larger by the use of the weakened potential. Furthermore, the damping effect works at greater distance of r when R_c is large. Strictly speaking, the larger the value of R_c increases, the larger T increases. Therefore, the value of R_c is closely related to the transmission probability T.

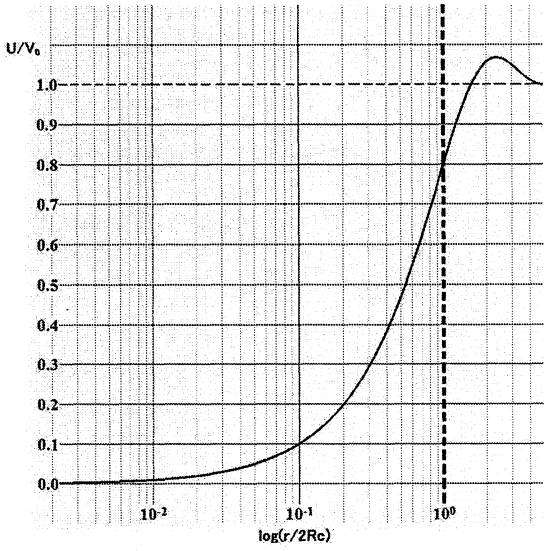

Fig.3. the ratio of U and V_0 rapidly decreases while the distance r reduces one order.

3. VALUES OF R_c IN VACUUM

R_c values for electron and proton are given respectively as follows[1, 7].

$$R_c = 1.9\times10^{-12}\ \text{cm} \quad \text{(Electron).} \quad (3)$$

$$R_c = 1.0\times10^{-15}\ \text{cm} \quad \text{(Proton).} \quad (4)$$

Especially, R_c of proton is much smaller than nuclear radius. These values are too small to yield some effect discussed in the previous section, because a incident particle reaches the nuclear surface before the distance between a incident particle and a nucleon is close to $2R_c$ and some effect due to R_c appears. Therefore, in vacuum, there is no effect of critical length R_c on transmission probability.

4. PHYSICAL QUANTITIES IN SEMICONDUCTOR

As seen in the previous section, the values of critical length R_c are too small to achieve some effect in vacuum. We then investigate the possibility that these critical lengths change in materials.

Recently, W.Zawadzki[4] considered the analogy between the band structure of narrow gap semiconductor and the Dirac equation for relativistic electron in vacuum. Dirac equation for free electron has four solutions: Two solutions with different spin component belong to positive energy region ($E_p > mc^2$), and the other two solutions belong to negative energy region ($E_p < -mc^2$) respectively in vacuum, where

$$E_p = \sqrt{m^2c^4 + p^2c^2} . \qquad (5)$$

p is momentum and c is light speed in vacuum. We can regard these two regions as band structure in vacuum. It makes us possible to compare the band structure of semiconductor with that in vacuum.

Zawadzki has reported a dispersion relation for InSb-type semiconductor,

$$E_p = \sqrt{\left(\frac{E_g}{2}\right)^2 + E_g \frac{p^2}{2m^*}}, \qquad (6)$$

taking the limit of large spin-orbit energy. Here E_g is the energy gap and m^* is the effective mass. The electron velocity v in the conduction band is given as the group velocity:

$$v_i = \frac{\partial E_p}{\partial p_i} . \qquad (7)$$

The maximum value of v taking the limit of large p becomes

$$\lim_{p\to\infty} v_i = \sqrt{\frac{E_g}{2m^*}} \equiv u . \qquad (8)$$

The maximum velocity u of electron in semiconductor plays the same role as light speed c in vacuum. We can rewrite Eq.(8) as $E_g = 2m^*u^2$. Using this equation, Eq.(6) is expressed as

$$E_p = \sqrt{m^{*2}u^4 + p^2u^2} . \qquad (9)$$

Equation (9) is the same as Eq.(5) in the form. Taking z axis along the momentum of the electron, Zawadzki reported the following Hamiltonian

$$H = u\alpha_z p_z + \beta m^* u^2 \qquad (10)$$

for the conduction and the light hole band, where α and β are the matrices in the Dirac Hamiltonian

$$H = c\boldsymbol{\alpha}\mathbf{p} + \beta mc^2 . \qquad (11)$$

Here, we note that Hamiltonian (10) has the same form as Eq.(11) perfectly, by replacing as

$$c \to u, \quad m \to m^* . \qquad (12)$$

According to Heisenberg's equation of motion

$$\frac{dO}{dt} = \frac{1}{i\hbar}[O, H], \qquad (13)$$

both Hamiltonians having the same form give the same equations of motion with the replacement of Eq.(12). Therefore, equations and physical quantities obtained in vacuum will be hold also in the semiconductor by replacement of Eq.(12).

For example, Zawadzki[4] has investigated Zitterbewegung (trembling motion) of the electron in semiconductor based on Hamiltonian of Eq.(10), and then obtained the amplitude of the trembling motion:

$$\lambda_z = \frac{\hbar}{m^* u}, \qquad (14)$$

Here λ_z corresponds to Compton wavelength. It is about 100 times larger than the corresponding amplitude for free electron in vacuum[10].

Next we consider another example concerned with the spin-magnetic moment of electron. Two of the present authors[5] found that the spin-magnetic moment of electron is caused by 'transition current' between positive energy state and negative energy state in vacuum;

$$< \mu_z >_{vac} = \frac{e\hbar c}{2E_p}. \qquad (15)$$

Here 'transition current' means the matrix element <n|J|m>, where |m> denotes positive energy state and |n> negative energy state. When momentum p is small, we have the well known result

$$< \mu_z >_{vac} = \frac{e\hbar}{2mc}, \qquad (16)$$

because of $E \cong mc^2$. Direct substitution of replacements of Eq.(12) into Eq.(16) gives

$$< \mu_z >= \frac{e\hbar}{2m^* u}. \qquad (17)$$

According to Zawadzki[4], we have $c/u \cong 100$ and $m/m^* = 10 \sim 100$. This means that $< \mu_z >$ of Eq.(17) is more 1000 times larger than $< \mu_z >_{vac}$ of Eq.(16) in vacuum[6]. Then spin-magnetic moment of the electron in semiconductor will include the contribution from Eq.(17) besides of Eq.(16), that is, Lande's g-factor in semiconductor becomes effectively larger than $g = 2$.

5. HOW ABOUT R_c FOR DEUTERON IN PALLADIUM?

In section 4, we presented that the value of physical quantities in vacuum change for semiconductor. This fact will be true also for other material in general. Critical length R_c is equal to the geometric mean value of 'classical electron radius' r_c and the Compton wavelength λ [7]:

$$R_c = \sqrt{r_c \lambda / 2}. \qquad (18)$$

It also depends on light speed c and electron mass m such as

$$R_c \sim \frac{1}{mc^{3/2}}. \qquad (19)$$

It is well known that both m and c in material can change, or be replaced by effective one[8][9]. Therefore, the change of R_c for deuteron is also strongly expected in palladium lattice, in contrast to vacuum. As pointed out in section 2, large value of R_c permits us to overcome the Coulomb barrier which prevents the nuclear reaction of deuteron.

In order to determine R_c, the most important thing for us is to know the solid-state property of palladium, and to know how the occluded deuterons behave in palladium.

References

[1] S. Sasabe: "Coulomb Potential Weakened by Self-Field of Electron", J. Phys. Soc. Jpn, **Vol.61**, 812 (1992).

[2] S. Sasabe: "Possibility of Control on Coulomb Potential", Proceedings of 7th Meeting of Japan CF Research Society, 47 (2006).

[3] M. Namiki, I. Ohba: *Scattering Theory in Quantum Mechanics*、 section 3, 1997, Iwanami (in Japanese).

[4] W. Zawadzki: "Zitterbewegung and its effects on electrons in semiconductors", Phys. Rev. **B72**, 085217 (2005).

[5] S. Sasabe, K. Tsuchiya: "What is spin-magnetic moment of electron?", Phys. Lett., **A372,** 381 (2007); DOI:10.1016/j.physleta.2007.07.078

[6] S. Sasabe, K, Tsuchiya: "Change of Spin-Magnetic Moment of Electron due to Band Structure", Trans. IEE. Japan, **Vol.127-A**, No.4 (2008) to be published.

[7] S. Sasabe: "Finite Mass Change of Electron in Alterd Self-Field Approach", J. Phys. Soc. Jpn, **Vol.59**, 449 (1990).

[8] J. Marangos: "Slow light in cool atoms", Nature, **Vol.397**, 559 (1999).

[9] C. Kittel: *Introduction to solid state physics*, section 8, 1986, Jon Wily & Sons.

[10] S. Sasabe; "Zitterbewegung of Dirac Electron from the Point of View of Huang's Expectation Value", Elec. Eng. Jpn. **Vol.132,** 1 (2000).

New Approach to the Theory of Cold Nuclear Transmutation

Mikio Fukuhara

Institute for Materials Research, Tohoku University

fukuhara@imr.tohoku.ac.jp

Abstract

The cold transmutation observed on the surfaces of Sr- or Cs-doped Pd/(CaO+ Pd)Pd complexes is interpreted to be a result of virtual ${}^{8}_{4}X$ or ${}^{12}_{6}X$ particle addition by the confinement of four or six interstitial solute deuterons, respectively, jumping from four tetragonal sites to octahedral sites along [111] directions in a Pd/CaO lattice and electrostatic attraction due to the charge transfer in the chains of atoms; *i.e.*, an alternating tetrahedral-octahedral site arrays with the aid of the electron-phonon charge-density wave coupling and electropionic attraction effects due to the capture of excited electrons from Pd and Ca by vacuum pumping:

$$^{88}_{38}\mathrm{Sr} + 8\,^{2}_{1}\mathrm{D} + 4\,e^{-} \rightarrow {}^{96}_{42}\mathrm{Mo} + 4\nu + 4\gamma$$

$$^{133}_{55}\mathrm{Cs} + 8\,^{2}_{1}\mathrm{D} + 4\,e^{-} \rightarrow {}^{141}_{59}\mathrm{Pr} + 4\nu + 4\gamma$$

$$^{137}_{56}\mathrm{Ba} + 12\,^{2}_{1}\mathrm{D} + 6e^{-} \rightarrow {}^{149}_{62}\mathrm{Sm} + 6\nu + 6\gamma$$

$$^{138}_{56}\mathrm{Ba} + 12\,^{2}_{1}\mathrm{D} + 6\,e^{-} \rightarrow {}^{150}_{62}\mathrm{Sm} + 6\nu + 6\gamma.$$

The deuterons are a source of supply for reparation for mass balance in the transmutation. The roles of CaO are dissolution of Sr and Cs and the creation of a good route for deuteron rushing by aid of vacuum pumping.

* E-mail address: fukuhara@imr.tohoku.ac.jp

1. Introduction

Recently, Iwamura and coworkers [2,3] have reported that nuclear transmutations are observed on the surfaces of Pd/(CaO+Pd)Pd (hereafter referred to as Pd/CaO) complexes, which consist of a thin Pd layer, alternating CaO and Pd layers, and bulk Pd, after subjecting the Pd complexes to D_2 gas permeation. When Cs, Sr, and Ba were added on the surfaces of the Pd complexes, Pr, Mo, and Sm emerged on the surfaces whereas the amount of Cs, Sr, and Ba decreased after

the Pd complexes were subjected to D2 gas penetration at 343 K and 1 atom for about one and two weeks. It was also noted that the increases in mass number are 8 and 12, and those in atomic number are 4 and 6 for the former and latter transmutations, respectively. This indicates the occurrence of cold (low-energy) nuclear transmutations from Cs to Pr, from Sr to Mo, and from Ba to Sm:

$$^{88}_{38}\mathrm{Sr} \rightarrow {}^{96}_{42}\mathrm{Mo} \qquad (1)$$

$$^{133}_{55}\mathrm{Cs} \rightarrow {}^{141}_{59}\mathrm{Pr} \qquad (2)$$

$$^{137}_{56}\mathrm{Ba} \rightarrow {}^{149}_{62}\mathrm{Sm} \qquad (3)$$

$$^{138}_{56}\mathrm{Ba} \rightarrow {}^{150}_{62}\mathrm{Sm}. \qquad (4)$$

Following the works of Iwamura and coworkers [2,3], Celani *et al.*[4] Kitamura *et al.*[5] and Yamada *et al.*[6] have confirmed the same results in different laboratories with different analytical methods. However, nobody has resolved any reasons for the transmutations yet. Furthermore, the role of Ca in the transmutations remains unknown.

Our interest lies in studying the dynamic interaction among deuterons in the Pd/ CaO lattice, assuming that the deuterons jump from the tetragonal sites to the octahedral sites to formation of a transient particle using the dynamics of an electron-phonon- coupled charged density wave (CDW) system. In this paper, a new interaction model is proposed on the basis of the collective resonance of electrons and the resulting photon emissions from Pd and Ca atoms. The central problem of this work is to explain how the deuterons react with each other when there exists a potential barrier so high that it should not be possible for the deuterons to draw sufficiently near to interact. For experimental confirmation, the question is raised as to whether the compressive forces exerted by the metal structure could lead to such a confinement of deuteron pairs at the necessary close proximity.[7,8] In addition, the compensation of mass balance in transmutations is an open question.

We have investigated the physical roles of electrons and electron neutrinos for electromagnetic and weak atomic interactions and have reported that the electrons and neutrinos in a nucleus enhance the fusion reaction as well as the catalytic effect of neutral pions.[9] A cold transmutation being similar to the cold fusion is currently a hot topic in low-energy cold fusion science, although few works have been reported on this subject.[2-5, 9-12]

2. Dynamic Interaction between He Nuclei and Formation of $^{8}_{4}\mathrm{X}$

We first focus our discussion on eqs. (1) and (2) for a transmutation mechanism. From the reactions (1) and (2), we note the common point that the increases in mass number and atomic number are 8 and 4, respectively. Although increase in atomic number for eqs. (1) and (2) can be attained by two time- double β decay of Sr and Ca elements[9], it is impossible to get the increase

in mass number. It is actually encouraging to consider a virtual ${}^{8}_{4}X$ particle for the processes. This is a transient particle that does not exist in nature. To elucidate both transmutation reactions, eqs. (1) and (2), we must consider the possible formation of the ${}^{8}_{4}X$ particle. In this case, it is necessary that the D, Pd and Ca elements are involved in the transmutations. If the ${}^{8}_{4}X$ particle exists, we can consider the following processes.

$$ {}^{88}_{38}Sr + {}^{8}_{4}X = {}^{96}_{42}Mo \qquad (5) $$

$$ {}^{133}_{55}Cs + {}^{8}_{4}X = {}^{141}_{59}Pr \qquad (6) $$

The ${}^{8}_{4}X$ is a four-*np* state whose isospin wave function is antisymmetric, where *n* and *p* are the neutron and proton, respectively. The first-order internuclear force among protons and neutrons in the ${}^{8}_{4}X$ nucleus must be mediated by eight charged pions, $\pi^{\pm}$, and eight neutral pions, π^{0}. On the other hand, the helium ${}^{4}_{2}He$ particle is composed of two protons and two neutrons. These four nucleons must be combined by the attractive mediation of two charged and two neutral pions. Thus, the ${}^{8}_{4}X$ can be formed by two helium nuclei,

$$ {}^{4}_{2}He + {}^{4}_{2}He = {}^{8}_{4}X. \qquad (7) $$

We have already reported a neutral-pion-catalyzed fusion based on the collective resonance (excitation) effect of electrons derived from Pd.[13)]

$$ {}^{2}_{1}D + {}^{2}_{1}D + 2\pi^{0} = {}^{4}_{2}He. \qquad (8) $$

From eqs. (5) and (6), we can obtain the following equation,

$$ 4\,{}^{2}_{1}D + 4\pi^{0} = {}^{8}_{4}X. \qquad (9) $$

If eq. (7) can occur from D_2 gas passing through the Pd/CaO complexes, we can replace the above-mentioned transmutations, eqs. (5) and (6), by

$$ {}^{88}_{38}Sr + 4\,{}^{2}_{1}D + 4\pi^{0} = {}^{96}_{42}Mo \qquad (10) $$

$$ {}^{133}_{55}Cs + 4\,{}^{2}_{1}D + 4\pi^{0} = {}^{141}_{59}Pr. \qquad (11) $$

Here, pions are responsible for all low-energy nuclear interactions;[14)] the pions within the nucleus allow the nucleonic species to bind together and transmute with each other.[10)]

On the other hand, an electron reacts with a deuteron to form a neutral pion and an electron neutrino: [15, 16)]

$$ e^{-} + {}^{2}D \rightarrow \pi^{o} + \nu + \gamma. \qquad (12) $$

Kenny [15)] has termed eq. (12) as the "electropionic reaction".

From eqs. (1),(2), (9) and (12), we obtain

$$ {}^{88}_{38}Sr + 8\,{}^{2}_{1}D + 4\,e^{-} \rightarrow {}^{96}_{42}Mo + 4\nu + 4\gamma \qquad (13) $$

$$ {}^{133}_{55}Cs + 8\,{}^{2}_{1}D + 4e^{-} \rightarrow {}^{141}_{59}Pr + 4\nu + 4\gamma \qquad (14) $$

with the aid of the electropionic attraction due to the capture of the electrons and deuterons. In eqs. (13) and (14), D is a source of supply for reparation for mass balance in a nuclear transmutation, and electrons are conduction electrons derived from the palladium, described later. Since eqs. (13) and (14) are nonequilibrium (irreversible) equations, they do not obey the rules of parity and momentum balance. On the other hand, in the irreversible endothermic reaction proposed by Glansdorff

and Prigogine [17], a marked enhancement is expected on the basis of the thermal factor of exp(-$\Delta G/kT$), where ΔG is the change in Gibbs energy for the entire system.

3. Roles of Pd, Ca and D for Transmutation

In the previous section, with a view to promoting transmutation process, the virtual ${}^{8}_{4}X$ or ${}^{12}_{6}X$ particle, formed by two or three helium nuclei, was proposed. Notwithstanding such a necessary condition, it is further necessary to get reasonable reasons. Next, we consider a sufficient condition for a dynamic reaction.

In previous papers,[18,19] the reason why nitrogen exists so abundantly in the Earth's atmosphere has been interpreted as a result of the endothermic nuclear transmutation of carbon and oxygen atom pairs in a carbonate (Ca,D) CO_3 lattice of mantle,

$$^{12}C + {}^{16}O + 2\,{}^{2}D \rightarrow 2\,{}^{14}N + {}^{4}He, \quad (15)$$

although the nuclear attraction effect due to the deuteron catalysis of nitrogen formation during the Archean era. In this case, the configuration and cross section of the D-inserted compound (Ca,D) CO_3 resemble those of the Pd/CaO complexes in this study. Hence, by analogy, we can image the atomic configuration of D-inserted Pd- and CaO -coupled lattices with faced-centered cubic (fcc) structures (Fig. 1). Furthermore, we have reported the electron and the neutrino in a nucleus enhance the fusion reaction[9] as well as the catalytic effect of neutral pions for formation of nitrogen in Eartth[19].

Since deuterium can be inserted in to the tetrahedral sites of the Pd and CaO lattices, the atoms

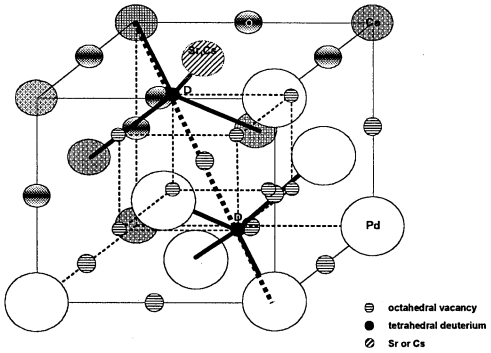

Fig.1 Sr-or Cs (small purple solid)-doped Pd/CaO complex crystal with tetrahedral D sites (small red solid) and octahedral vacancy sites (small blue solid) in Pd (large pink solid)/ Ca(middle light green solid)O(middle yellow solid) fcc lattice. The bold dot line indicates a chain (Ca-tetrahedral-site D- octahedral-site vacancy- tetrahedral-site D-Pd) along a <111> direction.

along four [111] directions are lined up in chains as follows: Ca-tetrahedral-site D-octahedral-site vacancy-tetrahedral-site D-Pd. The interstitial deuterons in PdDx and CaO are immersed in a sea of conduction electrons derived from the palladium and calcium atoms. Since the oxide CaO of Ca has an fcc lattice similar to that of Pd, it is suitable for the permutation of D_2 gases. Indeed, the bond lengths of Ca-D in CaO and Pd-D in Pd $D_{0.63}$ are 0.2080 and 0.1755 nm,[20] respectively, with a mismatch within $\pm$16 %. Thus the usage of the CaO layer promotes deuteron rushing by help of vacuum pumping. The actual passing route of deuterons is along four <111> directions in Fig. 1.

Next, we consider the cause of the local transition of deuterons in views of chemical potential effects in the Pd/ CaO complexes. Here, we note that coherency stress arises in the fluctuations of defects when atomic defects in crystals expand or contract the crystal lattice[21] because the elastic interaction

between the defects is mediated by the strain fields of the defects. The coherency stress and long-ranged elastic interaction are characteristic of a solid state with the defects. Indeed, the potential minimum for a hydrogen atom located at the tetrahedral interstice of a base-centered-cubic (bcc) β-$VH_{0.5}$ crystal is markedly displaced toward the crystal position of the octahedral interstice when the c axis, more precisely the [112] direction c-axis, is uniformly elongated by an external force at a constant volume. [22] Because the atomic configuration of the {001} plane of bcc-β-$VH_{0.5}$ surrounded by four tetrahedral interstitials is similar to that of the {110} plane of the fcc PdD crystal, the coherency stresses along the [111] directions of substochiometric PdDx could arise in the fluctuations of the defects. Hence, by analogy, we infer that the forced vacuum pumping in the fcc Pd/CaO complex [2,3] causes coherency stress and the resulting large slope of chemical potentials for the deuterons, leading to deuteron rushing along the [111] directions. Thus, the local transition of the tetragonal deuterons by vacuum pumping would aid the transition. This is a necessary condition for the dynamic interaction of interest.

4. Possible Collective Resonance and Three-Dimensional CDW

As an interaction mode for the Pd-Ca-D system, we note that the breathing-mode displacement of the oxygen atoms in the perovskite solid solution $BaPb_{1-x}Bi_xO_3$ causes the alternating expansion and contraction of the oxygen octahedral around the nonequilivalent Bi(I) and Bi(II) atoms [23] and leads to a complete charge disproportion [charge-density wave (CDW) instability] state, *i.e.*, an alternating Bi^{3+}-Bi^{5+} array. [24] In this case, the Fermi surface nests perfectly and the situation is favorable for the formation of a CDW. The CDW doubles the unit cell and creates a gap near the Fermi level. Because the deuteron atoms exist as itinerant deuterons in the Pd/CaO complex lattice, we expect a similar situation to occur for the Pd/CaO complexes.

As described in the previous section, the interstitial deuterons in the Pd and CaO lattices are surrounded tetrahedrally by four Pd atoms and four Ca atoms in a sea of conduction electrons. The CDWs are formed mostly in such materials, in which the atoms are lined up in chains (*i.e.*, an alternating tetrahedral $D^{+\delta}$-$Pd^{10-\delta}$ and $D^{+\delta}$-$Ca^{10-\delta}$ array [25]), the following breathing-mode-like displacement of the deuterons occurs along the [111] directions.

The longitudinal deformation ξ(z) of the phase φ(z) of the $2k_F$ CDW along the chain directions induces the large redistribution $\xi u(z)$ with the wavelength $2\pi/\xi q$ and long-ranged Coulomb forces, giving an optical frequency ($\omega^2 \neq 0$) at a longitudinal phason, which is a type of collective mode, *i.e.*, an exciting state:

$$u(z) = \sqrt{\frac{2}{\omega_{2k_F}}} \frac{\Delta}{g} \cos(2k_F z + \phi(z)) \qquad (16)$$

$$\xi u(z) = \frac{1}{\pi}\frac{\partial \varphi}{\partial z} \qquad (17)$$

where g is the electron-phonon coupling constant, k_F the wave vector of the Fermi level, ω_{2k_F} the phonon energy for the lattice of the wavenumber $2k_F$, and 2Δ energy gap at the Fermi level. Thus, the tetrahedral-site deuterons are positively charged, and the octahedral-site vacancy is oppositely negatively induced. [26]

When the further enrichment of deuterium leads to octahedral site occupancy by vacuum pumping, the positively charged tetrahedral-site deuterons plunge into the negatively charged octahedral-site vacancy owing to the electrostatic force in addition to the Coulomb force (A-type in Fig. 3). This leads to the confinement of deuteron pairs or the formation of deuteron clusters stuck with electrons at the necessary close proximity. Furthermore, when four tetrahedral-site deuterons simultaneously rush into the octahedral site along the [111] directions, the $^{8}_{4}X$ nucleus would be formed as the fusion product, *i.e.*, the activated state product. Since the product is the transient particle of a shape isomer in the nucleus, it fuses with $^{88}_{38}Sr$ or $^{133}_{55}Cs$ occupying the Ca sites in the CaO lattice (Fig.1) in a moment, leading to the transmutation of interest. Another role of CaO is the dissolution of Sr and Cs. The jumping location of these interstitial solute deuterons is necessary for the transmutation. Because the CDW wavelength changes with

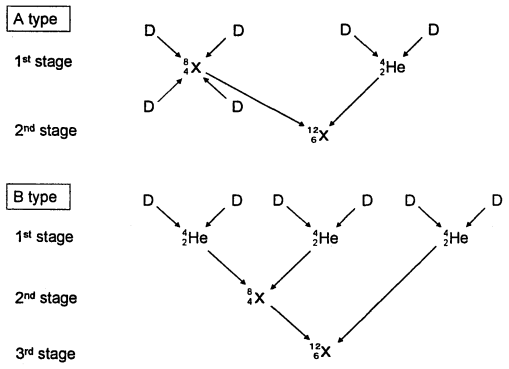

Fig.2 Transient transmutations (A- and B-types) of deuterons along [111] directions in Pd/CaO lattice.

the number of electrons, many electrons make the wavelength smaller, *i.e.*, the confinement stronger. It is known that the total oscillator strength in the collective resonance is approximately equal to the total number of oscillating electrons; [27] it is ~10 for the 4*d* resonance in Pd and ~10 for the 3*s*, 3*p*, and 4*s* electrons in Ca. The collective effect is strong only at energies above the first ionization threshold. The peak of the collective resonance is approximately at a frequency at which the atomic dielectric function $\varepsilon(k,\omega)$ with nonzero ω is zero. [28] Thus, the considerable confinement of two deuteron pairs could be attained by electrostatic attraction due to the collective resonance of many electrons.

5. Dynamic Interaction between He Nuclei and the Formation of $^{12}_{6}X$

Lastly, we consider the other type's transmutations in eqs. (3) and (4). If the transmutations for eqs. (3) and (4) can be formed by another virtual $^{12}_{6}X$ particle, we

can obtain the following formulae, as well as the above-mentioned procedure:

$$^{137}_{56}\mathrm{Ba}+12\,^{2}_{1}\mathrm{D}+6e^{-}\rightarrow\,^{149}_{62}\mathrm{Sm}+6\nu+6\gamma \quad (18)$$

$$^{138}_{56}\mathrm{Ba}+12\,^{2}_{1}\mathrm{D}+6e^{-}\rightarrow\,^{150}_{62}\mathrm{Sm}+6\nu+6\gamma \quad (19)$$

Thus, we can image the reaction processes along [111] directions in a large slope of deuteron potentials by vacuum pumping. This is a scheme of type B in Fig. 2.

6. Conclusions

The nuclear transmutation $^{88}_{38}\mathrm{Sr}\rightarrow\,^{96}_{42}\mathrm{Mo}$, $^{133}_{55}\mathrm{Cs}\rightarrow\,^{141}_{59}\mathrm{Pr}$, $^{137}_{56}\mathrm{Ba}\rightarrow\,^{149}_{62}\mathrm{Sm}$ and $^{138}_{56}\mathrm{Ba}\rightarrow\,^{150}_{62}\mathrm{Sm}$ in the Pd/CaO complexes reported by Iwamura and coworker was interpreted as a result of the virtual $^{8}_{4}\mathrm{X}$ particle or $^{12}_{6}\mathrm{X}$ additions due to the confinement of four or six deuterons at necessary close proximity, respectively. The necessary condition for the transmutation is the jumping location transition of four interstitial solute deuterons from tetrahedral sites to octahedral sites along [111] directions, which arises from the large slope of deuteron chemical potentials. A sufficient condition can be attained by electrostatic attraction among the deuterons due to the charge transfer in the chains of atoms (*i.e.*, an alternating tetrahedral-octahedral site array) with the aid of the electron-phonon CDW coupling based on the collective resonance of many oscillating electrons derived from Pd and Ca:

$$^{88}_{38}\mathrm{Sr}+8\,^{2}_{1}\mathrm{D}+4\,e^{-}\rightarrow\,^{96}_{42}\mathrm{Mo}+4\nu+4\gamma$$

$$^{133}_{55}\mathrm{Cs}+8\,^{2}_{1}\mathrm{D}+4\,e^{-}\rightarrow\,^{141}_{59}\mathrm{Pr}+4\nu+4\gamma$$

The deuterons are a source of supply for reparation for mass balance in the transmutation. In the irreversible endothermic reaction, the marked enhancement is expected. The roles of CaO are the dissolution of Sr and Cs in Pd/CaO lattice, and the creation of a good route for deuteron rushing. In the case of the transmutations of $^{149}_{62}\mathrm{Sm}$ and $^{150}_{62}\mathrm{Sm}$, the following reactions can be proposed:

$$^{137}_{56}\mathrm{Ba}+12\,^{2}_{1}\mathrm{D}+6e^{-}\rightarrow\,^{149}_{62}\mathrm{Sm}+6\nu+6\gamma$$

$$^{138}_{56}\mathrm{Ba}+12\,^{2}_{1}\mathrm{D}+6\,e^{-}\rightarrow\,^{150}_{62}\mathrm{Sm}+6\nu+6\gamma.$$

References

1) M.Fukuhara, Jpn. J. Appl. Phys. **46, 5A** (2007) 3035.
2) Y. Iwamura, M. Sakano, and T. Itoh, Jpn. J. Appl. Phys. **41** (2002) 4642.
3) Y. Iwamura, T. Itoh, M. Sakano, N. Yamazaki, S. Kuribayashi, Y. Terada, T. Ishikawa, and J. Kasagi: *Condensed Matter Nuclear Science*, J. P. Biberian, Ed. (World Scientific Publishing, Singapore, 2004), pp. 339-358.
4) F.Celani, *et al.*, Proc.4th Meeting of Jpn CF Res.Soc., Iwate University, Japan, pp.17-21.
5) A. Kitamura, R. Nishio, H. Iwai, R. Satoh,

A. Taniike, and Y. Furuyama, *Condensed Matter Nuclear Science*, A. Takahashi, K. Ota, and Y. Iwamura Eds. (World Scientific Publishing, Singapore, 2006), pp.272-277.

6) H.Yamada, S.Narita, S.Taniguchi, T.Ushirozawa, S.Kurihara, M.Higashizawa, H.Sawada and M.Itagaki, Proc.7th Meet. Japan Cold Fusion Research Society, Tokyo, 2006, p. 28.
7) M. Gai, S. L. Rugari, R. H. France, B. J. Lund, Z. Zhao, A. J. Davenport, H. S. Isaacs, and K. G. Lynn, Nature **340** (1989) 29.
8) D. E. Williams, D. J. S. Findlay, D. H. Craston, M. R. Sené, M. Bailey, S. Croft, B. W. Hooton, C. P. Jones, A. R. J. Kucernak, J. A. Mason, and R. I. Taylor, Nature **340** (1989) 375.
9) M.Fukuhara, Proc.6th Meet. Japan Cold Fusion Research Society, Tokyo, 2005, pp. 53-57.
10) S. E Jones, E. P. Palmer, J. B. Czirr, D. L. Decker, J. M, Thorne, S. F. Taylor, and J. Rafelsli, Nature **338** (1989) 737.
11) T. Mizuno, T. Ohmori and M. Enyo, Electrochem. **64** (1996) 1160.
12) F. Celani, *et al.*: *Condensed Matter Nuclear Science*, J. P. Biberian, Ed. (World Scientific Publishing, Singapore, 2004), pp. 108-127.
13) M. Fukuhara, Fusion Sci.Tech. **43** (2003) 128.
14) D. F. Measday, and G. A. Miller, Annu. Rev. Nucl. Part. Phys. **29** (1979)121.
15) J. P. Kenny, Fusion Technol. **19** (1991) 547.
16) M. Fukuhara, Fusion Technol. **34** (1998) 151.
17) P. Glansdorff and I. Prigogine, *Thermodynamic Theory of Structure, Stability and Fluctuations* (Wiley-Interscience, London, 1971).
18) M. Fukuhara, Nuovo Cimento **27** (2004) 99.
19) M.Fukuhara, Proc.7th Meet. Japan Cold Fusion Research Society, Kagoshima, 2006, pp. 71-73.
20) J. M.Rowe, J. J. Rush and H. G. Smith, H. G. Smith, M. Mostoller, and H. E. Flotow, Phys.Rev.Lett. **33** (1974) 1207.
21) H. Wipf, J. Volkl and G. Alefeld, Z.Phys.B, **76** (1989) 353.
22) H. Sugimoto, J. Phys. Soc. Jpn. **59** (1984) 2529.
23) S. Uchida, K. Kitazawa and S. Tanaka, Phase Transitions **8** (1987) 95.
24) L. F. Mattheiss and D. R. Hamman, Phys.Rev., **B28** (1983) 427.
25) S. Brown and G. Grüner, Sci.Am. **4** (1994) 28.
26) R. A. Swalin: *Thermodynamics of Solids* (John Wiley & Sons, New York, 1962) p. 275.
27) G. Mukhopdhyay and S. Lundqvist, J.Phys.,B, **12** (1979) 121297.
28) M. Fukuhara, Phys.Status Solidi **B, 175** (1993) 421.

An Explanation of Nuclear Transmutation in XLPE (Crosslinked Polyethylene) Films with and without Water Trees

Hideo Kozima,
Cold Fusion Research Laboratory,
421-1202, Yatsu, Aoi, Shizuoka 421-1202, Japan

Abstract

An explanation of the nuclear transmutation (NT) observed in the XLPE (crosslinked polyethylene) films dipped in aqueous electrolytic solutions with and without application of high-frequency electric field was presented by the neutron-drop model used in the theoretical investigation of the cold fusion phenomenon in transition-metal hydrides/deuterides (CF materials). The NT's K → Ca, Mg → Al, $^{56}_{26}$Fe → $^{57}_{26}$Fe and Fe → Ni are explained by a single neutron absorption with or without a succeeding beta-decay to get final nuclides. The NT's $^{56}_{26}$Fe → $^{64}_{30}$Zn and $^{56}_{26}$Fe → $^{60}_{28}$Ni are explained by an absorption of a neutron drop $^{8}_{4}\Delta$ and $^{4}_{2}\Delta$, respectively, in the cf-matter that was supposed to be formed at boundary regions of crystallites in the sample. Production of wonderful elements Li, Pb and Bi is discussed from our point of view.

1. Introduction

We have tried to explain the wide-spread experimental facts in the cold fusion phenomenon (CFP) from a unified point of view using a phenomenological models (the trapped neutron catalyzed fusion model (TNCF model) at first and then the neutron-drop model (ND model), a generalized version of the former). It should be remembered here that the development of the model was demanded to explain NT's with large changes of the nucleon and proton numbers observed in the CFP.

In the process of verification of the basic premises of these successful models, we have developed a quantal investigation of the CF materials such as transition metal hydrides/deuterides composed of lattice nuclei of transition metals and interstitial protons/deuterons. It was shown that it is possible to appear the cf-matter composed of neutron drops $^{A}_{Z}\Delta$ with Z protons, Z electrons and $(A-Z)$ neutrons in a dense neutron liquid at boundary /surface regions of the crystals.

Recently, Kumazawa et al. [1] observed the nuclear transmutation (NT) in XLPE (crosslinked polyethylene) including water trees and then detected weak emission of gamma or X-rays from similar samples [2]. Generally speaking, water trees are formed macroscopically at (α) boundaries of XLPE samples and microscopically at (β) amorphous portions of the sample among spherulites composed of crystalline lamellae.

The NT observed in the XLPE films by

Kumazawa et al.[1, 2] has common characteristics to that observed in CF materials as a part of the CFP. Therefore, it is natural to apply the same model to explain the NT in XLPE that was successful to explain the NT in the CF materials [3].

Experimental results in XLPE have clearly shown that the NT have occurred when the samples (**Original**) were dipped in the electrolytic solutions (**Blank**) and also when high-frequency (2.4–3.0 kHz), high-voltage (3.0–4.0 kV/mm) electric voltage was applied further (let us call such samples **Experimental** in the following discussion, for simplicity) as shown in Table 6 of [1]. As electrolytes, (a) **KCL**, (b) **NaCl** and (c) **$AgNO_3$** were used for aqueous electrolytic solutions as shown in this Table. It is noticed that the NT's were observed not only in the region where were observed water-trees but also in the region where were not (cf. Dipped in $AgNO_3$ solution in Table 6 [1]) even if this is not always a precise distinction because it was done visually, as the authors commented in their original paper.

Increase (+) and decrease (-) of elements in samples (Experimental) were qualitatively depicted in Table 9 of [1] for electrolytes KCl, NaCl and $AgNO_3$.

In this paper, we give an explanation of the mechanism to produce the observed nuclei in both of XLPE samples, Blank and Experimental, based on the neutron-drop (ND) model proposed by the author [3].

2. Theoretical Basis of the Data Analysis

The XLPE (crosslinked polyethylene) used in the experiment [1,2] was made from low density polyethylene (LDPE) adding an organic crosslinking agent and heating. XLPE contains cross-link bonds which changing it into the polymer structure, changing the thermoplastic into a duromer. In general, a LDPE is composed of two components; the crystalline and the amorphous portions. The crystallinities of the LDPE and the XLPE are about 50 and 45%, respectively, at room temperature. The crystalline portion is composed of the spherulites containing radially distributed lamellae, stacks of folded polyethylene chains with a thickness of about 100 angstroms.

Thus, a XLPE sample in a good condition is supposed to include a lattice structure (lamella) with ordered carbon nuclei (lattice nuclei) interlaced with ordered protons. In the structure of lattice nuclei and interstitial protons, there appears the super-nuclear interaction between neutrons in lattice nuclei mediated by interstitial protons as shown in our previous works [3]. The super-nuclear interaction between neutrons in lattice nuclei results in the neutron band in which neutron Bloch waves propagate in the crystal lattice without disturbance unless there are such disorders of the arrangement as impurities and boundaries.

In the boundary region of the crystal lattice where the neutron Bloch waves are reflected, there occurs accumulation of the waves and a state with a high-density neutron appears. In this state, there is a cf-matter composed of neutron drops ${}^{A}_{Z}\Delta$ immersed in a dense neutron liquid.

In the region where are disorders of the

arrangement of nuclei, the neutron Bloch wave and therefore the neutron drops interact with these irregular nuclides and results in nuclear reactions generating new nuclides together with liberated excess energy. In these nuclear reactions in the cf-matter, a characteristic mechanism works where the liberated energy is directly accepted by the cf-matter and converted into lattice energy instead of emission of a gamma photon as in a nuclear reaction in free space. This is the essential scenario of the neutron-drop (ND) model for the CFP proposed by us [3].

The nuclear reactions in solids thus induced are characterized by several properties; (1) liberated energy in the nuclear reactions are transferred to the crystal lattice not emitted as gamma rays, (2) the threshold energy for nuclear reactions in free space becomes zero or very low, (3) the threshold energy for fission also becomes zero or very low. The weak radiation observed by Kumazawa et al. [2] may be considered as a proof of the occurrence of nuclear reactions in the system but is a peripheral effect accompanied to the main nuclear reactions that trigger birth of water trees in the samples.

3. Characteristics of the Experimental Result and its Explanation by the ND Model

We give an explanation of characteristics of the experimental data obtained by Kumazawa et al. [1] using the ND model.

3-1 Experimental Results

Essential parts of the extensive experimental data sets on the NT in the XLPE obtained by Kumazawa et al. [1] are given in their Tables 6 and 9.

In the experiments, a XLPE (cross-linked polyethylene) sheet 0.5 mm thick was used. The original sheet (Original sample) was scratched by an Au wire brush on the surface to create the water needle electrodes where the water trees starts. Au was deposited as a ground electrode onto the bottom surface of the sample. Then, the sample was dipped in aqueous solutions of electrolytes (a) KCl, (b) NaCl and (c) $AgNO_3$ to make the Blank samples. To the Blank samples in the aqueous solutions, electric fields with high-frequency (2.4–3.0 kHz) and high-voltage (3.0 – 4.0 kV/mm) were applied between the voltage application wire above the sample and the ground electrode for 140 – 320 hours to obtain "the samples after voltage application" (let us call them the Experimental samples, for simplicity). Quantitative analysis of elements were performed for (I) the **Original**, (II) the **Blank** and (III) the **Experimental** samples for three electrolytes (a) **KCl**, (b) **NaCl** and (c) **$AgNO_3$**. In the case (c), there are no data on the blank samples but data on the two distinct regions selected visually (i) **with water trees** and (ii) **without water trees**.

Whole experimental data was tabulated in Table 6 [1] and a part of typical data is qualitatively shown in Table 9 of [1] where are shown the increase (+) and decrease (–) of elements in the Experimental compared to the Original samples.

Characteristics in the changes of elements from (I) the Original to (II) the Blank and (III) the Experimental samples were summarized as follows;

In the case (a) (KCl),

(1) K decreased and Ca increased,

(2) ^{56}Fe decreased and ^{57}Fe increased,

(3) ^{64}Zn increased while other isotopes of Zn decreased.

In the case (b) (NaCl),

(4) Mg decreased and Al increased in which the gross weight of the two elements was hardly different compared to the Blank or the Original samples.

In the case (c) ($AgNO_3$),

(5) Fe decreased and Ni increased,

(6) New elements Li, Na, Pb and Bi were detected, and

(7) There are changes of elements in both regions with and without water trees.

Furthermore, there are interesting features of the blank samples (II) in the case (a).

(8) In Blank samples, Mg and Ca are increased from those in the Original one while Fe is decreased.

In the second paper [2] by Kumazawa et al., they reported detection of weak and burst-like radiation supposed to be low energy gamma or X-ray. In the CFP, there are a few observations of gamma and X-rays but are peripheral (cf. Section 6.3 of [4] for the data of gamma ray observation). We concentrate our investigation in this paper to the data reported in the first paper [1].

3-2 Theoretical Investigation

As discussed in Section 2, the crystalline portion of the XLPE sample has a similar physical properties to the transition-metal hydrides/deuterides where observed various events in the CFP. As we summarized at the end of the previous sub-section, there are several NT in the XLPE films that have corresponding ones in the CFP explained phenomenologically [3].

We give explanations of the seven characteristics of the nuclear transmutations (NT) in XLPE giving counterparts in the CFP for reference.

(1) Decrease of K and increase of Ca in the case (a) are explained by such a reaction in the solids by absorption of a neutron followed by beta decay with a liberated energy $\Delta E = 1.31$ MeV;

$$n + {}^{39}_{19}\mathrm{K} \rightarrow {}^{40}_{19}\mathrm{K}^{*}$$

$$\rightarrow {}^{40}_{20}\mathrm{Ca} + e^{-} + \underline{\nu}_{e}\ (\sigma_{nK39} = 2.10\ \mathrm{b}) \quad (3\text{-}1)$$

where $\underline{\nu}_e$ is an electron neutrino. As a measure of the reaction cross-section in solids we cited the value in free space in the parenthesis behind the equation. the Corresponding examples of this type of NT in the CFP is given in Section 2.5.1 of [3].

(2) Decrease of $^{56}_{26}$Fe and increase of $^{57}_{26}$Fe in the case (a) are similarly explained but without beta decay due to the stability of $^{57}_{26}$Fe with an energy Q = 1.15 keV transferred to the lattice system instead of gamma ray emission in free space;

$$n + {}^{56}_{26}\mathrm{Fe} \rightarrow {}^{57}_{26}\mathrm{Fe} + Q.\ (\sigma_{nFe56} = 2.81\ \mathrm{b}) \quad (3\text{-}2)$$

(3) Increase of $^{64}_{30}$Zn and decrease of $^{66}_{30}$Zn, $^{67}_{30}$Zn and $^{68}_{30}$Zn in the case (a) are explained by using the neutron drop $^{A}_{Z}\Delta$, for example;

$$^{56}_{26}\mathrm{Fe} + {}^{8}_{4}\Delta \rightarrow {}^{64}_{30}\mathrm{Zn}. \quad (3\text{-}3)$$

Many examples of this type in the CFP are given in Section 2.5.2 of [3]. Decrease of other isotopes may be explained by nuclear reactions to transform them into other elements but its details are left for another work.

(4) Increase of Al and decrease of Mg in the case

(b) are explained by reactions similar to (3-2) with Q = 7.08 MeV and Q' = 12.11 MeV and a reaction similar to (3-1) with ΔE = 2.61 MeV.

$n + {}^{24}_{12}\mathrm{Mg} \rightarrow {}^{25}_{12}\mathrm{Mg} + Q$. ($\sigma_{\mathrm{nMg24}} = 0.05$ b)

$n + {}^{25}_{12}\mathrm{Mg} \rightarrow {}^{26}_{12}\mathrm{Mg} + Q'$. ($\sigma_{\mathrm{nMg25}} = 0.19$ b)

$n + {}^{26}_{12}\mathrm{Mg} \rightarrow {}^{27}_{12}\mathrm{Mg}^{*}$

$\rightarrow {}^{27}_{13}\mathrm{Al} + e^{-} + \underline{\nu}_{e}$. ($\sigma_{\mathrm{nMg26}} = 0.04$ b)

(5) Decrease of Fe and increase of Ni in the case (c) are explained similarly with use of the neutron drop, for example;

${}^{56}_{26}\mathrm{Fe} + {}^{4}_{2}\Delta \rightarrow {}^{60}_{28}\mathrm{Ni}$.

(6) New elements with nucleon and proton numbers far from those of elements preexisted in the system were observed fairly often in the CFP. There are several types of events producing such nuclides with largely shifted nucleon and proton numbers, A and Z, from those of original nuclides; One of them similar to the case Li, Na, Pb and Bi may be the NT by transformation discussed in Section 2.5.4 of [3]. (There are observations of C from Pd and W systems, Cl from a Pd system, Fe in a carbon system, and Pb in a Pd system.)

(7) The occurrence of the NT in both of regions with and without water trees (by visual observation) might be evidence that the NT is not a result but a cause of the water tree generation. If seeds of water trees were born at boundaries or impurities in the disordered regions of the XLPE sample, as is said conventionally, the position is just where the cf-matter is tend to be formed by accumulation of neutrons in the neutron band. The larger the lamella in the spherulite, the easier the cf-matter formed and the easier nuclear reactions occur there.

Thus, we may imagine a following scenario of growth of a water tree; (i) a NT of impurity nuclides occurs at a boundary region heating there by a liberated energy, (ii) a seed of a water tree is induced by the liberated energy, and (iii) the applied high-frequency electric field makes the water tree grow.

(8) The changes of amounts of elements in the blank samples from those in the Original in (a) support this scenario.

Furthermore, the characteristics (α) and (β) of water-tree formation pointed out in Introduction are consistent with the scenario. The lamella has a crystalline structure with lattice nuclei (C) and interstitial protons favorable for formation of the neutron band and the cf-matter [3]. By our scenario, nuclear reactions between a neutron or a neutron drop ${}^{A}_{Z}\Delta$ and exotic nuclei (e.g. ${}^{39}_{19}\mathrm{K}$) can take place.

4. Discussion

If the above explanation of the various experimental data obtained in XLPE samples consistent with that of data sets in the CFP is trustworthy, we can deduce a prediction for effective occurrence of NT in CF materials in general. Formation of the neutron band is easier in crystals with the more perfect periodicity of lattice nuclei (C) and interstitial hydrogen isotopes (H), i.e. higher crystallinity (lamellae and spherulite formation) in XLPE is favorable for formation of the neutron band. This factor may correspond to the higher average value of the D/Pd ratio in palladium deuterides that is necessary to be more than a minimum value at around 0.85 to realize the CFP in them (cf. Section 2.9.2 of [3]). In the case of XLPE,

regularity of proton array in a lamella is secured and remaining factor is the crystallinity of the sample which may depend on how the sample is manufactured. There may be a minimum size of lamellae in spherulites to realize the neutron band and therefore the NT in XLPE.

To realize nuclear reactions resulting in the generation of new nuclides, it is necessary to have appropriate irregularities of the lattice (boundaries and impurities) and appropriate nuclides in addition to the regularity of the nuclear arrangement for the neutron band formation,. The imbalance of samples A1, A2, B1 and B2 shown in Table 6 [1] may be explained by the inhomogeneous distribution of regular portions with spherulites and also density of such impurities as electrolyte ions.

In this paper, it was explained that the NT well known in the CFP occur also in the XLPE samples. Characteristics of the phenomenon in both of systems, transition- metal hydrides/deuterides and XLPE films, are very similar despite of the difference in the lattice nuclei and hydrogen isotopes: lattice nucleus is the transition metal (Ti, Ni, Pd) in the former and is carbon (C) in the latter; hydrogen isotope is proton or/and deuteron in the former and is proton in the latter. This shows that the mechanism responsible to the NT in both systems is independent of the species of lattice nuclei (Pd, Ni, Ti or C) and also of the species of hydrogen isotopes (proton or deuteron), if it is natural to assume a common cause for them.

Another remarkable point proved by the extensive data by Kumazawa et al. [1,2] is that the water tree in XLPE is, at least partially, induced by the NT in the sample. Effects of the high-frequency electric field (HFEF) may be multiple; (1) HFEF make the electrolyte ions diffuse into the sample (especially at amorphous portions) to become irregular ions. When a NT occurs at an irregular ion nucleus, the liberated energy induces a seed of water trees. (2) HFEF then accelerates growth of the water trees into a larger scale.

The fact that silver (Ag) has larger effect in water-tree formation, the tree in this case has a special name "the silver tree," may be a result of the large cross section of n – Ag reaction (38.62 and 90.53 b for ^{107}Ag (51.82%) and ^{109}Ag (48.18%), respectively) compared to small values of 0.53 and 2.1 b for n – ^{23}Na and n – ^{39}K reactions, respectively (1 b = 10^{-24} cm^2).

Based on the above mentioned scenario of the NT in XLPE, we may give speculation about possible nuclear reactions in it.

First, the silver isotope has a large cross section for a neutron absorption followed by a beta decay as mentioned above;

$$n + {}^{107}_{47}\mathrm{Ag} \rightarrow {}^{108}_{47}\mathrm{Ag}^{*}$$

$$\rightarrow {}^{108}_{48}\mathrm{Cd} + e^{-} + \underline{\nu}_{e}, \quad (\sigma_{\mathrm{nAg107}} = 38.62 \text{ b})$$

$$n + {}^{109}_{47}\mathrm{Ag} \rightarrow {}^{110}_{47}\mathrm{Ag}^{*}$$

$$\rightarrow {}^{110}_{48}\mathrm{Cd} + e^{-} + \underline{\nu}_{e}, \quad (\sigma_{\mathrm{nAg109}} = 90.53 \text{ b})$$

with liberation energies ΔE of 1.65 and 2.89 MeV, respectively. We can expect generation of cadmium if there occur these reactions with single neutron participation in the sample.

Second, proton has a cross section of about 0.332 b for thermal neutron absorption;

$$n + p \rightarrow d + Q, \quad (\sigma_{\mathrm{np}} = 0.332 \text{ b})$$

with Q = 2.22 MeV thermalized in the sample as we assume in our model. We can expect

enrichment of deuterium in the sample if the $n-p$ reactions effectively occur in amorphous portion surrounding spherulites in XLPE. This reaction may play an important role in formation of seeds of water trees if the deuterium enrichment is confirmed in clean XLPE samples without addition of exotic ions.

The complicated phenomenon of water trees in XLPE films will give further interesting examples of the CFP thoroughly investigated in transition- metal hydrides and deuterides.

Acknowledgement

The author would like to express his thanks to Dr. Hiroshi Yamada of Iwate University and Dr. Takao Kumazawa of Chubu Electric Power Co. for their valuable discussions on the work by Kumazawa et al. [1, 2]

References

1. T. Kumazawa, W. Nakagawa and H. Tsurumaru, "A Study on Behavior of Inorganic Impurities in Water Tree" *Electrical Engineering in Japan* **153**, 1 – 13 (2005).

2. T. Kumazawa and R. Taniguchi, "Detection of Weak Radiation Involving Generation and Progress of Water Tree" (in Japanese) *IEEJ Trans. FM,* **127**, 89 – 96 (2007)

3. H. Kozima, *The Science of the Cold Fusion Phenomenon,* Elsevier, 2006. ISBN-10: 0-08-045110-1.

4. H. Kozima, *Discovery of the Cold Fusion Phenomenon,* Ohtake Shuppan, Tokyo, 1998. ISBN: 4-87186-044-2.

A Chronicle of Condensed Cluster Fusion Models

Akito Takahashi*

*Osaka University (Prof. Emeritus); akito@sutv.zaq.ne.jp

Abstract: We have studied the theoretical models of deuteron-cluster fusion in dynamic process under the ordering/constraint conditions in regular metal-deuterium systems, for 18 years since 1989. This paper reviews a chronicle of our research papers in 1989－2007 in three steps. The step one is the study of multi-body deuteron fusion models in 1989-1999. The second step is the study of tetrahedral symmetric condensate (TSC) based on the electronic quasi-particle expansion theory (EQPET) in 2000-2005. The third step is the recent study of deuteron cluster dynamics and fusion rate by Langevin equation.

1. Step-1 Multi-Body Deuteron Fusion Models

The notorious announcement of Fleischmann-Pons test tube "cold fusion" claim[6] with large excess heat evolution without correspondingly intense neutron emission from the heavy-water electrolysis with Pd cathode in March 1989 inspired the author to get an idea and he submitted a short note[7] proposing that the three body deuteron interaction, 3D fusion, by the following D-catalyzed cascade reaction channel to produce main ash of helium-4 as given by Eq.(1).

We know that the ordinary d+d (2D) fusion should have two main outgoing channels with 50 %/50% branching ratio, the n + ^{3}He + 3.27 MeV channel and the p + t + 4.03 MeV channel, and have very small branch (10^{-5} %) of the electromagnetic transition, ^{4}He(g.s.)+ γ + 23.8MeV, in low deuteron kinetic energy. So, the author thought that *the third hadron interaction should participate into the d+d strong interaction to realize a main branch of ^{4}He producing reaction.* The author is still keeping this original view until now (in 2007[8]) for theorizing the deuteron cluster fusion models in dynamic condensed matter environments[1-5].

The modeling of Eq.(1) with quantification process met however difficulty to predict high level reaction rate, due to very short life time (about $10^{-21\text{-}22}$ s was assumed) of ^{4}He*(Ex=23.8MeV), from proven nuclear physics knowledge[8]. The author elaborated the model to the "simultaneous" 3D and 4D fusion models in the dynamic environment of PdD lattice with excited D-harmonic oscillators (phonons)[9] to be able to predict more than several watts/cc-PdD excess heat with ^{4}He ash (23.8 MeV/^{4}He) and predict also much less (on the order of 10^{-6} to 10^{-12} of helium yield) of tritium and neutron production. It was modeled that fusion reactions by deuteron transient clusters would take place as the following competition process of 2D, 3D and 4D fusions.

The formation of transient clusters of 2D, 3D and 4D was modeled to approximately quantify based on the concept shown with Fig.1.

$$d + d \rightarrow {}^4He^*(Ex = 23.8\,MeV);\ {}^4He^* + d \rightarrow {}^4He\,(g.s) + d + 23.8\,MeV \quad (1)$$

$$d + d \rightarrow n + {}^3He + 3.27\,MeV\ (50\,\%);\ p + t + 4.03\,MeV\ (50\,\%) \quad (2)$$

$$d + d + d \rightarrow {}^3He + t + 9.5\,MeV\ (about\ 50\,\%);\ {}^4He + d + 23.8\,MeV\ (about\ 50\,\%) \quad (3)$$

$$d + d + d + d \rightarrow {}^4He + {}^4He + 47.6\,MeV \quad (4)$$

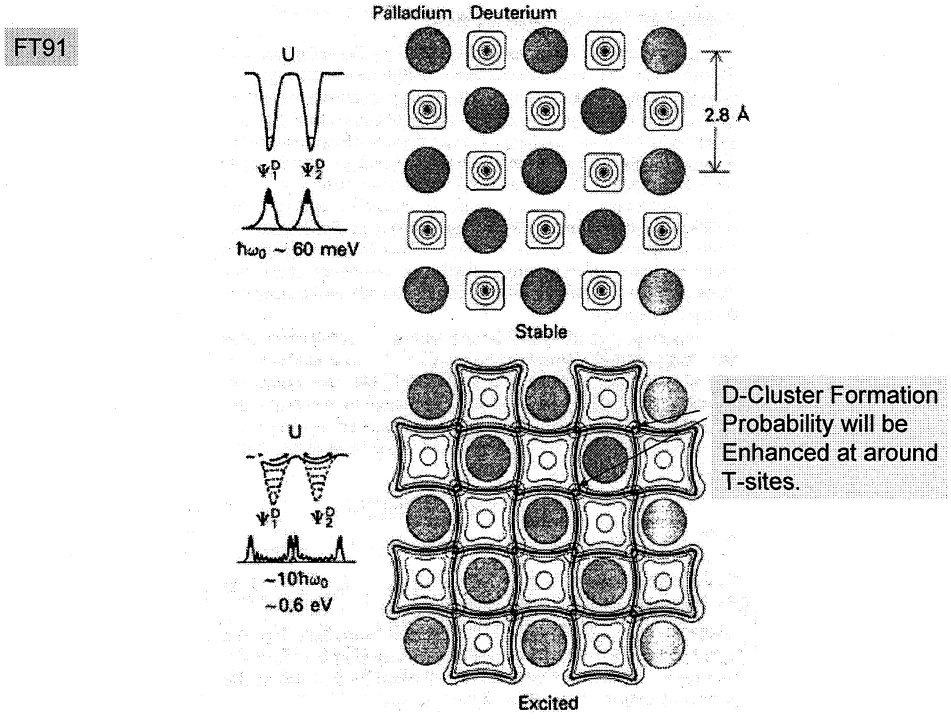

Fig.1: Modeling of transient D-cluster formation under D-harmonic oscillator of PdD lattice[9)]

Deuterons sit at O-sites as Einstein oscillator (harmonic oscillator), and have Gaussian wave function for the ground state (energy eigen-value is 32 meV). At higher phonon-excited states, D-wave function (Hermite function) changes to draw "U" shape distribution to enhance meeting probability of plural deuterons around the T-site. Fusion rates by 3D and 4D can take over 2D fusion rates in high phonon excited states[9)].

We elaborated the multi-body fusion model including modeling on multi-body strong interaction based on PEF (pion exchange force) concept and final state interaction channels[10-11)].

The time-window about 50 fs was conceived for transient 4D cluster formation with about 10 GHz lattice plasma-oscillation under D-phonon excitation as illustrated in **Fig.2**[11)]. We also roughly estimated D-cluster formation probabilities as shown in **Fi.g.3**, as a function of D-phonon energy (one phonon = 64 meV was used). Competing fusion rates were then estimated as copied in **Fig.4**.

Later, we elaborated that we needed to consider electron spin combination (in Step-2[1,2)]) and the Platonic symmetry (in Step-3[3-5)]) for constraint/ordering process in lattice dynamics, for D-cluster formation. We also found later by the Langevin equation analyses[3-5)] that the initial time window for 4D/TSC formation with much shorter interval as 1.0×10^{-18} s was enough for further 4D/TSC condensation. Also, very small 4D cluster formation probability as 10^{-11} can already realize[4, 5)] enough high 4D fusion rates to meet one watt/cc level nuclear heat level. So, we need to re-quantify cluster formation probabilities with more sophisticated solid state physics (or surface physics) modeling in future.

However, our Step-1 theories could explain why deuteron-related nuclear reaction with observable excess heat level with helium-4 main ash was possible with apparently radiation less nuclear products. To prove the super-screening scenario of mutual Coulomb barriers among deuterons, we needed further elaboration in Step-2 and Ste-3.

We have made experimental effort[18)] to observe neutron spectra from Pd/D_2O electrolysis cell, and could detect small component

of 2.45MeV neutrons by 2D fusion with higher energy component in 5-7 MeV region which might be attributed to 3D fusion.

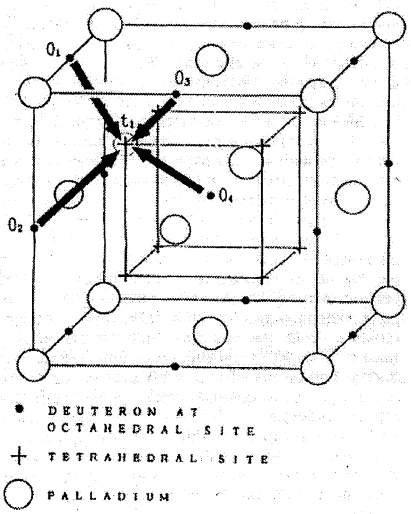

Fig. 1. The FCC lattice of PdD_x and squeezing of o-site deuterons onto the t-site.

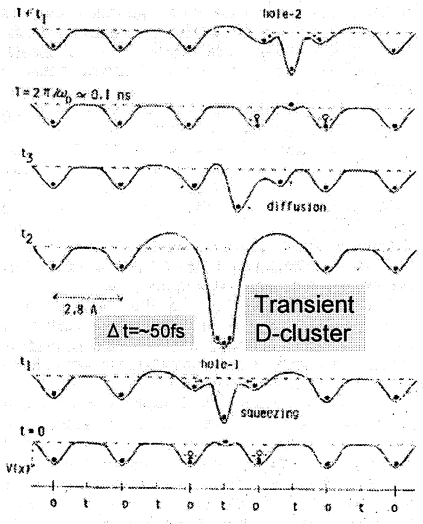

Fig. 3. Image of transient dynamics for microscopic clustering of deuterons.

Fig.2: Illustration of transient D-cluster formation around T-site (left figure) and D-plasma oscillation with time window for D-cluster formation about 50 fs (right figure), copied from the reference-11.

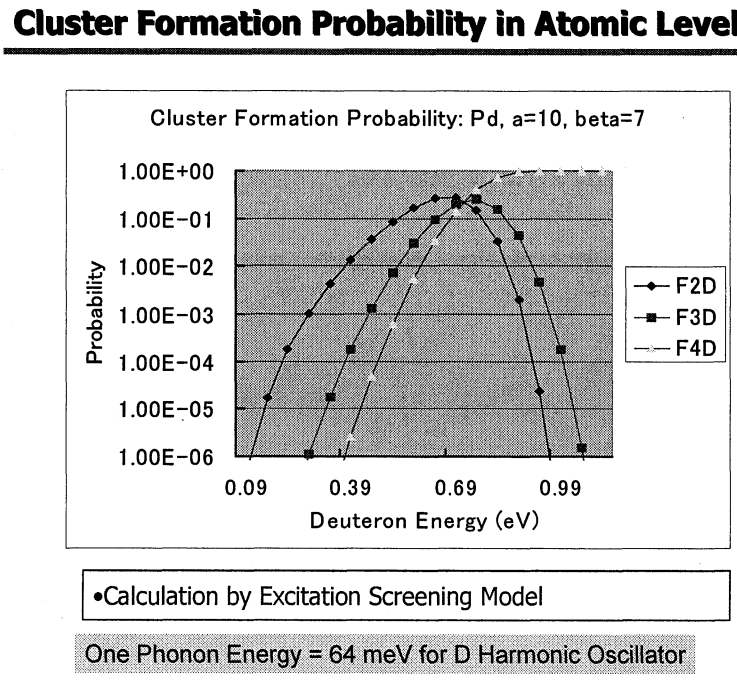

Fig.3: Estimation of 2D, 3D and 4D cluster formation probability around T-site of PdD lattice as a function of D-phonon excitation energy[11]

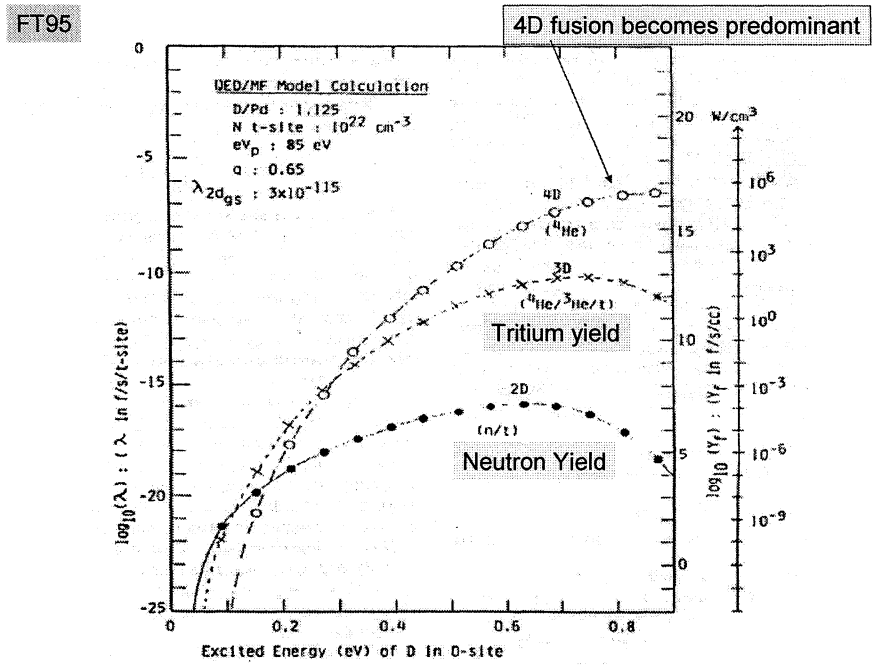

Fig. 4. Roughly estimated fusion rates in PdD_x, by the current model.

Fig.4: Comparison of logarithmic fusion rates between 2D, 3D and 4D fusions in PdD as a function of D-phonon excitation energy[11]

Using low energy deuteron beam implanted into TiDx target, we have intensively studied if there happened traces of 3D fusion, by detecting 4.75MeV triton and 4.75MeV ^{3}He emission[19-23]. We observed anomalous [3D]/[2D] yield ratios, on the order of 10^{-4}, which were 10^{26} times enhanced from theoretical value by the ordinary random reaction model of nuclear physics.

There should be existing close <d-d> pairs with significant amount in time-average in TiDx target under D-beam irradiation.

2. Step-2 EQPET/TSC Models

Elaboration of EQPET/TSC (electronic quasi-particle expansion theory/ tetrahedral symmetric condensate) models was reviewed in our recent papers[1,2].

We have proposed the multi-body deuteron fusion processes by formation of TSC (Tetrahedral Symmetric Condensate) and OSC (Octahedral Symmetric Condensate)[12,13]. Some numerical results were given by EQPET analyses, which could explain 3-78 W/cc power with 1.0×10^{11} f/s/cc to 1.0×10^{13} f/s/cc of ^{4}He-atoms production by 4D and 8D fusion reactions, with neutron production rate to be smaller than the rate of 10 n/s/cc.

There are remained open questions about where TSC is formed. We have proposed two mechanisms, as transient motion forming deuteron-clusters with short life time (60 fs).

In the near surface region of PdDx cathode, deuterium full loading (x=1; PdD) may be attained by electrolysis, gas discharge or gas-permeation, at least locally. No experimental techniques have been developed to measure local distribution of x-value, although we know that it should be key information. With very small density (namely 1 ppm was assumed in our paper[12]) PdD_2 states may exist. We can obtain only averaged D/Pd ratio over balk sample by experimental techniques used until now.

Trapped D in Bloch potential has discrete energies with 32 meV of the ground state and 64 meV of one phonon energy for excited states. Over 0.22 eV, all D-ions in lattice diffuse out of solid if excitation happens at every O-site. By exciting with external UV or

EUV laser, due to the classical Drude model, transient cluster of TSC can be formed with certain probabilities[12], in limited places as near surface region. An illustration of imagined state of moment for 4D/TSC (t=0) formation at a focal point (T-site in this case) is copied[1] in **Fig.5**.

Other speculative models for initiation of 4D(or H)/TSC (t=0) were discussed in references 3-5.

In EQPET models, we assumed that the total 4D wave function can be expanded by the linear combination of partial wave functions of dde* type molecules with regular electron state e(1,1) and electronic quasi-particle states as e*(2,2) Cooper pair, e*(4,4) quadruplet, and so on.

$$|\Psi_N\rangle = a_1|\Psi_{(1,1)}\rangle + a_2|\Psi_{(2,2)}\rangle + a_4|\Psi_{(4,4)}\rangle + a_6|\Psi_{(6,6)}\rangle + a_8|\Psi_{(8,8)}\rangle \quad (5)$$

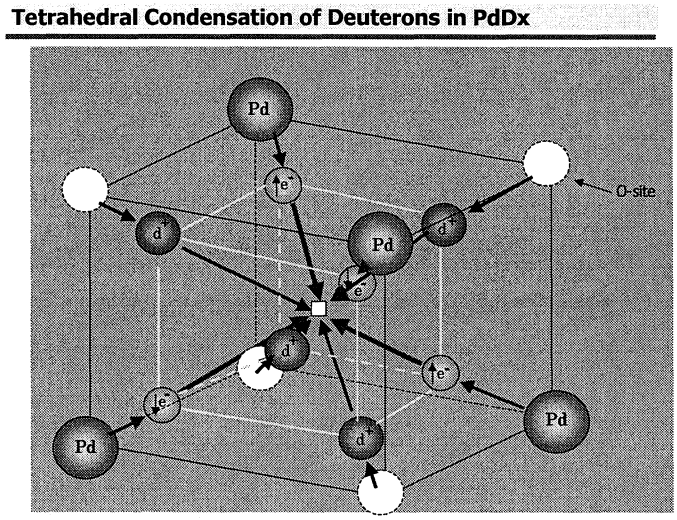

Fig.5: Illustration of initially formed 4D/TSC (t=0) around some T-sites in PdD lattice under D-phonon excitation[1]

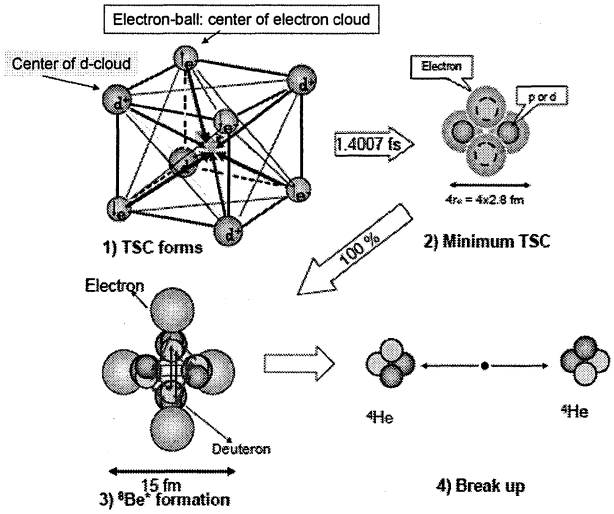

Fig.4: Illustration of 4D/TSC squeezing motion and 4D cluster fusion

Fig.6: Schematic steps of 4D/TSC condensation motion; 1) TSC (T=0) is just formed, 2) TSC gets to the minimum size state after about 1.4 fs condensation time[3,4], 3) strong interaction among 4d forms ^{8}Be* intermediate excited nucleus, 4) ^{8}Be* makes final state interaction to break up

$$\lambda_N = a_1^2 \lambda_{(1,1)} + a_2^2 \lambda_{(2,2)} + a_4^2 \lambda_{(4,4)} + a_6^2 \lambda_{(6,6)} + a_8^2 \lambda_{(8,8)} \quad (6)$$

$$\lambda_{nd(i,j)} = \nu(S_{nd} / E_d) \exp(-n\Gamma_{(i,j)}) \quad (7)$$

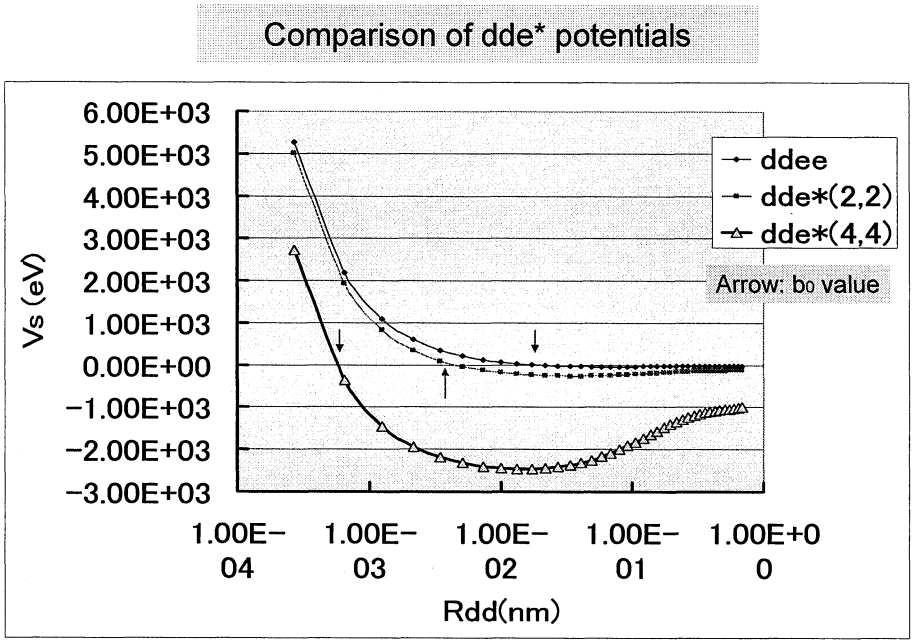

Fig.7: Comparison of d-d pair trapping potentials between D_2 molecule, dde*(2,2) and dde*(4,4)

Screening energies for d-d reaction are compared in **Table-1**[2].

Table-1: Screened energies for various EQPET molecules

e*(m*/me, e*/e)	Screening Energy Us (eV) dde*	dde*e*	b_0 (pm) dde*	dde*e*
(1, 1) ; Normal electron	36	72	40	20
(2, 2) ; Cooper pair	360	411	4	2
(4, 4) ; Quadruplet	4,000	1,108	0.36	1.3
(8,8) ; Octal coupling	22,154	960	0.065	1.5
(208, 1) ; muon	7,579	7,200	0.19	0.20

Table-2: Typical results by EQPET/TSC for fusion rates, power level and products, for TSC in PdDx, assuming N_{4D} = 1E+22 (1/cc)

Multi-body	Microscopic fusion rate (f/cl/s)	Macroscopic Yield (f/s/cc), Power (W/cc)	Ash (fusion products)
2D	1.9E-21	1.9E+1 (f/s/cc), 1.9E-11(W/cc)	Neutron; 10 n/s/cc
3D	1.6E-13	1.6E+9 (f/s/cc), 1.6E-3 (W/cc)	Tritium; 8E+8 t/s/cc
4D	3.1E-11	3.1E+11(f/s/cc), 3.1E+0 (W/cc)	Helium-4; 3E+11 h/s/cc

In **Fig.6**, condensation motion of 4D/TSC is illustrated reflecting the numerical results that we obtained in the Step-3 studies[3-5]. Modal fusion rate is defined[1] by Eq.6). Screening effect by bosonized electronic quasi-particle was estimated by using d-d pair trapping potentials of dde*-type molecules. Estimated fusion rates are shown in **Table-2**. Modal fusion rate given by Eq.(6) for 4D fusion is attributed almost 100% to the quadruplet EQPET molecule dde*(4,4) sate. Therefore, the accuracy of this model is closely related to what the minimum size sate of 4d/TSC is.

Later, we have considered that the squeezing motion of TSC can be more simply treated by a semi-classical model, because of the three-dimensionally constrained motion of 4d and 4e particles in TSC into the central focal point. **Figure-6** illustrates the feature of the semi-classical treatment. Every QM (quantum mechanical) particle-center in TSC can make central squeezing motion with same velocity, to keep charge neutrality of total TSC system – in other words to satisfy minimum system energy state (as calculated by the variational principle of quantum mechanics). Therefore this squeezing motion can be treated as Newtonian mechanics until when 4 deuterons get into the range (about 5 fm) of strong nuclear interaction. When 4 electrons start to separate at minimum TSC state, 4 deuterons suddenly start to *feel* mutual Coulomb repulsion. Nuclear interaction at this stage can be approximately treated by STTBA (Sudden Tall Thin Barrier Approximation) [2].

More rigorous time-dependent treatment of TSC motion was done based on Langevin equation in Step-3[3-5].

We obtained: λ_{4d} = 2.3E-4 f/s/cl at TSC-minimum state, by STTBA calculation. This microscopic fusion rate is 10^7 times larger order of value than one given in Table-2. We consider therefore that EQPET model gave significant underestimation for 4D fusion rate when rigid constraint of motion in three dimensional TSC motion in condensed matter is attained as shown in Fig.5.

TSC squeezes from about 100 pm size to its minimum-size with about 10-20 fm diameter and behaves as *charge-neutral pseudo-particle*. Life time of TSC is estimated as time difference from 100 pm size state to minimum size with velocity of the order of 10^5 cm/s; we obtain about 60 fs. (This is later found to be much shorter as 1.4 fs as we obtained in Step-3[3-5]) . During its life, TSC as charge-neutral pseudo-particle may approach to host-metal nuclei with some probability when TSC size becomes smaller than the orbit size (about 1 pm) of inner most K-shell electron orbit of host metal nucleus target and TSC has drift momentum of Center-of-Mass system, as illustrated in **Fig.8.**

We proposed therefore the interaction models between TSC-min state of either deuteron-cluster or proton-cluster and host metal large nucleus to induce 4d or 1p to 4p capture process[14]. This model of TSC-induced 4D fusion and transmutations could well explain ^{4}He production with excess heat results by Arata [15] and McKubre[16] and selective transmutation results by Iwamura[17].

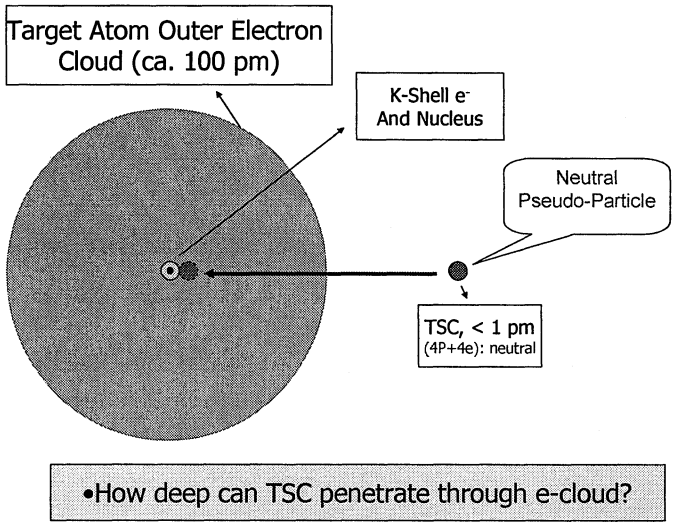

Fig.8: Illustration for TSC and host-metal atom interaction[14)]

3. Step-3 D-Cluster Dynamics and Fusion Rate by Langevin Equation

To explain apparent hard-radiation-less excess heat with helium-4 ash in CMNS (condensed matter nuclear science) experiments, especially in dynamic PdDx systems, we have done a long (1989-2007 or more) series of study for modeling D-cluster (or multi-body deuteron) fusion reaction mechanisms to reach at our latest theory in Step-3 studies based on Langevin equations[3-5)].

The basics of methods with Langevin equations for D-cluster dynamics, especially for D-atom, D_2 molecule, D_2^+ ion, D_3^+ ion, 4D/TSC (tetrahedral symmetric condensate) and $6D^{2+}$/OSC (octahedral symmetric condensate) are written in our latest paper[5)].

First one-dimensional Langevin equations for D-clusters with the R_{dd} (d-d distance) are formulated under the Platonic symmtery[3)] of multi-particle D-cluster systems with deuterons and quantum-mechanical electron centers. Under the orthogonally coupled Platonic symmetry for a Platonic deuteron-system and a Platonic electron system, dynamic equations for so-many-body system of deuterons and electrons with metal atoms (more than 4 deuterons plus 4 1s electrons of deuterium atoms plus 40 4d-shell electrons of 4 Pd atoms in fcc lattice plus surrounding lattice atoms under D-phonon excited states should be considered in our modeling[1)]), a simple one-dimensional Langevin equation for the inter-nuclear d-d distance R_{dd} can be formulated, as we showed in the paper[5)]. By the ensemble averaging of Langevin equation with the weight of quantum mechanical wave-functions for electrons and deuterons, we could further derive a time dependent one-dimensional Langevin equation for expectation value $<R_{dd}>$, which is nonlinear, but could be solved by the Verlet's time step method[3,4)]. We showed in our papers[5)] that only 4D(or H)/TSC can condense ultimately to be finally very small charge neutral entity with about 10-20 fm radius. At the final stage of 4D/TSC condensation in about $2x10^{-20}$ s, 4D fusion with 2 ^{4}He products takes place with almost 100% probability, according to our HMEQPET calculation for barrier factors and fusion rate formula by the Fermi's first golden rule[1)].

Basic Langevin equation for a Platonic symmetric D-cluster having N_e d-d edges and N_f faces of d-d-e (D_2^+)or d-e-d-e(D_2) type is written by Eq.(8). Here, R is the d-d distance and m_d is the deuteron mass, V_s is the d-d pair trapping potential of either d-e-d-e or d-d-e type molecule. The first term of right side in Eq.(8) is the total Coulomb force of D-cluster system, and f(t) is the fluctuation of force for which we introduce quantum mechanical fluctuation of deuteron positions under condensation motion. The

quantum mechanical effect of electron clouds is incorporated with the second term of right hand side as "friction" in Langevin equation. For D_2 molecule, N_e=N_f=1. For D_3^+ ion which is known as stable in vacuum, N_e=3 and N_f=6 are given. For 4D/TSC, N_e=6 and N_f=6 are given. For $6D^{2-}$, N_e=12 and N_f=24 are given.

By taking QM ensemble average with d-d pair wave function, assumed as Gaussian distribution, we derived Langevin equation of expectation value for 4D/TSC as Eq.(9). By taking QM ensemble average of Eq.(10), we obtained Eq.(13). We obtained the time-dependent TSC-cluster trapping potential[4] as Eq.(14).

Similar Langevin equation and trapping potential were derived for $6D^{2-}$ molecule also. We compared central potential curve (at R'=R_{dd}) in **Fig.9**. We found that 4D(or H)/TSC can condensate ultimately to very small charge neutral entity and has no stable or ground state. This may be the reason that we do not observe D_4 stable molecule in nature. On the contrary, $3D^+$ (D_3^+) molecule and $6D^{2-}$ molecule have stable and ground states[5].

Equation (13) was numerically solved by the Verlet method[4], as result is shown in **Fig.10**.

Time dependent barrier penetration probabilities (as a function of R_{dd}, since we have one-to-one relation between elapsed time and $R_{dd}(t)$) is shown in **Table-3.**

$$N_e m_d \frac{d^2 R}{dt^2} = -\frac{k}{R^2} - N_f \frac{\partial V_s}{\partial R} + f(t) \tag{8}$$

$$6 m_d \frac{d^2 R_{dd}(t)}{dt^2} = -\frac{11.85}{[R_{dd}(t)]^2} - 6\frac{\partial V_{s2}(R_{dd}(t);1,1)}{\partial R_{dd}(t)} + \langle f(t)\rangle + f'(t) \tag{9}$$

$$f'(t) = f(t) - \langle f(t)\rangle \tag{10}$$

$$f(t) = [-\frac{\partial \Delta E_c(R_{dd})}{\partial R_{dd}}] \bmod[\ X^2(R'_{dd}; R_{dd}(t))] \tag{11}$$

$$X^2(R'_{dd}; R_{dd}(t)) = \frac{1}{\sqrt{2\pi\sigma^2}} \exp[-(R'_{dd} - R_{dd}(t))^2/(2\sigma^2)] \tag{12}$$

$$6 m_d \frac{d^2\langle R_{dd}\rangle}{dt^2} = -\frac{11.85}{\langle R_{dd}\rangle^2} - 6\frac{\partial V_s(\langle R_{dd}\rangle; m, Z)}{\partial\langle R_{dd}\rangle} + 6.6\left\langle \frac{(R'-R_{dd})^2}{R_{dd}^4}\right\rangle \tag{13}$$

$$V_{tsc}(R': R_{dd}(t)) = -\frac{11.85}{R_{dd}(t)} + 6V_s(R_{dd}(t); m, Z) + 2.2\frac{|R'-R_{dd}(t)|^3}{[R_{dd}(t)]^4} \tag{14}$$

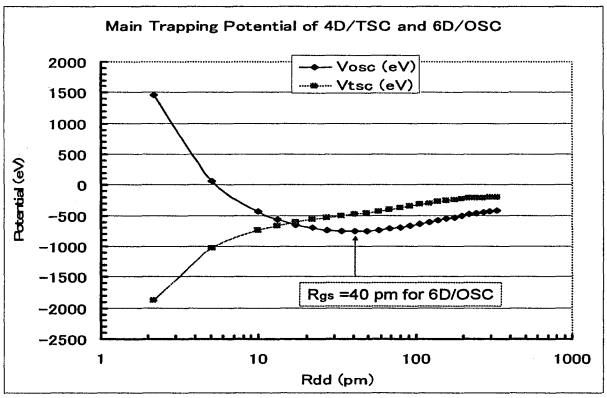

Fig.9: Comparison of cluster trapping potential between 4D/TSC and $6D^{2-}$/OSC. TSC condenses ultimately to very small R_{dd} value (ends at R_{dd}-min=about 20 fm), while OSC converges at R_{dd}=about 40 pm (corresponding to the ground state).

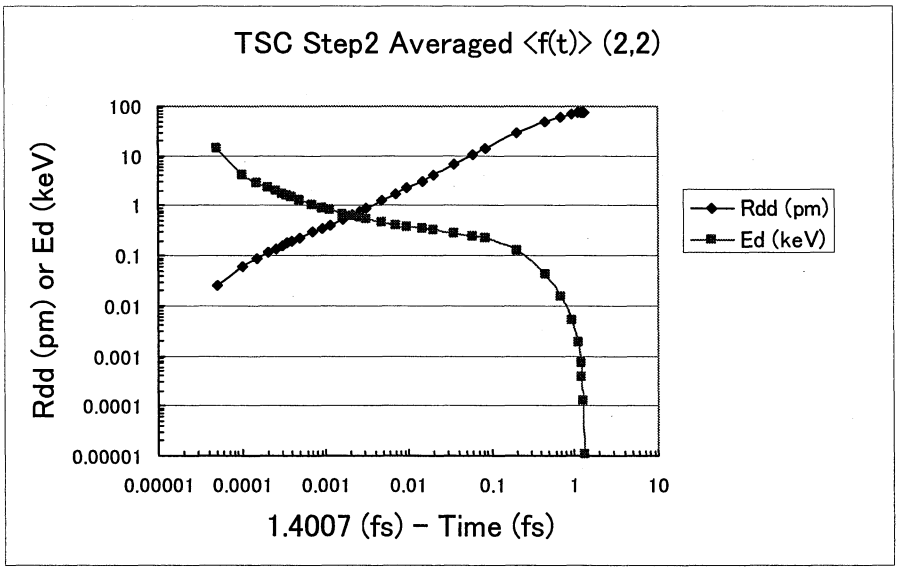

Fig.10: Numerical solution of Eq.(13) by the Verlet method[4]. Time is reversed starting from the condensation time 1.4007 fs.

Table-3: Calculated time-dependent (equivalently R_{dd} dependent) barrier factors of 4D/TSC condensation motion

Barrier Factors of 4D/TSC under condensation, Calculated by HMEQPET Code

$R_{dd}=R_{gs}$ (pm)	P_{2d} ; 2D Barrier Factor	P_{4d}; 4D Barrier Factor
0.0206 (TSC-min)	4.44E-2	1.98E-3
0.0412	1.06E-2	1.12E-4
0.103	1.43E-3	2.05E-6
0.206	3.35E-5	1.12E-9
0.412	9.40E-7	2.16E-13
0.805 (μ dd)	1.00E-9	1.00E-18
1.03	9.69E-11	9.40E-21
2.06	6.89E-15	4.75E-29
4.12	9.38E-21	8.79E-41
10.3	2.16E-32	4.67E-64
21.8 (dde*(2,2)	1.30E-46	1.69E-92
74.1 (D2 molecule)	1.00E-85	1.00E-170

Fusion rate is calculated by the following Fermi's golden rule[1],

$$\lambda_{nd} = \frac{2}{\hbar}\langle W \rangle P_{nd}(r_0) = 3.04 \times 10^{21} P_{nd}(r_0)\langle W \rangle \tag{15}$$

Here P_{nd} is barrier factor for nD-cluster and <W> is the averaged value of imaginary part of nuclear optical potential[1]. The extrapolation of <W> value to 4d fusion was made[4] by using the scaling law $\langle W \rangle \propto (PEF)^5$ with PEF-value which is given in unit of derivative of one pion exchange potential (OPEP) (simple case of Hamada-Johnston potential[5] for pion exchange model). We got the next value of 4D fusion yield per TSC generation,

$$\eta_{4d} = 1 - \exp(-\int_0^{t_c} \lambda_{4d}(t)dt) \qquad (16)$$

Using time-dependent barrier factors as given in Table-3, we obtained $\eta_{4d} \cong 1.0$. *This result means that:*

We have obtained that 4D fusion may take place with almost 100 % yield per a TSC generation, so that macroscopic 4d fusion yield is given by simply with TSC generation rate Q_{tsc} in the experimental conditions of CMNS.

However, when we consider that one deuteron has spin-parity 1+ and combination of 4d has total spin state 4, 3, 2, 1 and 0, the 4d fusion with out-going channel to two ^{4}He (0+:gs) particles is forbidden, by spin-parity conservation (for S-wave in/out channels), except for the 0+ spin-parity state (T=0) of 4d combination, to be explained detail analysis including P-wave and D-wave states with isospin elsewhere.

The ultimate condensation is possible only when the double Platonic symmetry of 4D/TSC is kept in its dynamic motion. The sufficient increase (super screening) of barrier factor is also only possible as far as the Platonic symmetric 4D/TSC system is kept. Therefore, there should be always 4 deuterons in barrier penetration and fusion process, so that 4d simultaneous fusion should take place predominantly. The portion of 2D (usual) fusion rate is considered to be negligible[4]. Maximum d-d fusion rate seems to appear in the condition near dde*(2,2) state which gives the d-d fusion rate of order of 1.0E-27 f/s/pair[4], and additional electrons atmosphere in condensed matter around dd-pair may induce minor screening effect.

Typical nuclear products of 4D fusion are predicted to be two 23.8 MeV α-particles[1,2]. although the final state interaction of ^{8}Be* is complex yet to be studied. 4H/TSC[14] should condense in the same way until when TSC-min state with classical electron radius (2.8 fm)[2] comes, but no strong interaction exists among protons and there will make 1p to 4p capture transmutations (strong interaction with <n> states of host nucleus) with host metal nuclei when 4H/TSC has sufficient drift (Center-of-Mass) momentum.

4. Concluding Remarks

How to super-screen Coulomb barrier, how to be ^{4}He of ash and why to have no apparent hard radiations are able to be resolved by the 4D/TSC dynamic condensation motion, basically. The Langevin equation-based analysis can be extended for neutral clusters as 6D/OSC and 8D/OSC with further elaboration of substantial modeling.

Main future works should be considered as:

1) How to enhance 4D/TSC(t=0) rate in nano-structure of metal-deuterium systems should be investigated, since this gives key information of stimulation-conditions in experiments. TSC formation process in regular PdD lattice under external stimulation, on surface of nano-particle or nano-structure samples or interfaces with incoming deuteron (or D_2) flux should be modeled or experimentally tried.

2) Detail of ^{8}Be* final state interaction and out-going channels should be studied. This compound excited state may have complex final state interaction to various out-going channels as α + ^{4}He*(Ex<47.6MeV) + (47.6MeV-Ex), gamma-transition of ^{8}Be*(47.6MeV-E_γ) + Eγ and minor channels of n, p, and t emission. Lower excited states of ^{8}Be* have many out-going channels to ^{4}He(g.s) + ^{4}He(g.s) with each lower kinetic energy than 23.8MeV. Combination of spin-parities and isospins are complex. Charged particle spectroscopy and particle-identification by experiments should be cross-checked with such theoretical predictions.

Acknowledgment: The author is very grateful to many former co-workers and supporting institutions and companies for a long series of study in 1989-2007. Currently, work is supported by Technova Inc., Tokyo, Japan.

References:

1) A. Takahashi, N. Yabuuchi: Fusion rates of bosonized condensates, *J. Condensed Matter Nuclear Science*, 1 (2007)106-128

2) A. Takahashi: A theoretical summary of condensed matter nuclear effects, *J. Condensed Matter Nuclear Science*, 1 (2007)129-141;

See also A. Takahashi: Brief Theoretical Summary of Condensed Matter Nuclear Effects, *Acta Physica et Chemica*, Debrecen, Hungary, Vol.38-39, (2005)341-356

3) A. Takahashi, N. Yabuuchi: Condensed matter nuclear effects under platonic symmetry, Proc. ICCF13, Sochi, Russia, 2007 (to be published)

4) A. Takahashi, N. Yabuuchi: Study on 4D/TSC condensation motion by non-linear Langevin equation, *LENR Source Book*, American Chemical Society, 2007, to be published from Oxford University Press

5) A. Takahashi, N. Yabuuchi: D-Cluster Dynamics and Fusion Rate by Langevin Equation, Proc. 8th Int. Workshop on Anomalies in D/H Loaded Metals, Catania, Italy, October, 2007, to be published

6) M. Fleischmann, S. Pons: *J. Electyroanal. Chem.*, 261 (1989)301

7) A. Takahashi: *J. Nucl. Sci. Tech.*, 26 (1989)558-550

8) A. Takahashi, N. Yabuuchi: Deuterons-to-^{4}He Channels, Proc. ICCF13, Sochi, Russia, 2007, to be published

9) A. Takahashi, et al: *Fusion Technology*, 19(1991)380-390 (submitted December 1989)

10) A. Takahashi, et al.: Excess heat and nuclear products by D_2O/Pd electrolysis and multi-body fusion, *Int. J. Appl. Electromagnetics in Materials*, El Sevier, 3(1992)221-230

11) A. Takahashi, et al: Multi-body fusion model to explain experimental results, *Fusion Technology*, 27(1995)71-85

12) A. Takahashi: Deuteron cluster fusion ans ash, *J. Condensed Matter Nucl. Sci.*, 1 (2007)62-85

13) A. Takahashi : Deuteron cluster fusion and related nuclear reactions in metal-deuterium/hydrogen systems, *Recent Res. Devel. Physics*, 6(2005)1-28, ISBN: 81-7895-171-1, Transworld Research Network

14) A. Takahashi: TSC-induced nuclear reactions and cold transmutations, *J. Condensed Matter Nucl. Sci.*, 1 (2207)86-96

15) Y. Arata: *Ill Nuovo Aggiatore*, 38(2005)66-71

16) M. McKubre, et al: Proc. ICCF10, *Condensed Matter Nuclear Science*, WSPC, pp.199-212 (2006)

17) Y. Iwamura, et al : *Jpn J. Appl. Phys.*, 41 (2002)4642-4650

18) A. Takahashi, et al : *J. Nucl. Sci. Tech.*, 27(1990)663-666

19) A. Takahashi, et al: *Fusion Technology*, 34 (1998)256-272

20) K. Ochiai, et al : *Fusion technology*, 36(1999)315-323

21) A. Takahashi, et al : Proc. ICCF10, *Condensed Matter Nuclear Science*, WSPC, pp.657-665 (2006)

22) Y. Isobe, et al: *Jpn J. Appl. Phys.*, 41(2002)1546-1556

23) A. Takahashi, et al : *Phys. Lett. A*, 255(1999)89-97

Effect on the Energy Level of a Hydrogen Atom Due to Magentic Interaction

OZAKI Masao, Tokyo University of Agriculture: m1ozaki@nodai.ac.jp

Abstract: An attractive model to explain cold fusion phenomena was proposed by Vigier and was developed by Samsonenko *et al.* They numerically obtained a new quantum level (a few keV) of a hydrogen atom. They solved Schrödinger's equation for two-body system (a proton and an electron) under the influence of magnetic interactions between them. The lowest energy state was not mentioned in the paper, because its value probably came to relativistic regime. Therefore, we formulate this model by Dirac equation and investigate an effect on energy levels due to magnetic interaction. We speculate the lowest energy state comparable in the order of that of the ordinary theory.

1. Introduction

Samsonenko *et al.*[1] developed an attarctive model, proposed by Vigier, to show a new enegy level of a hydrogen atom. They obtained about 40 keV bound state, which was not the lowest energy state. Although they did not mention, the lowest energy state had ridiculously large bounding energy. We shall briefly review their paper. Hamiltonian H of Schrödinger's equation for two-body system (p-e$^-$) including the effect of magenetic moments of both p and e$^-$,

$$\begin{aligned} H &= \frac{1}{2m_e}\left[\boldsymbol{p}_e + \frac{e}{c}\boldsymbol{M}_p \times \frac{\boldsymbol{r}_e - \boldsymbol{r}_p}{|\boldsymbol{r}_e - \boldsymbol{r}_p|^3}\right]^2 \\ &+ \frac{1}{2m_p}\left[\boldsymbol{p}_p - \frac{e}{c}\boldsymbol{M}_e \times \frac{\boldsymbol{r}_p - \boldsymbol{r}_e}{|\boldsymbol{r}_e - \boldsymbol{r}_p|^3}\right]^2 \\ &+ \frac{q_e q_p}{|\boldsymbol{r}_e - \boldsymbol{r}_p|} \end{aligned}$$

where, the suffixes e, p denote electron and proton, respectively, and $\boldsymbol{M}_e$, $\boldsymbol{M}_p$ are their magnetic moments. CGS unit is used in this section. Introducing the center of mass coordinate, $\boldsymbol{R} = \boldsymbol{r}_e + \boldsymbol{r}_p$, and the relative coordinates, $\boldsymbol{r} = \boldsymbol{r}_e - \boldsymbol{r}_p$, the corresponding masses and momenta are $M = m_e + m_p$, $\mu = \frac{m_e m_p}{m_e + m_p}$, $\boldsymbol{P} = \boldsymbol{p}_e + \boldsymbol{p}_p$, $\boldsymbol{p} = \frac{m_p \boldsymbol{p}_e - m_e \boldsymbol{p}_p}{M}$. Assuming the magnetic moments in the following form, $\boldsymbol{M}_e = -(e\hbar/2m_e c)\boldsymbol{\sigma}_e$, $\boldsymbol{M}_p = (e\hbar/2m_p c)\boldsymbol{\sigma}_p$, the Hamiltonian in the center of mass system is

$$H = \frac{\boldsymbol{p}^2}{2\mu} - \frac{e^2}{r} + \frac{e^2\hbar(\boldsymbol{\sigma}\cdot\boldsymbol{L})}{2c^2 m_e m_p r^3} + \frac{e^4\hbar^2}{4c^4\mu m_e m_p r^4}$$

where, $\boldsymbol{\sigma} = \boldsymbol{\sigma}_e + \boldsymbol{\sigma}_p$.
Consodering the equation in spherical coordinates of stationary state, the radial function $R(r)$ satisfies

$$(r^2R')' + \frac{2\mu r^2}{\hbar^2}\left[E + \frac{e^2}{r} - \frac{\hbar^2\ell(\ell+1)}{2\mu r^2} - \frac{e^2\hbar\sigma}{2c^2 m_e m_p r^3} - \frac{e^4\hbar^2}{4c^4\mu m_e m_p r^4}\right] R(r) = 0$$

where, the operator $(\boldsymbol{\sigma}\cdot\boldsymbol{L})$ is replaced by its eigenvalue σ. Setting $X = rR$,

$$X'' + \frac{2\mu}{\hbar^2}\left[E + \frac{e^2}{r} - \frac{\hbar^2\ell(\ell+1)}{2\mu r^2} - \frac{e^2\hbar\sigma}{2c^2 m_e m_p r^3} - \frac{e^4\hbar^2}{4c^4\mu m_e m_p r^4}\right] X(r) = 0$$

Finding the solutions in the following form after the method proposed by Özçelik and M. Şimşek[2],

$$X(r) = f(r) r^{\alpha} e^{-\kappa r} r e^{-\theta/r} \qquad (1)$$

where,

$$\begin{aligned} f(r) &= \textstyle\prod_{i=1}^{n}(r - \alpha_i^{(n)}), & n > 0 \\ &= 1, & n = 0. \end{aligned}$$

They numerically obtained a solution with n=1, ℓ=0, and its energy was about 40 keV. They did not mention the primary solution with $n = 0$. Its energy is estimated to larger than GeV. Thus, the problem should be treated by the relativistic way.

2. Fundamental Equations

We consider an electron under influence of a proton, which is rest at the origin and has a magnetic moment $\boldsymbol{\mu}$. The Dirac equation for an electron with a minimal coupling, $\partial_\mu \rightarrow \partial_\mu - i(e/\hbar)A_\mu$,

$$(i\hbar c\gamma^\mu \partial_\mu - ce\gamma^\mu A_\mu - mc^2)\psi(x) = 0.$$

where we use so called Bjorken and Drell metric[3] $(+,-,-,-)$ and MKSA unit. Multiplying the above equation by the operator $(i\hbar\gamma^\mu\partial_\mu - q\gamma^\mu A_\mu + mc)$ and deviding by c,

$$[(i\hbar\gamma^\mu\partial_\mu + e\gamma^\mu A_\mu)^2 - (mc)^2]\psi = 0 \quad (2)$$

Eq. (2) is rewritten as

$$\left[\left(i\hbar\frac{\partial}{\partial t} + ecA_0\right)^2 - c^2\left(\frac{\hbar}{i}\boldsymbol{\nabla} + e\boldsymbol{A}\right)^2 + iec\hbar\boldsymbol{\alpha}\cdot\boldsymbol{E} - ec^2q\hbar\boldsymbol{\Sigma}\cdot\boldsymbol{B} - m^2c^4\right]\psi(\boldsymbol{r},t) = 0$$

where,

$$\boldsymbol{\alpha} = \begin{pmatrix} 0 & \boldsymbol{\sigma} \\ \boldsymbol{\sigma} & 0 \end{pmatrix}$$

$$\boldsymbol{\Sigma} = \begin{pmatrix} \boldsymbol{\sigma} & 0 \\ 0 & \boldsymbol{\sigma} \end{pmatrix}$$

Assuming a stationary wave function $\psi(\boldsymbol{r},t) = \Phi(\boldsymbol{r})e^{-iEt/\hbar}$, we obtain

$$\left[E^2 + \hbar^2c^2\boldsymbol{\nabla}^2 + iec^2\hbar\boldsymbol{\nabla}\cdot\boldsymbol{A} + 2eEcA_0 + 2ie\hbar c^2\boldsymbol{A}\cdot\boldsymbol{\nabla} + (ecA_0)^2 - e^2c^2\boldsymbol{A}^2 + iec\hbar\boldsymbol{\alpha}\cdot\boldsymbol{E} - ec^2\hbar\boldsymbol{\Sigma}\cdot\boldsymbol{B} - m^2c^4\right]\Phi(\boldsymbol{r}) = 0$$

3. Wave Equation Under the Effect of Proton's Magnetic Moment

The electromagnetic potential comes from the proton,

$$\boldsymbol{A}(\boldsymbol{r}) = \frac{\mu_0}{4\pi}\boldsymbol{\mu}\times\frac{\boldsymbol{r}}{r^3},$$

$$cA^0(\boldsymbol{r}) = \frac{e}{4\pi\epsilon_0 r},$$

then

$$\boldsymbol{E} = -\boldsymbol{\nabla}(cA^0) = \frac{e}{4\pi\epsilon_0 r^2}\frac{\boldsymbol{r}}{r}$$

$$\boldsymbol{B} = \boldsymbol{\nabla}\times\boldsymbol{A} = \frac{\mu_0}{4\pi}\left\{3\frac{(\boldsymbol{\mu}\cdot\boldsymbol{r})\boldsymbol{r}}{r^5} - \frac{\boldsymbol{\mu}}{r^3}\right\}.$$

Using these expressions and assuming $\boldsymbol{\mu} = \frac{e\hbar}{2m_p}\boldsymbol{\Sigma}$, many terms in the above equation reduce to relatively compact forms (see the Appendix)

$$\left[(E^2 - m^2c^4) + \hbar^2c^2\left(\frac{\partial^2}{\partial r^2} + \frac{2}{r}\frac{\partial}{\partial r} - \frac{\boldsymbol{L}^2}{r^2}\right) + \frac{2e^2E}{4\pi\epsilon_0 r} + \frac{ie^2\hbar c\boldsymbol{\alpha}\cdot\boldsymbol{r}}{4\pi\epsilon_0 r^3} + \left(\frac{e^2}{4\pi\epsilon_0 r}\right)^2 + \frac{e^2\hbar^2\boldsymbol{\Sigma}\cdot\boldsymbol{L}}{4\pi\epsilon_0 m_p r^3} - 2\left(\frac{e^2}{4\pi\epsilon_0 r}\right)^2\left(\frac{\hbar}{2m_p rc}\right)^2\right]\Phi(\boldsymbol{r}) = 0 \quad (3)$$

As in the central field problem, we intoroduce two operators,

$$K = \beta(1 + \boldsymbol{\Sigma}\cdot\boldsymbol{L}),$$

$$\Lambda = -\beta K - i\frac{e^2}{4\pi\epsilon_0\hbar c}\alpha_r,$$

where, $\alpha_r = \boldsymbol{\alpha}\cdot\frac{\boldsymbol{r}}{r}$ and

$$\beta = \begin{pmatrix} \mathbf{1} & 0 \\ 0 & -\mathbf{1} \end{pmatrix}.$$

K commutes the Hamiltonian H and the total angular momentum $\boldsymbol{J}$,

$$[K, H] = [K, \boldsymbol{J}] = 0.$$

Λ commutes K and $\boldsymbol{J}$ but does not commute H,

$$[\Lambda, K] = [\Lambda, \boldsymbol{J}] = 0,$$
$$[\Lambda, H] \neq 0$$

where,

$$H = c\boldsymbol{\alpha}\cdot\boldsymbol{p} + \beta mc^2 + \frac{\mu_0 e^2\hbar c}{8\pi m_p r^3}\boldsymbol{\alpha}\cdot\boldsymbol{\Sigma}\times\boldsymbol{r} - \frac{e^2}{4\pi\epsilon_0 r},$$

$$\hbar\boldsymbol{J} = \hbar\boldsymbol{L} + \frac{\hbar}{2}\boldsymbol{\Sigma}.$$

These operators satisfy

$$K^2 = 1 + \boldsymbol{L}^2 + \boldsymbol{\Sigma}\cdot\boldsymbol{L} = \boldsymbol{J}^2 + \frac{1}{4},$$

$$\Lambda^2 = K^2 - \left(\frac{e^2}{4\pi\epsilon_0\hbar c}\right)^2,$$

$$\Lambda(\Lambda+1) = \boldsymbol{L}^2 - \left(\frac{e^2}{4\pi\epsilon_0\hbar c}\right)^2 - i\frac{1}{\hbar c}\cdot\frac{e^2}{4\pi\epsilon_0}\alpha_r.$$

Now we have

$$\left[\frac{E^2-m^2c^4}{\hbar^2c^2}+\frac{\partial^2}{\partial r^2}+\frac{2}{r}\frac{\partial}{\partial r}-\frac{\Lambda(\Lambda+1)}{r^2}\right.$$
$$+\frac{2e^2E}{4\pi\epsilon_0\hbar^2c^2r}-\frac{e^2}{4\pi\epsilon_0}\frac{\boldsymbol{\Sigma}\cdot\boldsymbol{L}}{m_pc^2}\frac{1}{r^3}$$
$$\left.-2\left(\frac{e^2}{8\pi\epsilon_0m_pc^2}\right)^2\frac{1}{r^4}\right]\Phi(\boldsymbol{r})=0$$

Using $\boldsymbol{\Sigma}\cdot\boldsymbol{L}=\beta K-1$,

$$\left[\frac{E^2-m^2c^4}{\hbar^2c^2}+\frac{\partial^2}{\partial r^2}+\frac{2}{r}\frac{\partial}{\partial r}-\frac{\Lambda(\Lambda+1)}{r^2}\right.$$
$$+\frac{2e^2E}{4\pi\epsilon_0\hbar^2c^2r}-\frac{e^2}{4\pi\epsilon_0}\frac{\beta K-1}{m_pc^2}\frac{1}{r^3}$$
$$\left.+2\left(\frac{e^2}{8\pi\epsilon_02m_pc^2}\right)^2\frac{1}{r^4}\right]\Phi(\boldsymbol{r})=0$$

Replacing the operators K and Λ by their eigen values k and $\pm\lambda$, we have an equation for the radial part of the wave function $R(r)$ in the similar form in the nonrelativistic Coulomb problem. Setting $X(r)=rR(r)$,

$$\left[\frac{E^2-m^2c^4}{\hbar^2c^2}+\frac{d^2}{dr^2}-\frac{\pm\lambda(\pm\lambda+1)}{r^2}\right.$$
$$+\frac{2e^2E}{4\pi\epsilon_0\hbar^2c^2r}-\frac{e^2}{4\pi\epsilon_0}\frac{\beta k-1}{m_pc^2}\frac{1}{r^3}$$
$$\left.-2\left(\frac{e^2}{4\pi\epsilon_02m_pc^2}\right)^2\frac{1}{r^4}\right]X(r)=0$$

With the assumption that the upper two components of $X(r)$ dominates the lower components, we obtain an equation similar to that of Samsonenko *et al.*,

$$X''+\left[\frac{E^2-m^2c^4}{\hbar^2c^2}+\frac{2e^2E}{4\pi\epsilon_0\hbar^2c^2r}\right.$$
$$-\frac{\pm\lambda(\pm\lambda+1)}{r^2}-\frac{(k-1)e^2}{4\pi\epsilon_0m_pc^2r^3}$$
$$\left.-2\left(\frac{e^2}{4\pi\epsilon_02m_pc^2}\right)^2\frac{1}{r^4}\right]X(r)=0 \qquad (4)$$

where we have used the same notaion for one-component function as for that of four-component one.

We rewrite eq.(4) as

$$\frac{X''}{X}=-\epsilon+\frac{b_1}{r}+\frac{b_2}{r^2}+\frac{b_3}{r^3}+\frac{b_4}{r^4} \qquad (5)$$

where, $\epsilon=\frac{E^2-m^2c^4}{\hbar^2c^2}$, $b_1=-\frac{2e^2E}{4\pi\epsilon_0\hbar^2c^2}$, $b_2=\pm\lambda(\pm\lambda+1)$, $b_3=\frac{(k-1)e^2}{4\pi\epsilon_0m_pc^2}$, $b_4=2\left(\frac{e^2}{8\pi\epsilon_0m_pc^2}\right)^2$. Note that ϵ expresses the value proportional to the binding energy. We assume a solution with $n=0$ in eq.(1) in order to find the lowest energy value. After a little bit calculation (see the Appendix), we obtain energy eigenvalue $\epsilon^{\pm}$ is

$$\epsilon^{\pm}=-\frac{1}{16b_4}(b_2\pm\sqrt{b_2^2-2b_3b_1})^2 \qquad (6)$$

Assigning actual values of physical constant and taking account of the binding energy must be much smaller than mass energy, $|E-mc^2|<<mc^2$, we obtain the binding energy within the order estimation (see the Appendix)

$$E-mc^2\sim 6\times10^{-19}(J)\approx 3(eV)$$

The difference between our result and that of Samsonenko *et al.* comes from the mass ratio $(\frac{m_p}{m_e})^2$ in the factor of $1/r^4$ term. Although Samsonenko *et al.* brought in the magnetic moments of both an electron and a proton in the Hamiltonian, our model did in only a proton's magnetic moment.

4. Conclusion

We have investigated the Dirac equation for an electron under the effect of electromagnetic field from a proton. With the assumption of the dominance of the upper component of the wave function, we have obtained the similar equation to that of Samsonenko *et al.*. The binding energy is of the order of a few eV, which is an adequate value. On the contrary, the result calculated by Samsonenko *et al.* was terribly large value (> GeV). We shall calculate four-component equation in the next step.

Acknowledgement

The author appreciates Prof. Sasabe for making him known the paper of Samsonenko *et al.*

Appendix

(1)Equations used to derive eq. (3)

Setting an electromagnetic potential as,

$$\boldsymbol{A}(\boldsymbol{r}) = \frac{\mu_0}{4\pi}\boldsymbol{\mu} \times \frac{\boldsymbol{r}}{r^3},$$

$$cA^0(\boldsymbol{r}) = \frac{e}{4\pi\epsilon_0 r},$$

we have directly obtained the following equations.

$$\begin{aligned}\boldsymbol{\nabla}\cdot\boldsymbol{A} &= \boldsymbol{\nabla}\cdot\left[\frac{\mu_0}{4\pi}\boldsymbol{\mu}\times\frac{\boldsymbol{r}}{r^3}\right] \\ &= \boldsymbol{\nabla}\cdot\left[-\frac{\mu_0}{4\pi}\boldsymbol{\mu}\times\boldsymbol{\nabla}\left(\frac{1}{r}\right)\right] = 0\end{aligned}$$

$$\boldsymbol{\nabla}^2 = \frac{\partial^2}{\partial r^2} + \frac{2}{r}\frac{\partial}{\partial r} - \frac{\boldsymbol{L}^2}{r^2},$$

where, $\hbar\boldsymbol{L} = \boldsymbol{r}\times\boldsymbol{p}$.

$$(ceA_0)^2 = \left(\frac{e^2}{4\pi\epsilon_0 r}\right)^2,$$

$$e^2c^2\boldsymbol{A}^2 = \left(\frac{ce\mu_0}{4\pi}\right)^2\left\{\frac{(\boldsymbol{\mu}\cdot\boldsymbol{r})^2}{r^6} - \frac{\boldsymbol{\mu}^2}{r^4}\right\}$$

$$-2i\hbar c^2 q\boldsymbol{A}\cdot\boldsymbol{\nabla} = -\frac{2e\hbar}{4\pi\epsilon_0}\frac{\boldsymbol{\mu}\cdot\boldsymbol{L}}{r^3}$$

Furtheremore, substituting $\frac{e\hbar}{2m_p}\boldsymbol{\Sigma}$ for $\boldsymbol{\mu}$,

$$\boldsymbol{\mu}^2 = 3\left(\frac{e\hbar}{2m_p}\right)^2$$

$$(\boldsymbol{\mu}\cdot\boldsymbol{r})^2 = \left(\frac{e\hbar}{2m_p}\right)^2 r^2$$

$$\frac{(\boldsymbol{\mu}\cdot\boldsymbol{r})^2}{r^6} - \frac{\boldsymbol{\mu}^2}{r^4} = -2\left(\frac{e\hbar}{2m_p r^2}\right)^2$$

$$\begin{aligned}&\boldsymbol{\Sigma}\cdot\boldsymbol{B} \\ &= \boldsymbol{\Sigma}\cdot\frac{\mu_0}{4\pi}\left\{3\frac{(\boldsymbol{\mu}\cdot\boldsymbol{r})^2\boldsymbol{r}}{r^5} - \frac{\boldsymbol{\mu}}{r^3}\right\} \\ &= \frac{\mu_0}{4\pi}\frac{e\hbar}{2m_p}\left\{3\frac{(\boldsymbol{\Sigma}\cdot\boldsymbol{r})^2}{r^5} - \frac{\boldsymbol{\Sigma}^2}{r^3}\right\} \\ &= 0\end{aligned}$$

(2)Derivation of eq. (6)

Substituting eq. (1) with $n = 0$ for eq. (5), we obtain

$$b_1 = -2\alpha\kappa, \qquad \text{(A1)}$$

$$b_2 = \alpha(\alpha-1) - 2\kappa\theta, \qquad \text{(A2)}$$

$$b_3 = 2\theta(\alpha-1), \qquad \text{(A3)}$$

$$b_4 = \theta^2. \qquad \text{(A4)}$$

From eq. (A1)

$$\alpha = -\frac{b_1}{2\kappa}, \qquad \text{(A5)}$$

$$\alpha - 1 = -\frac{b_3}{2\theta}, \qquad \text{(A6)}$$

Substituting eqs. (A5) and (A6) into eq. (A3), we have

$$\kappa^2 + \frac{b_2}{2\theta}\kappa + \frac{b_1 b_3}{2\theta} = 0.$$

We then obtain eq. (6).

(3)Calculation of the binding energy

$$b_2^2 = \lambda^2(\pm\lambda+1)^2$$

$$k^2 = j(j+1) + \frac{1}{4} = \left(j+\frac{1}{2}\right)^2,$$

$$\lambda^2 = k^2 - \left(\frac{e^2}{4\pi\epsilon_0\hbar c}\right)^2 \approx \left(j+\frac{1}{2}\right)^2$$

$$\begin{aligned}2b_3b_1 &= -\left(\frac{e^2}{4\pi\epsilon_0}\right)^2\frac{4(k-1)E}{m_pc^4\hbar^2} \\ &\approx 1.41\times10^6(k-1)E \\ &\sim -1.1\times10^{-7}\times(k-1)\end{aligned}$$

Here, we set $E \sim mc^2 \approx 8.2\times10^{-14}$(J). Since we come to konw $|b_2| \sim 1$ and $k \sim 1$ from the above equations, $b_2^2 >> |2b_3b_1|$, then

$$\sqrt{b_2^2 - 2b_3b_1} \approx b_2 - \frac{b_3b_1}{b_2}$$

$$b_4 = 2\left(\frac{e^2}{8\pi\epsilon_0 m_pc^2}\right)^2 \approx 1.17\times10^{-36}.$$

We then have

$$\begin{aligned}&E^2 - (mc^2)^2 \\ &\approx -5.3\times10^{-17}\left\{b_2 \pm \left(b_2 - \frac{b_3b_1}{b_2}\right)\right\}\end{aligned}$$

Since the solution of the upper sign branch is not satisfied with the condition $E \sim mc^2$, we discard it. When $B \equiv E - mc^2$ is much smaller than E, $B \approx (E^2 - m^2c^4)/2E \approx 6\times10^{-19}$(J).

References

1) N. V. Samsonenko *et al.*, Phys. Lett. A, 220(1996)297-301.

2) S. Özçelik and M. Şimşek, Phys. Lett. A, 152(1991)145-150.

3) *e.g.*,C. Itzykson and J-B. Zuber, "Quantum Field Theory",McGrow-Hill 1985.

Numerical simulation of vortex pattern appeared on electrode surface after long term electrolysis of well annealed thick Pd rod in 0.1M LiOD

H. NUMATA: numata.h.aa@m.titech.ac.jp
Tokyo Institute of Technology, 2-12-1, O-okayama, Meguro Tokyo 152-8552 Japan
M. BAN: Masanobu_Ban@member.metro.jp
Tokyo Metropolitan Leather Technology Center, 3-13-14, Higashi Sumida, Sumida Tokyo 131-0042 Japan

Abstract: In N-cycle reaction model the hypothetical particles mass moves differently in two modes during the cold fusion experiment. The vortex pattern observed proves that the hypothetical particles mass flow coincidently through the electrode surface/electrolyte using LGCA numeric simulation method. Further the cascade model of vortices using usual CFD method is proposed for simulating the motion of these particles mass underneath the electrode surface.

Keyword: Computational fluid dynamics, Lattice gas cellular automata, Pd, Nuclear reaction cycle model, vortex, cold fusion

1 Introduction

During long-term electrolysis for well annealed thick Pd rod (9.0 mmϕ) in 0.1M LiOD vortex pattern was observed [1-2]. The morphology of the postelectrolysis electrodes revealed that there were appeared two long faults but without any cracking on the surface. This vortex pattern proved that the hypothetical particles mass flows coincidently through the electrode surface/electrolyte interface using Lattice Gas Cellular Automata method [3]. The original work of the modified cellular automata (numerical simulation) method had been first applied by Numata et al. to the study of cold fusion and the related phenomena.[8] Instead of the Quantum mechanical realization of cold fusion process, that work has captured microscopic mechanism: how the hypothetical particles mass having significant kinetic energy moved and has left the vortices on the sample surface. In modeling the given experimental system, the motion of particles (e.g., proton, electron or deuteron) was simulated as a 2D incompressive fluid composed of identical particles (correspond to fluid elements in the fluid), which time evolutions were calculated under the law of hydrodynamics: Navier-Stokes equation. Here, a fluid was composed of fluid elements.

Our interest has been focused on the mechanism of such peculiarities observed during cold fusion experiments. However there is still remained ambiguous with respect to the properties of moving particles and subsequently the modeling too.

In this paper recent progress of the phenomenological approach using computer simulation will be presented on the following points.

·PC performance for numerical simulation: speed of computation and change of platform from Windows to Linux
·Optimum B.C. for simulating vortex pattern emerging in the 2D incommpresive fluid flow
·Simulation model using CFD method of

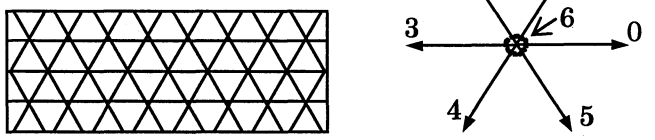

0-5 : moving particles having individual unit velocity
6 : rest particle

Fig.1 Triangular lattice with hexagonal symmetry and lattice gas particles having various velocities

Escaping D_2 from Deuterated Pd surface

2 Experimental

2.1 Basics of cellular automata

Lattice gas cellular automata are discrete models of fluids. A fluid is modeled by identical moving particles (essentially fluid elements consisting macroscopic fluid) set regularly in lattice whose time evolutions are represented by a discrete time step. This simulation method for fluids was proved to be identical to the kinetic equation: Navier-Stokes equation.

As cellular automata (hereafter CA or LGCA) are becoming helpful as simulation models in many physical phenomena (i.e., heat, wave and fluid); in particular, it offers a simple way to simulate the conventional fluid flows in complex geometry. In simulating 2D incompressive fluid lattice gas cellular automata are constructed on a simulating space where regular triangular lattices with unit link length are mapped and discredited on the whole. At each vertex, there are up to seven particle velocities involving rest particle. (Fig.1) In the simple lattice gases that are of interest for flow simulation, particles of unit mass move synchronously from one vertex of the lattice to a nearest neighbor vertex and collide with other particles arriving at that vertex (see example of Fig.2). This means there are as many different velocities as there are nearest neighbors to a

vertex. For a given velocity only one particle is allowed at a given vertex at a given time. This means that for a lattice gas with n different velocities $\{c_1, c_2, ..., c_n\}$ the state of each vertex is defined by n bits $\{s_1, s_2, ...,s_n\}$, each bit indicating whether a particle with corresponding velocity is present at the vertex or not. Often the absence of a particle with a given velocity is called ' a hall'.

For the simulation of Navier-Stoke flow it is essential that mass,

$$\Sigma i\, s_i,$$

and momentum,

$$\Sigma i\, s_i c_i,$$

are conserved in collisions. For a given velocity set, the algorithm is defined by the collision rules, i.e., the rules that specify for any given initial state (of incoming particles) what the final, after-collision, state of a vertex will be. Possible types of initial and final states for collisions in the FHP I fluid model [4] are shown in Fig.2. This model is relatively simple and it shows the correct macroscopic behavior. By changing these rules it is possible to vary the properties (e.g., the viscosity) of the fluid within a certain range.

2.2 Simulator performance

As an integrated CA simulator, we have made LGCA programs run on Windows and Linux platforms. On a usual PC (not CRAY supercomputers) users can configure their working area and edit their source code at the same time (not yet but being proceeded). Like most text editors, the text window of the simulator allows users to load a previously designed program, or input new rules into the editing area. As GUI for Windows we installed "GrWin graphics library developed for Windows OS" that can be obtained as the GrWin archives file from web site: http://sip.sci.shizuoka.ac.jp. The tutorial and documentations there would be helpful for installing several released versions. In order to run the program (programming languages: C, Fortran, Java et al.), users have to install the compiler in his machine. For example, the compiler can be downloaded from GNU web site for free.

First, the benchmark: Himeno benchmark was run under different ordinary PC speculations to evaluate the speed of the incompressive fluid analysis code. This code (calculation size fixed at S) is very simple to measure the speed in MFLOPS. (Table1) The test result shows that the larger the CPU clock, somewhat accompanied with the memory size, the faster the computational speed. In this experiment, CA simulation environment, Windows was at first implemented.

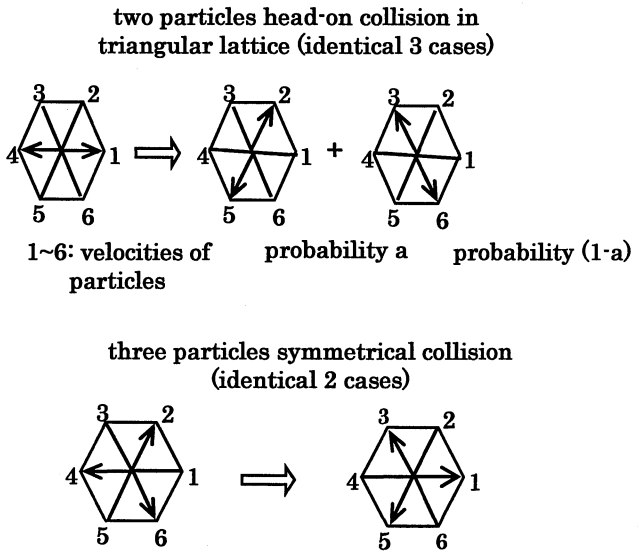

Fig.2 Collisions in 6-bits FHP I model

In Table 1 AMD implemented on Linux platform exhibits rank 5 (42.80 MFLOPS), that seems comparable, even though the PC speculation is relatively low. Since Linux is becoming convenient for movable and net environment, the further programming will be developed in Linux.

The implementation of CA simulation program: LGROTATE designed for Windows has been conducted; source code made using C will be also converted to Java because of its benefits: popular and complete graphical library for users. In the CA calculation each cell on the lattice is simultaneously renewed based on a single update rule, therefore, some approaches with parallel systems can be expected for more efficient computation. Until now we have made our CA simulator using only the soft wear from free sites, though next the compiler will be necessarily purchased from benders.

3. Results and discussion

3.1 Nuclear reaction cycle model

So far, endeavors have been exerted on understanding the individual phenomenon accompanied with cold fusion reaction, which are a complicated phenomenon as a whole. Under such an idea, by considering phenomena as an energy engine, N-cycle model[1-3] was proposed from a point of view of its continuous operation (4 reciprocating cycle). It consists of 4 sequential processes: in-taking and compression--triggering--reaction--scavenging, taking into account of the correspondence to long-term electrolysis of a thick rod Pd. (Fig.3) The following two key points are beneficially realized: (1) enhanced reproducibility of the experiments resides in continuation of the cycle (2) on systematic consideration the hindered factors might come to the surface.

Let the correspondence be examined with the model in question to the phenomena of the cold fusion experiment. In the absorption and compression processes of the reactants of the reaction (Fig.3), a barrier layer of deuterium migration by compression stress (also corresponds to the B side of the single-side electrolysis referred to the report [2, 5-6]) is formed as absorption in progress, resulting in formation of a vessel composed of the interior and blanket as the barrier layer. In the compression process, the interior appears to make expansion owing to the continued absorption, i.e., a part of the generated deuterium is contributed to further slow absorption. However, the compression pressure of

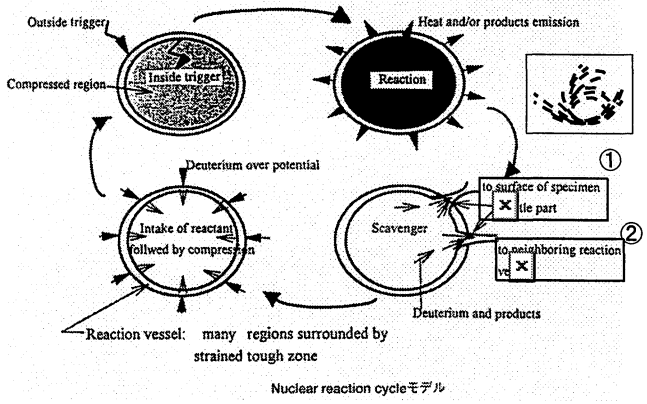

Fig.3 Schematic of nuclear reaction cycle model.

the blanket brings an increase of the internal pressure (in otherwise an increase in stress) due to a kind of enhanced pinch effect. In the reaction process a reaction should be caused by an external trigger that is applied to the inside (i.e., injection of high energy particles from the outside) or by an internal trigger. [2, 7] Very many holes concentrated on both the sides of the fault found in the experiment[2] were discharge ports of the reaction products in the process of scavenging. At this stage, discharge is made with the products of the reaction together with unreacting deuterium[7-8].

The resulting ca. 6% expansion confirmed during 1st run (also see the left of Fig. 4)[1-2, 5-6] suggests the occurrence of considerable internal pressure increase corresponding to the absorption/compression process of N-cycle model. Apart from the identification of the reaction vessels and emitted particles, the subsequent outflow of the hypothetical particle mass (once these particles were defined as charged particles, deuterium or reaction products) might occur toward 360° radial direction as the scavenger process of N-cycle model (also see the right of Fig.4). Such motions of the particles mass might be realized from the geometry of the reaction vessel formed during the absorption/compression process shown in the left. That is, in a long prism crystal absorbed reaction products or deuterium under high pressure coincidently spout out with sufficient energy where the motion of the flows are expressed as 'simulate flow' vectors normal to

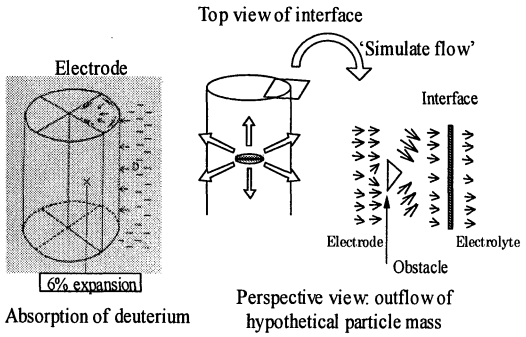

Fig.4 Absorption of deuterium and resultant outflow of hypothetical particles mass.

the electrode interface as shown in the right. Importantly all the flows synchronize with the occurrence of the reactions. It is known that nuclear reaction instantaneously occurs during which the hypothetical particles surrounding the site coincidently gain momentum converted by the energy of force evolved multiplied by time in an adiabatic sense. In addition obstacles might be embedded under beneath the surface due to inhomogeneity. Thus, N-cycle model predicts that the flows occur coincidently through the electrode/electrolyte interface (above shown in Fig.3 as the motion of reaction products and deuterium to neighboring vessels and/or surface of the electrode), however, phenomenological evidence has not yet been shown, which is substantiated next by a postelectrolysis Pd surface observation and numerical simulation of the fluid flow.

Simulation of vortex pattern

Ever since N-cycle model predicted the hypothetical particles mass explosively spouted out from the deuterated Pd surface after long-term deuterium evolution, it has been necessary that the vortex pattern on the Pd surface will be reproduced using computer simulation technique. In Scavenger process of Fig.3 there appeared alternative two mechanisms of the hypothetical particles mass motions. First, ① indicated in the figure togetherwith the insertion showing the vortex pattern means the fluid of these particles mass occasionally had left the locus on the Pd surface, named as vortex. Previous report[3] mainly concerned with the morphological identification of the vortex comparing between the vortex pattern observed and the form by 2D LGCA simulation. Further consideration had led to the physical view that the motion was fully understood by the influence of the electromagnetic interaction at the electrode/electrolyte interface. In this paper, a little more advanced 2D LGCA simulation result is presented. Figure 5 shows the flow behind a flat plate at t = 500 by using FHP III model in a rectangular domain, where stationary flow from left to right is given by the pressure difference of the inflow and outflow boundary regions. (refer

Ref. 9 for boundary conditions) This simulation in 2D space shows that the flow creates a vortex behind a flat plate as shown in the area enclosed with a circle. In this case the flat plate is considered as an obstacle for the first approximation. Although the coarser simulation is needed to fully describe the phenomenon, it is shown that a vortex exists in the downstream as shown in Fig.5. In Fig.5 the axis of the calculated vortex appears normal to this page, which is redrawn in 3D along the longitudinal of Pd rod, not normal to the electrolyte solution from the electrode surface. The LGCA simulation result showed that the vortex axis appeared along the longitudinal of the electrode due to the coincidental flow of the hypothetical particles mass (shown as arrows in Fig.4). However, by comparing the vortex pattern obtained by LGCA simulation and a post electrolysis Pd surface observation the vortex with the leaned axis along the electrode can only be acceptable to describe the motion of the hypothetical particles. (Fig.6) This means that the force might exert on the vortex motion of the particles during these traveling in either an electromagnetic or magneto-magnetic sense. The quantitative calculation with respect to the motion of the hypothetical particles mass at the interface was shown elsewhere.[9)]

Simulation model of vortex-thread dynamics

Secondary, ② indicated in Fig.3 means the hypothetical particles mass transfers continuously from a vessel to a neighboring one. There has been emerging doubt as to whether the vortex pattern on the electrode surface is representative motion of this particles mass. A reasonable inference led to that the vortex appeared is found incidentally, while the cascade of many vortices: vortex-thread moves underneath the electrode surface. This view might not be inconsistent with the irregularity of subsurface layer under an extraordinary treatment.

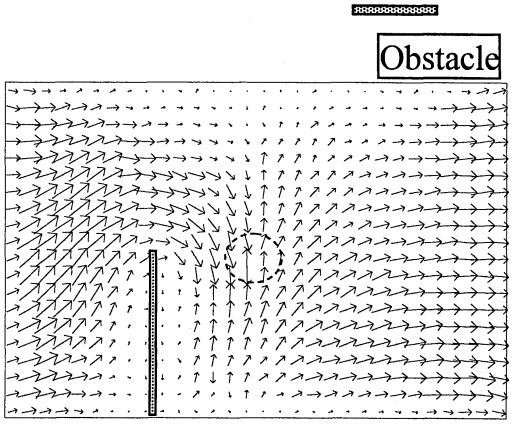

Fig.5 LGCA simulation result of vortex evolved behind flat plate on 512 x 460 grids at t=500.

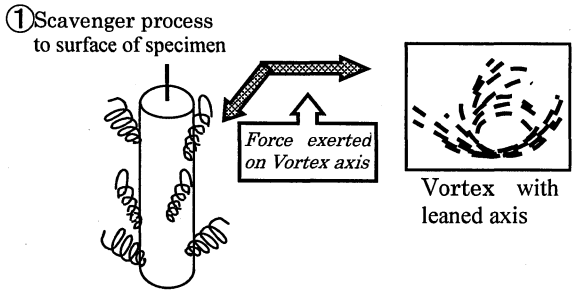

Fig.6 Schematics of vortex with leaned axis during Scavenger process; motion of hypothetical particles mass from vessel to surface.

In order to validate the cascade of vortex model, a vessel is at first defined where the turbulent flow of a vortex starts spout out by artificial triggering. In Fig.7 the possible two types of triggering: external and internal are shown togetherwith the vessel exhibiting turbulence therein. For simulating the dynamics of vortex-thread the characteristics of the fluid has been analyzed using 2D CFD (Computational fluid dynamics, e.g., FLUENT). Preliminary 2D CFD result shows that the vessel with free surface caused the turbulence and convection due to the gravitational and induced centrifugal forces involving the pressure (fluid velocity) variation with time. The model used to calculate using the vessel with free surface can be extended to 3D cascade vessel as shown in Fig.8. Next our approach is addressed to the followings,

- more useful CA simulator
- parameter survey fit for D_2 gas permeation
- physics of fluid, e.g., density, viscosity, velocity and superconductivity state around vortex-thread

3 Conclusion

We have designed the advanced LGCA simulation model for elucidating the mechanism of the evolution of the vortex during long-term deuterated Pd surface. N-cycle reaction model predicted that the hypothetical particles mass spouts out leaving the locus of the vortex pattern on the electrode surface. The analysis of the motion of these particles mass using LGCA shows the leaned axis of the vortex is attributed to the influence of magnetohydrodynamic interaction at the electrode/electrolyte interface. Further the cascade of the vortices: vortex-thread is proposed for the hydrodynamics of these particles mass motion using usual CFD simulator.

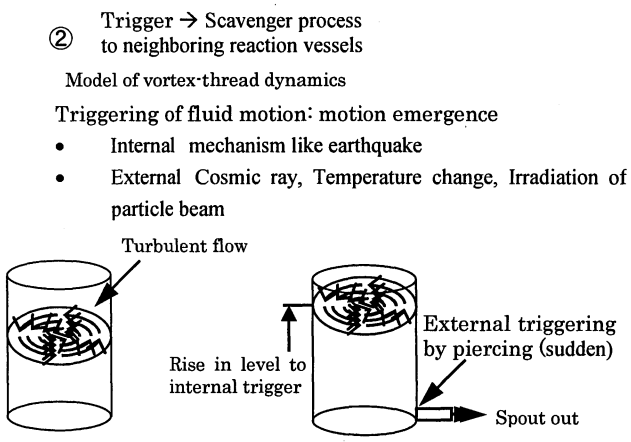

Fig.7 Schematics of a vessel (turbulent flow) and triggering

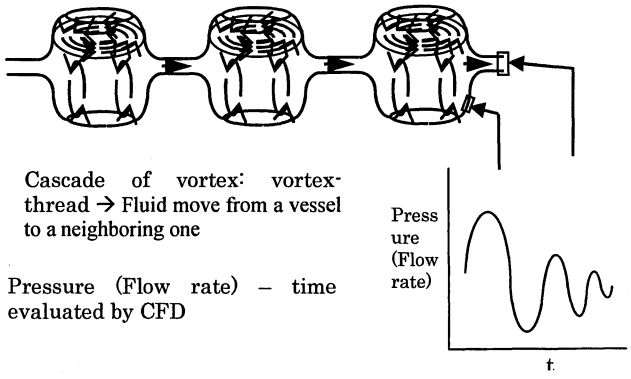

Fig.8 Cascade of vortex: vortex-thread model for CFD

Table 1 Comparison of measured speed at constant calculation size S(128x64x64)

Rank	Measured speed MFLOPS	CPU No	Manufacture	Model	CPU	Clock	Compiler	Option	Misc.info
	4705.05	1	NEC	SX-5	10GFLOPS	312.5 MHz		"Ch opt"	
1	224.44	2	-	Self-made PC	Intel Core2 Duo	1.86 GHz	gcc 3.4.2		WinXP Mem. 2GB
2	197.20	1	DELL	Notebook I2200	Intel PentiumM	1.6G Hz	gcc 3.4.2		WinXP Mem 504MB
3	191.77	1	DELL	Inspiron ME051	Intel CeleronM	1.5G Hz	gcc 3.4.2		WinXP Mem 504MB
4	82.29	1	DELL	OptiPlex743	Pentium IV	3GHz	gcc 3.4.2		WinXP Mem. 512MB
5	42.80	1	AMD	AMD Duron		707 MHz	gcc 3.3.6		Vine Linux 4.1 Mem. 124MB
6	34.41	1	IBM	Aptiva	Pentium IV	1.4G Hz	gcc 3.4.2		WinMe Mem. 1.5GB

References

1) H. Numata et al.: Proc. Conf. Science of Cold Fusion, Vol.33, pp.71, T.BRESSANI et al. eds., SIF, Bologna, Italy (1991)
2) R. Takagi et al.: Fusion Technol., **19** (1991)2135
3) H. Numata and M. Ban: Proc. ICCF12, Yokohama, pp.411-420 (2005)
4) D. d'Humières: Complex Syst. **1** (1987)599
5) H. Numata and I. Ohno: Fusion Technol., **38** (2000)206
6) H. Numata and I. Ohno: ICCF6, Toya Japan, vol.**1**, pp.213(1997)
7) H. Numata: in book "Cyber X" No.11, pp.37 (1999) Kougakusha.
8) A. Takahashi et al.: "Nuclear Reaction Study In Condensed Matter No.1", Chapter 4, pp.124, 1999 Kougakusha.
9) H. Numata and M. Ban: Proc. JCF6, pp.32 (2005)

Evolution of Co-operative tunnel resonance in Canonical Ensemble system

M. BAN, Tokyo Metropolitan Leather Technology Center: Masanobu_Ban@member.metro.tokyo.jp
H. NUMATA, Tokyo Institute of Technology : numata.h.aa@m.titech.ac.jp

Abstract: The Nosé-Hoover method for temperature const. molecular dynamics (MD) of many-particle was investigated by Watanabe et al. It is shown that the dynamic behavior of the variables: random or periodic is dependent on the added thermostats' parameter. If the total system exhibits Torus in phase-space diagram, this is accomplished by loss of one/more degree of freedom. In the cold fusion experiments this state appears accompanied by the stimulus during which the permeation of the relevant particles is characterized as "tunnel resonance" proposed by Ban.

Keyword: tunnel resonance, cold fusion, ergodic, many–particle, degree of freedom, D permeation

1 Introduction

In the cold fusion experiments heat generation and/or emissions of neutron or charged particles have been observed by continuing a state where hydrogen isotopes are strongly absorbed in a Pd electrode by electrolysis or electrical discharge in gaseous plasmas. First experiment of the deuterated (also hydrated) Pd/Au heterostructures in a vacuum chamber elucidated that excess heat evolved coincidently to the current injection was attributed to the accelerated out-gas of H_2 (D_2) through the matrix specially stressed by the induced sample deformation.[1] In the current injection device, the direct current: flow of electron was transferred between the top of W needle and the outer most Pd layer during which the flow of not only electron but hydrogen (D) atoms occurred forming a fluid like the next transmutation experiment. The nuclear transformation has also been studied by D_2 gas permeation method through Pd/CaO multi-layered Pd film.[2] In the transmutation experiment D_2 gas permeation takes place by the controlled pressure difference, and subsequently D^+ permeates the multi-layered structure.[2]

In the cold fusion experiments, above indicated as representative examples, D_2 gas permeation takes place by either the controlled pressure difference or the autocatalytic process induced by stress change.

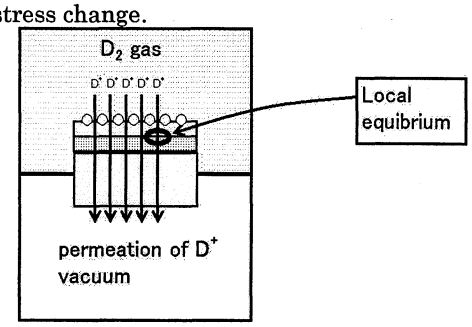

Fig.1 Local equibrium at permeation of D^+

Figure 1 shows a schematic of the snapshot of the motion of the particles concerned with those transfers during the extraordinary cold fusion phenomena occurred. Although there have been still unsettled moving particles and the matrixes, it is postulated that the particles might be electron and deuteron (hydrogen in an aqueous solution). We consider ionized entities: deuteron (hydronium ion) as these particles. For simplicity let us consider the charge of these particles in the next report. For the perturbation, which moves these particles, the physical origin can be easily understood as mainly chemical potential and a small amount of electric field. The chemical potential difference there gives rise to the irreversible process, e.g., diffusion (viscosity and thermal conductivity under the other perturbations), the usual time constant to attain the entire homogeneity: hydrodynamic relaxation time is taken as the order of seconds or minutes. While under the limited areas: a few mean free paths wide the gradients of these quantities are so small that the relaxation time is in the order of 10^{-9} s, then we expect that in such a small volume local near-equilibrium can be attained. We take a limited volume into consideration as is shown in Fig.1 provided local equilibrium. Based on such local equilibrium the motion of those particles (see Fig.1) can be envisaged as the canonical ensemble further discussed later.

Apart from statistical mechanics, the kinetic equation, e.g., Boltzmann equation has been extensively studied in the field of high temperature plasmas. Bosonized condensates and coherent reaction of many-particle in lattices are modeled to elucidate the dynamics of D permeation through the multiple barrier. [3-4]

Ban had presented new theory that could be helpful in elucidating cold fusion. [5-6] These reports have shown that matter wave (i.e., deuteron/ hydronium ion and electron) behaves like a wave during which hypothetical periodic

lattice emerges forming the Toda's infinite lattice.[7] In addition, the process of self-organization makes the structure of the arrayed lattices where the molecular motion was described by "tunnel resonance" process as in usual electronic devices. Recently, the idea of similar tunnel resonance process is introduced to analyze the deuterium transportation through deuterated Pd thin film.[8]

From a general point of view, quantum physics can be considered essentially the principle method to approach the cold fusion theory. But statistical mechanics is also beneficial for giving a simple mechanism with so complicated phenomena involving many kinds of particle motions.

In this paper statistical mechanics has been applied to many-particle motion that can be evolved with cold fusion reaction[1-2] considering the concept reported by Watanabe et al.[9-10] The numerical simulation: the Nosé-Hoover method has shown that the total system in equilibrium exhibits loss of ergodicity, that is characterized as torus isoenergitic trajectory in phase-space diagram. Given total system is composed of the original system thermally equilibrated with a thermostat. However, the total system takes one or more thermostats added resulting the ergodicity which isoenergitic trajectory homogeneously occupies the volume in phase-space diagram. Thus the Nosé-Hoover method and the other extended ones showed two different dynamic behaviors, associated with the time evolutions of the heatbaths variable. Since the above mentioned matrixes subjected to the D^+ (H^+)and electron permeation (see Fig.1) can be simulated as the total system, the transition from one to another states with and without ergodicity can be highly probable. Here we will focus on the system behavior showing the transition, where the motion of many-particles is thermally equilibrated with the atmosphere and then suddenly changed to the state of coherent wave: tunnel resonance process.

2 Background of Analysis

2.1 Canonical movement and tunnel resonance

The motion of many-particle is now discussed from the standpoint of statistical mechanics; in particular the motion is described as "random or periodic". The energy of the given system (for total system if it is composed of many subsystems) is conserved, i.e., an isolated system. The necessary condition "In equilibrium" can be required, either for a single system or a unified one having many subsystems. One of the systems obeying such conditions is coerced into the ergodic behavior; it makes their long-time-averaged behavior independent of initial conditions. The example of this motion: time evolution of one particle configuration is characterized as Brownian motion and that of phase-space diagram as chaotic motion. Unlike such known motions, the system without the ergodicity shows the periodic configuration change, and thus the time evolution in phase-space diagram makes a Torus which volume is vacant. (schematic diagram is seen in Fig.2)

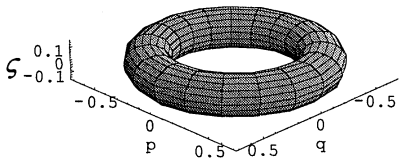

Fig.2 Isoenergitic 3D trajectory of harmonic oscillator (pendulum motion) in phase-space diagram

Therefore, the Hamiltonian of the system has maximum and minimum values. One example of the latter case: without ergodicity is consistent with "tunnel resonance" that evaluated by Ban.[5-6]

It is highly probable that the cold fusion reaction is related with the motion of electron and hydronium ion (D^+). In the followings the miscellaneous underlying conditions in the emergence of cold fusion (i.e., the above mentioned two experiments) accompanied by "tunnel resonance" will be elucidated in the aspect of statistical mechanics of many-particle.

2.2 Dynamics of T const. MD: Nosé-Hoover and extended Nosé-Hoover methods (from Watanabe's reports [9-10])

Before following discussion we permits that the experimental systems concerned are in equilibrium with the atmosphere, i.e., conserved at constant temperature, and then the interesting results drawn by Watanabe et al. can be applicable. Here the atmosphere means the matrix surrounding a small volume, which is in local equilibrium. The Nosé-Hoover method has been developed for the system conserving constant temperature with MD simulation when it is ergodic. [11] To achieve the canonical ensemble this method takes samples, e.g., many-particle at a constant-temperature, equilibrated with the Nosé-Hoover thermostat, and thus the equations of motion for the total system equilibrated with Nosé-Hoover thermostat are

$$\begin{cases} \dot{p} = -\dfrac{\partial H}{\partial q} - p\zeta, \\ \dot{q} = \dfrac{\partial H}{\partial p}, \\ \dot{\zeta} = \tau^{-2}\left(\dfrac{K}{K_0} - 1\right), \\ \dot{\eta} = \zeta \end{cases} \quad (1)$$

where ζ and η are additional variables expressing the Nosé-Hoover thermostat, and K, K_0, and τ are the kinetic energy, the aimed temperature, and the relaxation time of the thermostat, respectively.

Then, the pseudo-Hamiltonian H' of the total system (= original + additional thermostats) is given as

$$H' = H + K_0(\tau\zeta^2 + 2\eta) \quad (2)$$

where H is the original Hamiltonian. While the system with the Nosé-Hoover thermostat does not have the canonical form. If a quantity H' is conserved with the original Hamiltonian H (namely the energy of the system without the thermostat can fluctuate with the Boltzmann weight $\exp(-\beta H)$), the system will achieve the canonical ensemble.

Figure 2 shows isoenergitic phase-space diagram (p,q,ς) of the total system (the original system: harmonic oscillator) with the Nosé-Hoover thermostat (one degree of freedom). While the harmonic oscillator exhibits time evolution of fluctuation weighted by Boltzmann distribution, the given system has the minimum and maximum energies.

Apparently, it is not ergodic since the isoenergitic trajectory did not cover the whole phase-space and rooted only on the surface of Torus.

On the other hand, Kusnezov et al. [12] proposed the kinetic-moments method to improve the ergodicity introducing the extended Nosé-Hoover method. As shown above the Nosé-Hoover method with the Nosé-Hoover thermostat easily has seen lost the ergodicity, because the added degree of freedom makes the system quickly oscillate accompanied with much slower oscillation. This method and also Nosé-Hoover chain one [12-13] take one or more thermostats added resulting the ergodicity because the added degrees of freedom emerges the chaotic time evolution of the variables. The key factors distinguish between the systems with and without ergodicity are attributable to the additional thermostat showing the chaotic

time evolution. Here, the examined systems as the original one were the harmonic-oscillator with one degree of freedom and the other oscillating system ($H_0 = p^2/2 + q^{2k}/2k$ (k = 1, 2,)).

3 Discussion

3.1 Ergodicity of the systems with Nosé-Hoover type thermostat

Aforementioned, Watanabe reported that the Nosé-Hoover method loses its ergodicity where the original system (mostly Hamiltonian) is equilibrated with a thermostat i.e., adding one degree of freedom. Thus, the total system once characterized as lost its ergodicity by adding one degree of freedom but doesn't lose by adding two degrees of freedom. In contrast to this process the total system assuming some degrees of freedom (i.e., already has lost ergodicity) exhibits its ergodicity simultaneously with a loss of more than one degree of freedom. It is schematically tabulated in terms of ergodicity, corresponding method and nominal change of degree of freedom, accompanied with isoenergitic trajectory in phase-space diagram. (Table 1)

Table 1 Nominal change of degree of freedom, ergodicity and trajectory of system

Method	system;		Nominal change of degree of freedom	Ergo-dicity	Trajec-tory
	Hamil tonian	thermo stats			
N-H	1	1	-	nil	Torus
Kinetic moments,	1	1+1	1	exist	un-settled
N-H chain method	1	1+ many	+many	exist	un-settled
(N-H=Nosé-Hoover method)					

3.2 Emergence of cold fusion reaction

In this chapter let us show how the emergence of the cold fusion reaction is achieved by a sudden change of the following two states. At first we consider two states. During the cold fusion experiments (i.e., electrolysis, discharge in a vacuum chamber or gas permeation), we assume one state; in the early stage the sample matrix is substantially subjected to absorption of D (H) atoms, and then the permeation of these particles occur steadily. In this stage there appears no evolution of neutron and/or excess heat or transmutation. That state is characterized as the original system with two/more thermostats, i.e., resulting plus 1 or many degrees of freedom addition to that equilibrated with a thermostat. (see Table 1) Following the above manner of statement another state is expressed as the original system (mostly Hamiltonian) equilibrated with a thermostat i.e., adding one degree of freedom.

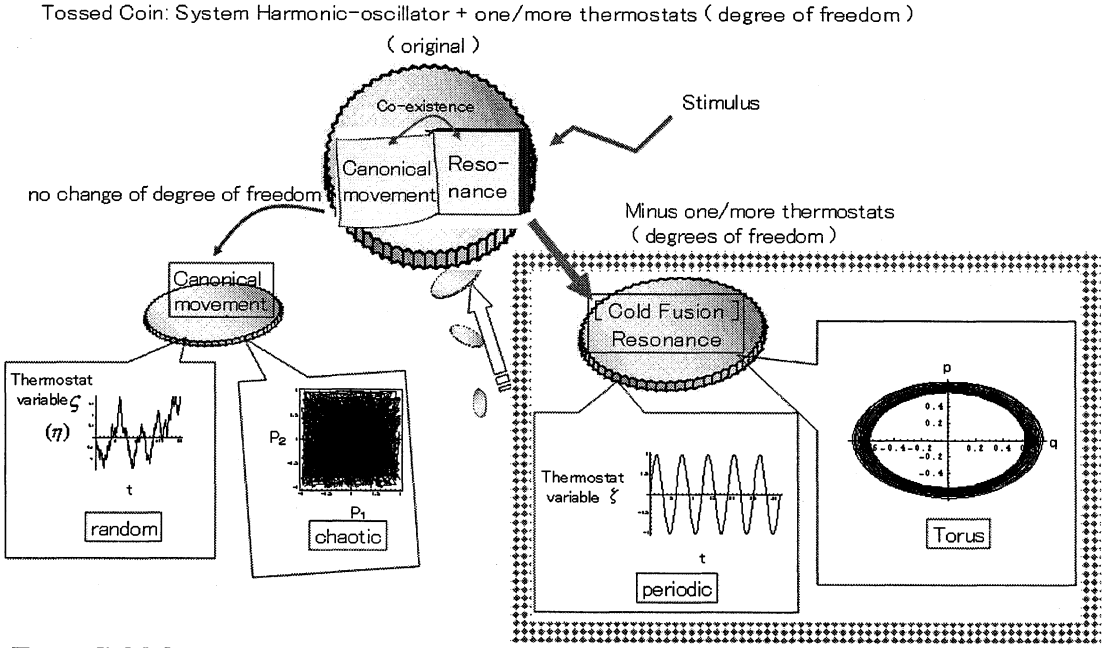

Fig.3 Cold fusion emergence in the system: original + one/more thermostats

Here we make another assumption that except only an isolated system there co-exist the random motion and somewhat ordered one originated from the system's fluctuation. According to Watanabe's result[9-10] the former system exhibits Brownian motion with chaotic time evolution in phase-space diagram. While the latter shows some degree of ordered motion, and thus the time evolution in phase-space diagram makes a Torus. (schematic diagram is shown in Fig.2) The latter case is exemplified as "tunnel resonance" that evaluated by Ban.[5-6]

By the way we define the next stage as the cold fusion phenomena appeared. Our expectation to elucidate the cold fusion mechanism is that the transition between two stages occurs by a strong stimulus. In addition in the early stage the system is configured by the particles in chaotic motion and in the next stage it is by the coherent motion i.e., tunnel resonance state, both of which are equilibrated with one/more thermostats. These two opposite states in co-existence and the sudden change of stages are illustrated in Fig.3 as a performance of the coin toss. It is seen that the state of the cold fusion reaction appeared in the next stage is characterized as Torus in phase-space diagram, which corresponds to the particle motion in tunnel resonance state.

From the above consideration one condition necessary to the cold fusion reaction is evaluated as one or more degree loss of freedom according to Watanabe' s result[9-10].

Next we figure out the necessary conditions for the system exhibiting change from the usual defined by the Hamiltonian + two/more thermostats to that of the Hamiltonian + one thermostat.

3.3 Cold fusion and tunnel resonance

Let the correspondence be examined with Watanabe's predictions from a statistical mechanistics viewpoint. We again consider the experimental conditions; the permeation of electron and hydronium ion (deuteron) are steadily conducted under a controlled driving force. Due to the stimulus or irregular disturbance, the tunnel resonance occurs with the frequency of $2\pi n$, together with a loss of one/more degree of freedom: e.g., in coherent state or at lower temperatures.

Watanabe et al. analyzed the Nosé-Hoover method as canonical ensemble where the total system is composed of the original and subsystems both under a thermal equilibrium. The Hamiltonian of the total system is

$$H(\Gamma) = H_0(\Gamma_0) + H_\perp(\Gamma_\perp) \qquad (3)$$

where $H_0(\Gamma_0)$ and $H_\perp$ are the Hamiltonian of the original, i.e., the Boltzmann distribution and the rest system. (also see Fig.4)

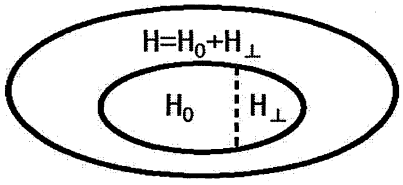

Fig. 4 Schematic diagram of Nosé-Hoover method; the original system thermally equilibrate with given thermostat.

Since the change of above canonical movement/resonance state depends on the nominal loss/gain degree of freedom, which is attributable to: how the total system oscillates under an influence of the equilibrate subsystems.

Since the system in tunnel resonance having the subsystem oscillating quickly, there happens for the rest system changing the state of oscillation resulting loss of degree of freedom.

4 Conclusion

Watanabe et al. elucidated that the Nosé-Hoover method for temperature const. MD of many-particle loses the ergodicity, which is dependent on additional thermostats oscillating with the given frequency. Based on their result cold fusion emerges accompanied by degree loss of freedom of the system which state is characterized as "tunnel resonance" proposed by Ban.

Acknowledgements

We thank JCF for giving the opportunity to present our paper.

Appendix

Theoretical consideration

Given momentum p and space position q in many particles system, a state variable is expressed as

$$\Gamma = (p_1, q_1, \ldots\ldots)$$

If we assume that the given state of the Boltzmann distribution Γ_0 is embedded into the stateΓ assuming the other state$\Gamma_\perp$, that is, Γ_0 is a state variable of a partial system in that of Γ

$$\Gamma = \Gamma_0 \otimes \Gamma_\perp$$

The energy function $H(\Gamma)$ of the stateΓ is shown using Hamiltonian of the Boltzmann distribution $H_0(\Gamma_0)$

$$H(\Gamma) = H_0(\Gamma_0) + H_\perp(\Gamma_\perp)$$

Here the distribution function $f(\Gamma)$ is expressed as the products applying the method using separation of variables

$$f(\Gamma) = f_0(\Gamma_0) f_\perp(\Gamma_\perp)$$

where $f_0(\Gamma_0) = Z_0^{-1}\exp(-\beta H_0)$ is given and β is temperature.

We finally obtain $H_\perp(\zeta)$ as the solution of the above Eq.

$$H_\perp(\zeta) = \tau^2\zeta^2/2$$

whereτ is an arbitrary parameter that shows relaxation time.

Thus, Nosé-Hoover equation obtained represents the particles motion.

On the other hand, the characteristic of the equation is drawn as

$$H_0 \cdot (m+1)\ln H_0 \leqq C$$

where m is an integer and C is the constant.

The above inequality implies that an increase of degree of freedom, i.e., the addition of variable ζ loses the ergodicity of the Boltzmann distribution.

Actually the H_0 of harmonic oscillator is given

$$H_0 = p^2/2 + q^{2k}/2k \quad (k = 1, 2, \ldots)$$

References:

1 E. Yamaguchi and H. Sugiura: Excess Heat and Nuclear Products from Pd:/Au Heterostructures by the 'In-vacuo' Method, Proc. ICCF7, pp.420-424, Vancouver, 1998

2 Y. Iwamura, M. Sakano and T. Itoh: Jpn. J. Appl. Phys. 41, 4642, 2002

3 A. Takahashi: Proc. ICCF10, Cambridge, 2003

4 S. Chubb: Proc. ICCF10, Cambridge, 2003

5 M. Ban: COMPOSITION OF 1/F AMPLITUDES ELECTRON WAVE AND A WORK OF ONE DIMENSION OF LATTICE, Proc. JCF4, pp.90-94, Morioka, 2002

6 M. Ban: Proc. ICCF12, pp.451-455, Yokohama, 2005

7 M. Toda: JPSJ, 22, 431, 1967, ibidem: 23, 501, 1967

8 Li, X.Z., et al.: Proc.ICCF12, pp.482-493,Yokohama, 2005

9 H. Watanabe and H. Kobayashi: Butsuri (Nihonbutsurigakkaisi), 62, pp.785-788, 2007, in Japanese

10 H. Watanabe and H. Kobayashi, Phys. Rev. E 75 040102(R), 2007

11 S. Nosé: Mol.Phys., 52, 255, 1984; W.G.Hoover: Phys. Rev. A, 31, 1695, 1985

12 D. Kusnezov, A. Bulgac and W. Bauer: Ann. Phys. (N.Y.), 204, 155, 1990

13 G.J. Martyna, M.L. Klein and M. Tuckerman: J. Chem. Phys., 97, 2635, 1992

Questions raised by a reviewer on this paper

1. Validity of the assumption "**Although there have been still unsettled moving particles and the matrixes, it is postulated that the particles might be electron and deuterium**" (p.1 right column) for cold fusion system (e.g. PdD_x). It is considered that electrons enter into a conduction band and deuterons move through interstitials sites, in general.

2. Validity of the application of MD, cultivated to treat dynamics of a microcanonical or canonical ensemble, to cold fusion system, which is essentially non-equilibrium, assuming "**we expect that in such a small volume local near-equilibrium can be attained.**" (p.1 right column)

The Cold Fusion Phenomenon as a Complexity (2) – Parameters Characterizing the System where occurs the CFP –

Hideo Kozima,
Cold Fusion Research Laboratory,
421-1202, Yatsu, Aoi, Shizuoka 421-1202, Japan

Abstract

The cold fusion phenomenon (CFP) was investigated from the point of view developed in nonlinear dynamics. It was shown that the recursion relations are applicable to events in the CFP to explain their characteristics using the density of the trapped neutrons in the TNCF model as a parameter of the recursion function.

1. Introduction

The cold fusion phenomenon (CFP) contains events related with nuclear reactions accompanying excess energy production. In these events, we have determined experimentally parameters governing the occurrence of the CFP such as the loading ratio η (=D/Pd, H/Ni, etc.), temperature T, current density i to the cathode in electrolytic and discharge systems, etc. The events also show a characteristic of the recursion relations

$$x_{n+1} = \lambda f(x_n), \qquad (1)$$

well investigated in nonlinear dynamics [1].

It is interesting to notice that a large class of recursion relations (1) exhibiting infinite bifurcation possesses a rich quantitative structure essentially independent of the recursion functions $f(x)$ when they have a unique differentiable maximum $\underline{x}$. With $f(\underline{x}) - f(x) \sim |x - \underline{x}|^z$ (for $|x - \underline{x}|$ sufficiently small) and $z > 1$, the universal details depend only upon z.

In particular, the local structure of high-order stability sets is shown to approach universality rescaling in successive bifurcations, asymptotically by the ratio α (α = 2.5029078750957... for $z = 2$) [1].

We investigate the CFP from the point of view described by the recursion relations (1).

2. Structure of the Population (Density) Equation

The recursion equations (1) provide a description for a variety of problems. For example, a discrete population (density) satisfies the formula

$$p_{n+1} = f(p_n),$$

determining the population (density) at one time in terms of its previous value [1].

The events we observe in the CFP seem to belong this type of quantities obeying the relations (1) as we have partly shown in recent works [2 – 5]. We confine our investigation in this paper to the discrete population (density) relations and make the result show its validity.

If the population (or density) referred to is such that of a dilute group of organisms (or

agents e.g. density of trapped neutrons n_n in the CFP), then the population (density) equations

$$p_{n+1} = b\, p_n \qquad (2)$$

accurately describe the population (density) growth with a growth rate b so long as it remains dilute, with the solution

$$p_n = p_0\, b^n. \qquad (3)$$

For a given species of organism (agent) in a fixed milieu, b is a constant – the static birth rate for the configuration.

As the population grows, the dilute approximation will ultimately fail: sufficient organisms (agents) are present and mutually interfere. At this point, the next value of the population (density) will be determined by a dynamic or effective birth rate b_{eff}:

$$p_{n+1} = b_{eff}\, p_n \qquad (4)$$

with $b_{eff} < b$. Clearly, b_{eff} is a function of p, with

$$\lim_{p\to 0} b_{eff}(p) = b, \qquad (5)$$

the only model-independent quantitative feature of b_{eff}. It is also clear that

$$\lim_{p\to\infty} b_{eff}(p) = 0. \qquad (6)$$

Accordingly, the simplest form of b_{eff} to reproduce the qualitative dynamics of such a population (density) should resemble Fig. 1, where $b_{eff}(0) = b$ is an adjustable parameter.

A simple specific form of $b_{eff}(p)$ is written with a constant a;

$$b_{eff}(p) = b - ap, \qquad (7)$$

so that

$$p_{n+1} = b_{eff}\, p_n - a\, p_n^2.$$

By defining $p_n \equiv (b/a)x_n$, we obtain the standard form of logistic difference equations (l.d.e.)

$$x_{n+1} = b x_n (1 - x_n). \qquad (8)$$

In (8), the adjustable parameter b is purely multiplicative. With a different choice of b_{eff}, x_{n+1} would not in general depend upon b in so simple a fashion [1]. Nevertheless, the internal b dependence may be (and often is) sufficiently mild in comparison to the multiplicative dependence that at least for qualitative purposes the internal dependence can be ignored. Thus, with $f(p) = p\, b_{eff}(p)$, any function like Fig. 1,

$$p_{n+1} = bf(p_n) \qquad (9)$$

is compatible and representative of the population (density) discussed [1].

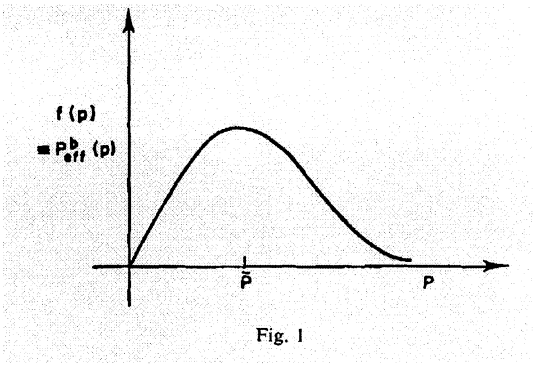

Fig. 1

Fig. 1. Dependence of $f(p) = p\, b_{eff}(p)$ on p after Feigenbaum [1].

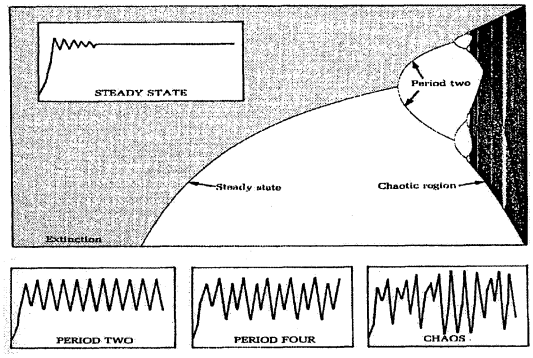

Fig. 2. Bifurcation diagram to show period-doubling and chaos (From "Chaos" by J. Gleick [6]. p.71). The main figure depicts x_∞ on the ordinate (x_∞ is x_n at $n = \infty$) vs. the parameter λ on the abscissa of the logistic difference equation, i.e. l.d.e., $x_{n+1} = \lambda\, x_n(1 - x_n)$ $(0 < x_0 < 1)$.

The inserted figures, a) Steady state, b) Period two, c) period four, and d) chaos, depict variations of x_n with increase of suffix n (temporal variation if n increases with time) for four values of λ; a) $1 < \lambda < 3$, b) $3 < \lambda < 3.4$, c) $\lambda \simeq 3.7$, d) $4 < \lambda$. The region a), b) and d) correspond to "Steady state", "Period two" and "Chaotic region" in the main figure, respectively.

To investigate the structure of the population (density) equation (8), we study the l.d.e. after J. Gleick [6]. Figure 2 is a bifurcation diagram showing period-doubling and chaos [6, p. 71].

3. Parameters of the l.d.e. in the CFP

We investigate complexity of the cold fusion phenomenon (CFP) assuming that the density (or population) of agents for the CFP obey the recursion equations (1) or rather the simplified equation, the l.d.e. (8).

In accordance with the quantum mechanical explanation of mechanisms of the CFP, we may take the trapped neutron (the quasi-free neutron in the CF materials) as an agent for the CFP and its density n_n as the variable x_n in the l.d.e.

The number of reactions N_{nX} (per unit time) between trapped thermal neutrons and a nucleus ${}^{A}_{Z}X$ is assumed to be calculated by the same formula as the usual collision process in a vacuum [3]:

$$N_{nX} = 0.35\, n_n\, v_n\, n_X V \sigma_{nX}, \qquad (10)$$

where $0.35\, n_n\, v_n$ is the flow density of the trapped thermal neutrons per unit area and time, n_X is the density of the nucleus ${}^{A}_{Z}X$, V is the volume where the reaction occurs, σ_{nX} is the cross section of the reaction.

Then, the equations (8) applied to the CFP describes evolution of the adjustable parameter n_n (density of the trapped neutrons at an active region) due to variations of the CF material accompanied with such nuclear reactions in CF materials as

$n + p = d$ (1.33 keV) + φ's (2.22 MeV) (11) $n + d = t$ (6.98 keV) + φ's (6.25 MeV), (12) $t + d = {}^{4}_{2}\mathrm{He}$ (3.5 MeV) + n (14.1 MeV), (13)

where φ's mean phonons generated at the reaction in the CF material instead of a photon in the case of these reactions occurred in the free space.

The evolutions of nuclear products and/or excess energy due to $n - p$ and $n - d$ reactions are proportional to n_n and Eq. (10) is rewritten as follows;

$$N_{np} = 0.35\, n_n\, v_n n_p V \sigma_{np} \tau, \qquad (14)$$

$$N_{nd} = 0.35\, n_n\, v_n n_d V \sigma_{nd} \tau, \qquad (15)$$

where n_p and n_d are the densities of protons and deuterons, $\sigma_{np} = 3.32 \times 10^{-1}$ b and $\sigma_{nd} = 5.5 \times 10^{-4}$ b (1 b = 10^{-24} cm^2) are the cross sections of the $n - p$ and $n - d$ reactions for a thermal neutron, respectively.

There are several data sets which were obtained in systems with temperature variation. In these cases, such variables as n_n, v_n, σ_{nX} (σ_{np}, σ_{nd}) in Eqs. (10), (14) and (15) are temperature dependent and therefore the number of reactions N depends on the temperature T;

$$N = N(T). \qquad (16)$$

Furthermore, it should be noticed that the number N expressed as Eq. (16) shows also a temporal evolution of the nuclear products (including also the excess heat) when the parameter n_n depends on the time variable τ

even if other quantities are not;

$$N(\tau) = Cn_n(\tau), \qquad (17)$$

where C is a constant independent of time.

The parameter b in the l.d.e. (8) specifies evolution of the population (or density) x_n as we see in Fig. 2. The larger the constant (parameter) b is, the more complex the evolution (and bifurcation) becomes.

In the CFP, the parameters governing the events are experimentally figured out as follows; The most evident parameter is the loading ratio η of hydrogen isotopes to host metals (η = D/Pd, D/Ti, H/Ni, etc.). The other less definitely specified parameters are the temperature T, current density i to the cathode, homogeneity of composition in the active region of alloys (transition-metal hydrides and deuterides), a distance from equilibrium state, density of trapped neutrons n_n, etc.

Leaving comprehensive discussion about the parameters governing the CFP to the next paper, we show here only an example obtained by De Ninno et al. [7]. In their experiment, a titanium (Ti) sample in the shape of shavings was put in contact with a deuterium (D_2) gas with pressures up to 5 MPa at varying temperatures between 77K and room temperature. The samples were, thus, put in a dynamical condition for the process of absorption/desorption of deuterium in titanium.

Using a BF_3 neutron counter with high sensitivity (efficiency $\simeq 5 \times 10^{-5}$), they could observe neutron emissions in two runs up to 320 counts/10 min under a low background condition with an average value of 2.3 counts/10 min The results were shown in Figs. 3 and 4.

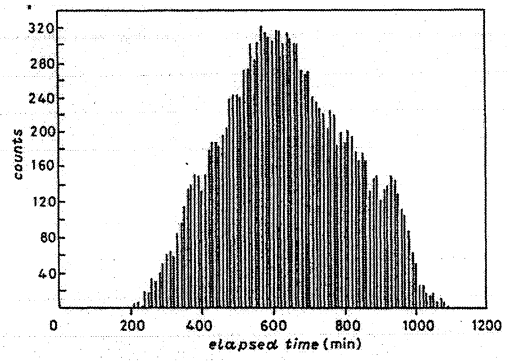

Fig. 3. Diagram showing the time evolution of the neutron emission from TiD_x sample during the run A (April 15-16, 1989). The values indicated are integral counts over periods of ten minutes (Fig.3 of [7]).

Figure 3 is a diagram showing the temporal evolution of the neutron emission during the run *A* (April 15 – 16, 1989). In this run, the system was put in the desorption phase; the deuterium gas was evacuated and the liquid-nitrogen Dewar was removed from the initial situation where deuterium pressure was 5 MPa at 77 K. Thus, the temperature of the system increases from 77 K at time 0 to room temperature about time 61 h accompanying desorption (and therefore decrease of the loading ratio η = D/Ti). From our point of view, this process can be interpreted as an increase of the parameter n_n (density of trapped neutrons) with increase of temperature despite of the decrease of η at first and then a decrease of n_n due to the decrease of η.

This variation of the parameter n is qualitatively described in Fig. 1 simulating an envelope of Fig. 3. This behavior suggests that neutron emission in this case is determined by a

nuclear reaction such as Eq. (12) (followed by Eq. (13) to emit neutrons) where the reaction rate is proportional to the density n_n of the trapped neutrons assumed in the TNCF model.

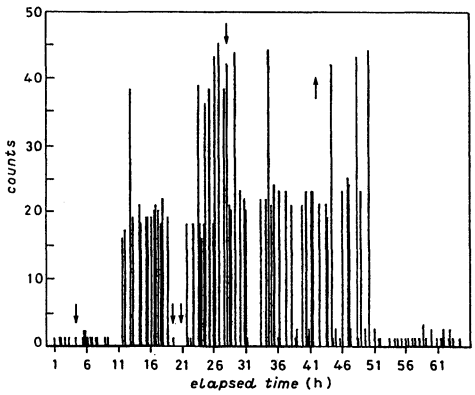

Fig. 4. Diagram showing the time evolution of the neutron emission counts (ordinate) during the run B (7-10 April, 1989) by De Ninno et al. [7]. The values indicated are integral counts over periods of 10 minutes.

Fig. 4 is a diagram showing the temporal evolution the neutron emission during the run *B* (April 7 – 10, 1989). In this run, D_2 gas was admitted to the cell in steps of increasing pressure after degassing the Ti sample. A pressure around 5 MPa was reached and then the temperature was lowered to 77 K by immersing the cell in a Dewar full of liquid nitrogen. At this point, the system was left to itself, at constant pressure, with the aim of obtaining changes of temperature both in time and space while the level of liquid nitrogen in the Dewar was going down.

In Fig. 4, the down directed arrows indicate liquid-nitrogen fillings. The up-directed arrow shows the time when the Dewar was taken away and the system was thus allowed to rise to room temperature. Thus, the abscissa of this diagram is not necessarily represents temperature of the system as in the case of Fig. 3.

We notice a characteristic of time pattern of neutron emission appeared in Fig. 4 that there are two levels of emission as if they are "quantized." We can give a possible explanation for this behavior by the bifurcation as appeared in Fig. 2.The inserted diagram "period two" shows an appearance of two stable states by bifurcation according to the increase of the parameter λ (b in Eq. (8)). We may identify two levels appeared in Fig.4 as the two states shown in the "period two" diagram.

4. Conclusion

We have shown that the recursion relations (1) studied in nonlinear dynamics may be applicable to dynamics of nuclear reactions in the CFP. Experimentally, observations of neutron emission illustrated characteristics of the l.d.e. suggesting the applicability of the nonlinear dynamics to the CFP..

Further investigation of the CFP as a complexity will be given in the following paper [8].

This work is supported by a grant from the New York Community Trust.

References

1. M.J. Feigenbaum, *J. Statistical Physics,* **19**, 25 – 52 (1978).

2. H. Kozima, *Proc. JCF6,* pp. 72 – 77 (2005).

3. H. Kozima, *The Science of the Cold Fusion Phenomenon*, Elsevier Science, 2006. ISBN-10:

0-08-045110-1.

4. H. Kozima, *Proc. ICCF13* (to be published).

5. H. Kozima, W.-S. Zhang and J. Dash, *Proc. ICCF13* (to be published).

6. J. Gleick, *Chaos*, Penguin books, ISBN 0-14-00.9250-1

7. A. De Ninno, A. Frattolillo, G. Lollobattista, G. Martinio, M. Martone, M. Mori, S. Podda and F. Scaramuzzi, *Europhys. Lett.* **9**, 221 (1989)

8. H. Kozima, "The Cold Fusion Phenomenon as a Complexity (3) – Characteristics of the Complexity in the CFP" *Proc. JCF8,* (in this issue).

The Cold Fusion Phenomenon as a Complexity (3)
– Characteristics of the Complexity in the CFP –

Hideo Kozima,
Cold Fusion Research Laboratory,
421-1202, Yatsu, Aoi, Shizuoka 421-1202, Japan

Abstract

Complexity in the cold fusion phenomenon is investigated using several experimental data sets and its characteristics are determined. It is shown that the density n of the trapped neutrons (quasi-free neutrons in CF materials) assumed in the TNCF model is used as the parameter of recursion relations in the nonlinear dynamics in which bifurcation and chaotic behavior are mathematically investigated very well. Thus, the CFP has to be investigated taking nonlinear dynamical point of view into consideration.

1. Introduction

In the previous paper [1], we have shown that the recursion relations in nonlinear dynamics [2] describe fundamental properties of events in the cold fusion phenomenon (CFP), giving mathematical foundation for previous treatments of the CFP as complexity [3 – 6].

The experimental data set of neutron emission obtained by De Ninno et al. [7] was analyzed as an example showing a recursion function $f(x)$ in the recursion relations

$$x_{n+1} = \lambda f(x_n) \quad (n = 0, 1, 2, 3, \cdots) \quad (1)$$

and also showing a bifurcation depicted by a logistic difference equation (l.d.e.), a special type of the equation (1),

$$x_{n+1} = \lambda x_{n+1} (1 - x_n). \quad (2)$$

In that analysis, the parameter n_n (the suffix n in this notation specifies the neutron) assumed in the trapped neutron catalyzed fusion model (TNCF model) was identified as the variable x_n in Eq. (1) or Eq. (2).

In this paper, we give a unified explanation of typical experimental data sets obtained in the CFP on the basis of the investigation of complexity given in the previous works [1, 3 – 6].

2. Analysis of Typical Experimental Data Sets Showing Characteristics of Complexity

There are several data sets of the CFP showing dependences of observables (physical quantities) on such parameters as time τ, temperature T, the loading ratio η of hydrogen isotopes to host metals (η = D/Pd, H/Ni, etc.), density of neutrons in the material n_n, electrolytic or discharge current density i, and so forth. In this section, we list up typical experimental data sets exhibiting some features of the recursive equations (1) and the l.d.e. (2).

2.1. Data set by De Ninno et al. [7]

The experimental data set obtained by De Ninno et al. shows neutron emission from TiDx samples in dynamical processes of absorption/desorption when the sample temperature T varied between 77 K and the room temperature. As was explained in the previous paper [1], the variations of the neutron emission simulate the characteristics of the l.d.e. [2].

2.2 Data set by McKubre et al. [8]

The experimental data set of excess energy generation in Pd/D_2O + LiOD/Pt electrolytic systems by McKubre et al. [8] is one of the most extensive calorimetric result obtained in this field. The excess power P_{ex} (W/s) has been observed as functions of the loading ratio η (= D/Pd) and electrolytic current density i (A/cm^2) in addition to temporal variation of P_{ex}.

Based on our quantum mechanical investigation, we may assume that the number density n of trapped neutron increases with η which makes the super-nuclear interaction more effective to build up the neutron band below zero [4] when other conditions are kept constant.

We investigate the data by McKubre et al. [8] from this point of view. Then, Fig. 1 shows the temporal evolution of their data [8, Fig. 5] which is to be compared with the inserted figures of Fig. 2 of [1].

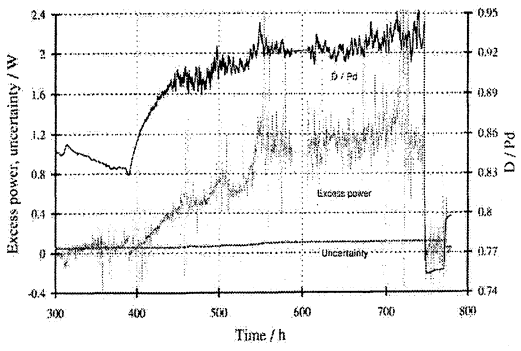

Fig. 1. Variation of Excess Power, Uncertainty and Loading ratio [8].

In the initial part from 400 to 550 h

of Fig. 1, the loading ratio η increase from 0.8 to 0.92 and the excess power P_{ex} increases up to about 0.8 W while with a burst at around 460 – 470 h. This increase of P_{ex} with η (or n_n in our interpretation) reminds us the recursion function $f(x)$ shown in Fig. 1 of [1]; the excess power P_{ex}, which is proportional to n_n, increase with n_n until a point n_n_where $f(n)$ becomes a maximum.

The bursts of P_{ex} appear while η does not change much as we see in Fig. 1. We may interpret these variations of P_{ex} as a presentation of bifurcation as appeared in inserted figures of Fig. 2 of [1] in the case of the l.d.e.

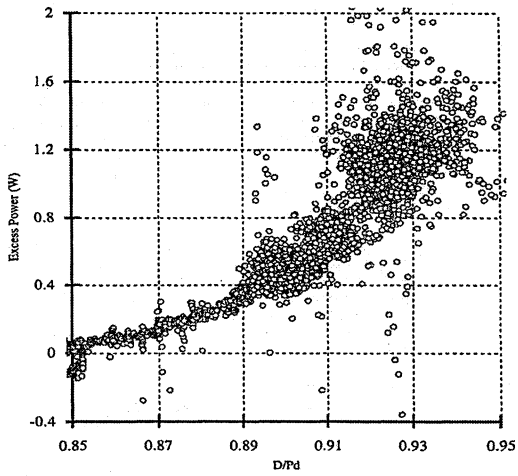

Fig. 2 Variation of Excess Power with Loading ratio [8]

Figure 2 shows the variation of the excess power P_{ex} as a function of the loading ratio [8, Fig. 7]. The excess power depicted in this figure shows such a chaotic behavior for η > 0.89 as appeared in "Chaotic region" of Fig. 2 of [1].

Furthermore, there appear several chaotic behavior at $I \simeq 0.1$, 0.4, 3.9, 5.1 and 7.1 in Fig. 3 where are plotted P_{ex} vs. cell current I. As far as we know at present, there are no explicit relations between the cell current I and the parameter n (density of the trapped neutrons) we used to explain Fig. 1 and 2. The occurrence of the chaotic behavior in Fig. 3 may be accidental depending on other uncontrollable factors in the system.

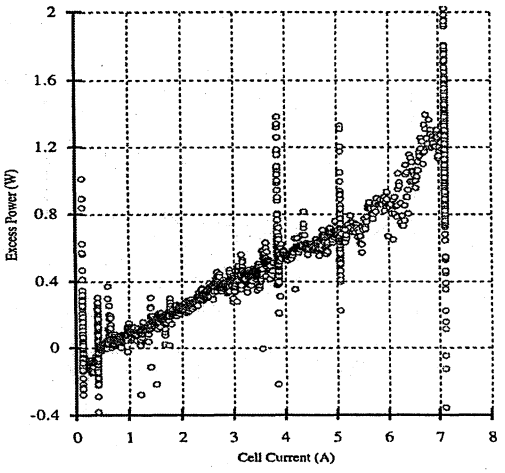

Fig. 3 Variation of Excess Power with Cell Current

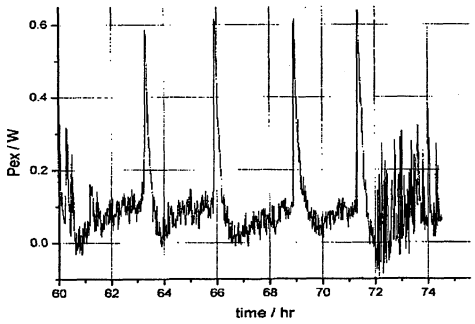

Fig. 4. Excess power pulses during a 14 hour period of an experiment (070108) of Dash et al.[6] which lasted 12 days as a whole.

2.3 Data set by Dash et al. [6]

Experimental data set of the excess energy in $Pd/D_2O + H_2SO_4/Pd$ electrolytic systems by Dash et al. [6] gives another illustration of complexity in the CFP. They observed temporal variations of P_{ex} with bursts up to 20 W as shown in Fig. 4 similar to those observed by McKubre as shown in Fig. 1.

These features of the excess power P_{ex} as a function remind us the behavior of the l.d.e. as shown in inserted figures of Fig. 2 of [1] as pointed out already in relation to Fig. 1 in Section 2.2.

With a statistical treatment of the data sets obtained by Dash et al., we could show bifurcation of the excess power generation in Fig. 5 [6]. To plot this figure, we assumed that the amount of excess power increases with temperature of the sample generalizing property of the system that P_{ex} is finite only if the temperature of the system is higher than a critical temperature $T_c \simeq 90$ degC.

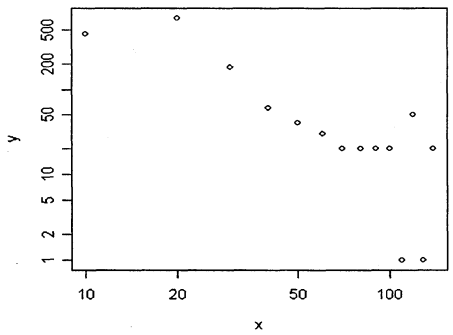

Fig. 5. Distribution of the frequency N_P (= y) producing excess power P_{ex} (= x). To depict log-log curve, values of N_P and P_{ex} were arbitrarily multiplied by 10^n. (x = 100 in this figure corresponds to P_{ex} = 1 W).

The behavior of P_{ex} depicted in Fig. 5 illustrates explicitly the bifurcation of the state in the l.d.e. appeared at $3 < b < 3.4$ in Fig. 2 of [1].

2.4 Positive Feedback of Nuclear Reactions in the CFP

We have shown several examples of the bifurcation (or bifurcation-like behavior) of the CFP in experimental data sets in the above subsections. In these figures, the bursts of signals corresponding to the branch of Fig. 5 or Fig. 2 of [1]

may be realized by upper more effective positive feedbacks to increase the population or density than the lower branch.

Even if the bursts of the excess power generation in Figs. 1 and 4 and of the neutron emission in Fig. 2 of [7] have finite heights, we may suppose cases where they increase without limit not restrained by any negative feedback thus resulting in explosions.

2.5 Explosions observed in the CFP

There are several reports of explosions in the CFP. The first group of the explosion is comparatively well analyzed [9, 10]. In these cases, the Pd cathodes were narrow cylinders similar to that used by Dash et al. [6].

The positive feedback observed in the excess power bursts appeared in Fig. 4 might be effective to raise the sample temperature especially due to the specific shape (cylinder) of the cathodes and finally to induce explosions in these cases [6].

The second group of the explosion is composed of the cases observed by Fleischmann et al. [11] and by Mizuno et al. [12]. These explosions occurred in experiments with cathodes with simple geometry in ordinary electrolytic system Pd/D_2O + LiOD/Pd and in plasma discharge system W/H_2O + K_2CO_3/Pt with a voltage of 350 V. These data may be explained by the similar mechanism to that sued in the first group while we do not have enough data to discuss them, further.

Another explosion observed in SRI reported by Smedley et al. [13] might be classified to the second group if it is related to nuclear reactions in the Pd cathode.

3, Conclusion

Several events of the CFP have explained by characteristics of complexity assuming that the parameter n of the TNCF model corresponds to the variable of the recursion relations (1).

The TNCF model has been effectively used to explain semi-quantitative relations between observables in the CFP. The investigation given in this paper has shown again ability of the idea contained in the model to explain some characteristics of the CFP as complexity. This result clearly shows that events in the CFP does not have quantitative reproducibility but qualitative or statistical one common to many-body systems.

The assumption of the parameter n_n as a variable in the

recursion relations (1) will be investigated in following works.

This work is partially supported by a grant from the New York Community Trust.

References

1. H. Kozima, "The Cold Fusion Phenomenon as a Complexity (2) – Parameters Characterizing Cold Fusion Systems" *Proc. JCF8* (2007) in this issue.

2. M.J. Feigenbaum, "Quantitative Universality for a Class of Nonlinear Transformations" *J. Statistical Physics,* **19**, 25 – 52 (1978).

3. H. Kozima, "The Cold Fusion Phenomenon as a Complexity (1) – Complexity in the Cold Fusion Phenomenon" *Proc. JCF6,* pp. 72 – 77 (2005).

4. H. Kozima, *The Science of the Cold Fusion Phenomenon*, Elsevier Science, 2006. ISBN-10: 0-08-045110-1.

5. H. Kozima, "Physics of the Cold Fusion Phenomenon" *Proc. ICCF13* (2007, to be published).

6. H. Kozima, W.-S. Zhang and J. Dash, "Precision Measurement of Excess Energy in Electrolytic System $Pd/D/H_2SO_4$ and Inverse-power Distribution of Energy Pulses vs. Excess Energy" *Proc. ICCF13* (2007, to be published).

7. A. De Ninno, A. Frattolillo, G. Lollobattista, G. Martinio, M. Martone, M. Mori, S. Podda and F. Scaramuzzi, "Evidence of Emission of Neutrons from a Titanium-Deuterium System," *Europhys. Lett.* **9**, 221 (1989)

8. M.C.H. McKubre, S. Crouch-Baker, A.M. Riley, S.I. Smedley and F.L. Tanzella, "Excess Power Observed in Electrochemical Studies of the D/Pd System," *Proc. ICCF3*, pp. 5 – 19 (1993).

9. X. Zhang, W-S. Zhang, D. Wang, S. Chen, Y. Fu, D. Fan and W. Chen, "On the Explosion in a Deuterium/Palladium Electrolytic System, "*Proc. ICCF3,* p. 381 (1992).

10. J.-P. Biberian, "Explosion during an electrolysis experiment in an open cell mass flow calorimeter," presented at *6th International Workshop on Anomalities in Hydrogen/Deuterium loaded Metals*, Siena, Italy, May 13-15 2005.

11. M. Fleischmann, S. Pons and M. Hawkins, "Electrochemically induced Nuclear Fusion of Deuterium," *J. Electroanal. Chem.*, **261**, 301 – 308 (1989).

12. T. Mizuno and Toriyabe, "Anomalous energy generation during conventional electrolysis" *Proceedings of ICCF12*, pp. 65 – 74,

(2006)
13. S.I. Smedley, S. Crouch-Baker, M.C.H. McKubre and F.L. Tanzella, "The January *2, 1992,* Explosion in a Deuterium/Palladium Electrolytic System at SRI International" *Proc. ICCF3,* pp. 139 – 151 (1992).

A note without reviewing.

An Explanation of Earthquake Lightning by Cold Fusion

Hiroshi Yamamoto
3110-17, Tsuzuki, Mikkabi-Town, Kita-Ku, Hamamatsu-City, Shizuoka-Pref. Zip:431-1402, Japan
e-Mail: hughy@aqua.ocn.ne.jp

ABSTRACT: The recent deployment of many seismometers and occurrences of earthquakes in Japan revealed explosive nature of earthquakes. There have been a few reports that earthquakes and strange emissions of light called earthquake lighting took place simultaneously, but there is no plausible hypothesis to correlate each other. Recently, a new idea has emerged that atomic hydrogen can generate energy somewhat between chemical reaction and nuclear reaction by lowering the electron orbit from the ground state to lower states. A hydrogen atom with much lower electron orbit below the ground state naturally has lower Coulomb barrier and would be much easier to fuse each other, resulting in the generation of neutrinos. It is known that water injection into deep wells can cause earthquakes. Water can be dissociated into atomic hydrogen by metals under the ground. This paper proposes a hypothesis that the power source of earthquakes is hydrogen fusion and generation of neutrinos by hydrogen fusion would excite nitrogen and water vapor in the atmosphere, resulting in earthquake lightning.

Key words: atomic hydrogen, hydrogen fusion, gamma ray, neutrinos. earthquake lightning

The mechanism of earthquakes is currently explained by the plate-tectonics theory which claims the earth's surface is covered with a series of crustal plates that can store elastic energy caused by relative movement of each plate. But recent deployment of GPS (Global Positioning System) revealed occurrences of gradual slip of the plates and also explosive nature at the event of earthquakes.

There are two ways to generate excess energy from hydrogen and its isotope. One is fusion and the other is to drop the electron in hydrogen atom from the ground state to the lower one. The latter is quite controversial to the current quantum physics, but R. Mills demonstrated that hydrogen atoms can achieve lower states than ground state by a resonant collision with a near by atom or combination of atoms having the capability to absorb the energy to effect the transition, namely, an integer multiple of the potential energy of the electron at atomic hydrogen, $m \times 27.2eV$ (m=integer) [1] . He named this shrunken hydrogen atom "hydrino" and claims that this hydrino can be a catalyst to shrink other hydrinos to further lower states. He named this reaction the BlackLight process.

Mills' hydrino mechanism has been paid little attention by researchers of low energy nuclear reaction (late abbreviated as LENR), but recently, E. Storms who is one of the pioneer in this field stated in a magazine interview, "Only the Mills' hydrino mechanism has all of the necessary features combined into one theory. In other words, LENR requires the existence of something having the basic features of the hydrino[2]".

Based on his hypothesis, R. Mills succeeded in generating energy somewhat between chemical and nuclear reaction.

Currently Mills' work has been concentrated in low pressure vessels under 1 torr with a scavenging pump and it will not evolve to fusion but it would be so if the vessels are rigid and tight enough, in which well shrunken hydrinos that have small Coulomb barrier can be produced, and then fuse.

In 1961, a deep well was drilled at northeast of Denver Colorado U.S.A for disposal of nuclear waste fluids. Injection was commenced March 1962, and shortly after that, an unusual series of earthquakes erupted in the area. Injection had been discontinued and the number of quakes decreased dramatically. When the injection was resumed, quakes increased accordingly and the link between the fluid injection and earthquakes was established[3]. The most notable experience in this series of earthquakes is that many people heard extremely loud, explosive-like earth noises.

The Earth's crust is divided into several separate solid plates. Subduction occurs when two plates collide and the edge of one dives beneath the other. The crust contains water and when it contacts with metals such as iron, atomic hydrogen will be produced according to the following reaction.

$3\,Fe + 4\,H2O \rightarrow 8\,H + Fe3O4$ -----(1)

"H" designates atomic hydrogen.

Once atomic hydrogen is produced and if there is no heat sink at the collision point, just a collision of atomic hydrogen for a instance,

$H + H \rightarrow H2$ (molecular hydrogen) wouldn't take place but just elastically repulse each other. This suggests that atomic hydrogen can exist much longer than normally expected. The pressure and temperature at 30km bellow the surface of the earth would be around 1GPa and 1500 Celsius degree. When the reaction (1) takes place at this condition and atomic hydrogen gas builds up, the pressure of the atomic hydrogen gas would be getting higher and higher and finally there would be cracks at the surrounding rocks of the hydrogen gas, resulting in pressure drop of the hydrogen gas.

3 body collision of atomic hydrogen is the BlackLight process because ionization energy of hydrogen is 13.6 eV and 2 hydrogen atoms give 27.2eV to the third hydrogen atom, resulting in the following reaction.

$H + H + H \rightarrow H[n=1/2] + 2\,H^+ + 2\,e^-$ ------ (2)

H[n=1/2] designates a hydrogen whose electron orbit is shrunken to 1/2 the radius of a normal one and these will be shrunken further to lower orbits as reaction continues.

Well shrunken hydrinos would then fuse each other as is the case of muon catalyzed fusion due to small Coulomb barrier.

Fig 1 illustrates the hydrogen fusion.

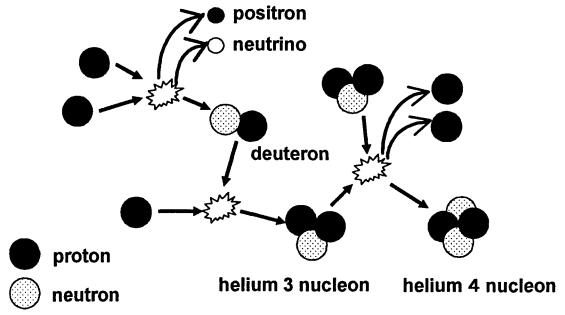

Fig. 1 Process of hydrogen fusion

High pressure molecular hydrogen gas up to 70MPa is now being used for fuel cell cars but almost no technical information on the stability of high pressure atomic hydrogen gas is available because it's almost impossible to make such a gas here on the ground.

Only information available concerning the initiation of the BlackLight process is the one carried out by BLACKLIGHT POWER Inc., but these are limited at very low pressure. The Black-Light process is quite sensitive to the pressure and it can be expected that the same characteristic curve as is the case for the self ignition curve of the stoichiometric mixture of hydrogen and oxygen shown in Fig 2.

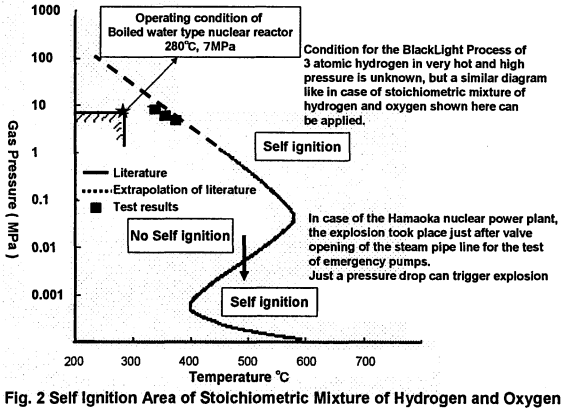

Fig. 2 Self Ignition Area of Stoichiometric Mixture of Hydrogen and Oxygen

Source:Chubu Electric Power Company:
Reactor Manual Shutdown Caused by Pipe Rupture in Residual Heat Removal System at the Hamaoka Nuclear Power Station Unit-1 (Final Report), April 2002 (in Japanese).

The author has reported that when the gas pressure of atomic hydrogen reaches such a high pressure that surrounding rocks can not sustain, gas leakage starts and the atomic hydrogen gas plunges into the area of the BlackLight process, resulting in hydrogen fusion under the ground, namely earthquake(4).

There are a couple of evidence that suggest hydrogen fusion can take place under the ground. One example is the helium spot which emitted helium gas during the Matsushiro swarm earthquakes in Japan(5). Another is the anomaly of helium-3 found in the gasses escaping from volcanoes on which S. Jones hypothesized that it was made in the Earth's interior by hydrogen fusion(6).

The first step of the fusion by hydrogen is :

p + p = d + positron + electron neutrino, where d designates deuteron.

Positron will recombine with electron, emitting gamma ray (0.511MeV) which may not be transmitted to the ground surface through the cracks made by earthquakes, but electron neutrinos can penetrate the crust. Electron neutrinos have very little capability to interact with matters but it can be reasonably postulated that huge neutrino flux generated by M7 class earthquakes (equivalent to one mega-ton class hydrogen bombs) can energize gas molecules in the atmosphere such as nitrogen and water vapor, resulting in generation of lightning or luminescence. Luminescence by neutrinos is utilized to study the characteristics of neutrinos in research laboratories and is a well known phenomenon.

In the past, it could have been hardly imagined atomic hydrogen gas can explode by itself but the BlackLight process by R. Mills opened the way to investigate the cause of anomalous explosion of hydrogen from a new standpoint of view. From the relationship between water injection into deep wells and occurrences of earthquakes, it can be reasonably concluded that earthquakes are caused by fusion of hydrogen dissociated from water that is bought deep in the earth by subduction of crustal plates. Electron neutrinos produced by hydrogen fusion can energize gas molecules in the atmosphere such as nitrogen and water vapor, resulting in generation of lightning or luminescence.

REFERENCES

(1) R.L. Mills, P. Ray, B. Dhandapani, R.M. Mayo, J. He, "Comparison of Excessive Balmer Alpha Line Broadening of Glow Discharge and Microwave Hydrogen Plasmas with Certain Catalysts," Journal of Applied Physics, Vol. 92, No. 12, (2002), pp. 7008-7022

(2) J.A. Rudesill, "An Interview with Dr. Edmund Storms, Author of The Science of Low Energy Nuclear Reaction", New Energy Times, January, 2008, No. 26

(3) Nicholson, Craig and Wesson, R.L., "Earthquake Hazard Associated with Deep Well Injection," A Report to the U.S. Environmental Protection Agency, U.S. Geological Survey Bulletin 1951, pp.74 .

(4) H.Yamamoto, "An Explanation of Earthquakes by the Blacklight Process And Hydrogen Fusion," Proceedings of the 12th International Conference of Cold Fusion, pp. 577-581, Yokohama, 2005

(5) H.Wakita, et al., "Helium Spots: Caused by Diapiric Magma from the Upper Mantle," Science, Vol. 200, April 28, 1978, pp. 430-432

(6) S.E.Jones, E. P. Palmer, J. B. Czirr, D. L. Decker, G. L. Jensen, J. M. Thorne, S. F. Taylor, J. Rafelski, "Observation of Cold Nuclear Fusion in Condensed Matter," Nature 338, pp737-740

About a Principle of Condensation

Norio YABUUCHI
High Scientific Research Laboratory
2nd Floor, Takano Building, 24-16 Marunouchi, Tsu City, Mie 514-0033, JAPAN
E-mail yabuuchi@kogakken.co.jp

Lorentz-Fitzgerald contractions have been evident as an experimental reality, but the theory behind them is complex, and just as Einstein explained incomprehensible Lorentz-Fitzgerald contractions by means of the principle of the constant speed of light and the Pythagorean theorem, the author has attempted to elucidate a theory of baffling condensation by means of Coulomb's law, the Platonic structure and the Pythagorean theorem. That is to say, when q1 is taken to be a positively charge (+d) and q_2 is taken to be a negatively charge (-e), their charges are the same +1 and −1,

$$(F =) \mid q_1q_1/4\pi\varepsilon r^2 \mid = \mid q_2q_2/4\pi\varepsilon r^2 \mid$$

Repulsion

$$= \mid q_1q_2/4\pi\varepsilon r^2 \mid$$

Attraction **1**

The auther arranged +d and −e on the vertices of the regular polyhedron each others. and calculated the ratio repulsion to attraction. as shown like next.

In a regular tetrahedron, the ratio of attraction to repulsion

Ratio is 2:1, with 4 vertices. **2**

In a cube, the ratio of attraction to repulsion

Ratio is 12:0, with 8 vertices. **3**

In a regular octahedron, the ratio of attraction to repulsion

Ratio is 2:1, with 6 vertices. **4**

In a regular dodecahedron, the ratio of attraction to repulsion

Ratio is 4:1, with 20 vertices. **5**

In a regular icosahedron, the ratio of attraction to repulsion

Ratio is 2:1, with 12 vertices. **6**

The cube and the regular icosahedron have a high ratio of Coulomb attraction to repulsion is 12:0 and vertices that number 20 , which, surprisingly enough, are magic numbers.

In this regard, the author made reference to Figure 1 and employed the Pythagorean theorem to calculate the strength of condensation attraction for the cube, which has the highest Coulomb-attraction ratio.

$$q_1(d_1)q_2(-e_1)+q_1(d_1)q_2(-e_2) > q_2(-e_1)q_2(-e_2) \quad \mathbf{7}$$

$$q_1(d_1)q_2(-e_1)/4\pi\varepsilon r^2 + q_1(d_1)q_2(-e_2)/4\pi\varepsilon r^2 > q_2(-e_1)q_2(-e_2)/4\pi\varepsilon \left(r\sqrt{2}\right)^2 \quad \mathbf{8}$$

$$\mid -2q_1q_2/4\pi\varepsilon r^2 \mid > \mid + q_2q_2/8\pi\varepsilon r^2 \mid \quad \mathbf{9}$$

Similarly,

$$\mid -2q_2q_1/4\pi\varepsilon r^2 \mid > \mid + q_1q_1/8\pi\varepsilon r^2 \mid \quad \mathbf{10}$$

In the same way, the Coulomb attraction with respect to the -e-e and +d+d that are the Coulomb repulsion of all other diagonal lines is accounted for by Equations 9 and 10,

Rewriting Equations 9 and 10 as general expressions yields the following:

$$-2q_1q_2 \text{ (or } q_2q_1)/4\pi\varepsilon r^2 > +q_1q_1 \text{ (or } q_2q_2)/8\pi\varepsilon r^2 \quad \mathbf{11}$$

$$-2q_1q_2(\text{or } q_2q_1)/4\pi\varepsilon r^2 > +q_1q_1(\text{or } q_2q_2)/2\cdot 4\pi\varepsilon r^2 \quad \mathbf{12}$$

$$-4q_1q_2(\text{or } q_2q_1)/4\pi\varepsilon r^2 > +q_1q_1(\text{or } q_2q_2)/4r\pi\varepsilon r^2 \quad \mathbf{13}$$

$$\mid -4 \mid > \mid +1 \mid \quad \mathbf{14}$$

As a result, under the Yabuuchi model, when +d and −e are arranged alternatingly at the vertices of a cube inscribed within a sphere, according to Equation 14, total attraction exerts four times the force of repulsion, causing condensation of +d. That is to say, calculation based on the Pythagorean theorem relating to the two combination of diagonal lines $-e_1$ to $+d_2$ and $-e_3$ to $+d_4$ yields.

For both attraction and repulsion, magnitude is

equal and shared, and calculation using an electrical charge of +1 or -1 yields a regular hexahedron whose sides are all of identical size, and because calculation can be performed with distance r = 1,

$(-q_2(e_1)q_1(d_2)/4\ \pi\varepsilon r^2) + (-q_2(e_3)q_1(d_2)/4\ \pi\varepsilon\left(r\sqrt{3}\right)^2) > +q_2(e_3)q_2(e_1)/4\ \pi\varepsilon\left(r\sqrt{2}\right)^2$ **15**

$-q_2q_1/4\ \pi\varepsilon r^2 + (-q_2q_1/4\ \pi\varepsilon r^2 3) > +q_2q_2/4\ \pi\varepsilon r^2 2$ **16**

($-e_1$ to d_2) is as ($-e_3$ to d_4)

Similarly, calculation based on the Pythagorean theorem relating to the two combination of diagonal lines $+d_1$ to $-e_2$ and $+d_3$ to $-e_4$ yields this:

$-q_1(d_1)q_2(e_2)/4\ \pi\varepsilon r^2 + (-q_1(d_3)q_2(e_2)/4\ \pi\varepsilon r^2 3) > (+q_1(d_3)q_1(d_1)/4\ \pi\varepsilon r^2 2$ **17**

$-(1 + 1/3) > +1/2$ **18**

$|-1.33| > |+0.5|$ **19**

(d_1 to $-e_2$) is as (d_3 to e_4)

This proves that attraction is greater than repulsion.

Thereupon synthesizing ,in these 14,19 equation

$|-F| : |F| = 5.33 : 1.5 = 3.55 : 1$ **20**

$|-F| = 3.55\,|F|$ **21**

That is to say, this equal shows principle of condensation.namely,In case of arrangeing positively charge and negatively chage on the veritices of regular hexahedron,because of coulomb attraction is increased coulomb repulsion 3.55 times, 8 veritices condense perfeetly.

As the auther request the principle of Condensation by coulomb power.

Next, try to apply to Condensation of neucler fusion.

fig 1

YABUUCHI MODEL

+ → positive charge
— → negative charge

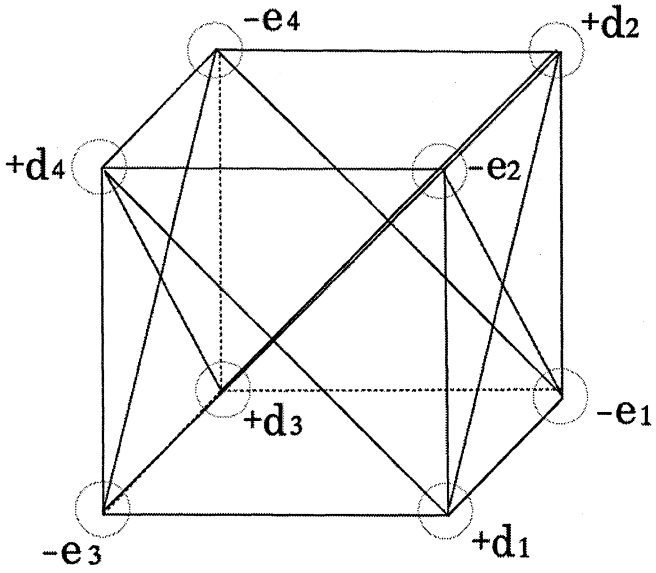

The relation between a Pythagorean theorem and Coulomb's law in regular hexahedron(cube)